ELECTROCHEMICAL SUPERCAPACITORS

ADVANCED MATERIALS AND FABRICATION METHODS FOR ELECTROCHEMICAL SUPERCAPACITORS

By

Mustafa Sami Ata, B. Sc.

A Thesis

Submitted to the School of Graduate Studies

In Partial Fulfillment of the Requirements

For the Degree

Master of Science

McMaster University

MASTER OF SCIENCE (2012) McMaster University

(Materials Science and Engineering) Hamilton, Ontario

TITLE: Advanced Materials and Fabrication Methods for Electrochemical Supercapacitors

AUTHOR: Mustafa Sami Ata, B.Sc. (Kırıkkale University, Turkey)

SUPERVISOR: Dr. Igor Zhitomirsky

NUMBER OF PAGES: xv, 115

Abstract

The electrochemical supercapacitors (ESs) are an emerging technology that promises to play an important role in meeting the demands of automotive and electronic industry. A notable improvement in ES performance has been achieved through recent advances in understanding charge storage mechanisms and the development of advanced nanostructured materials, such as nanostructured MnO_2 and composites.

The anodic electrophoretic deposition (EPD) method has been developed for the fabrication of MnO_2 and composite MnO_2-multiwalled carbon nanotubes (MWCNTs) films. The problem of low stability of MnO_2 suspensions was addressed by the development of new dispersing agents. Benzoic acid and phenolic molecules, such as 3,4-dihydroxybenzoic acid, 3,4-dihydroxyphenylacetic, 3,4-dihydroxyhydrocinnamic acid, 3,4,5-trihydroxybenzoic acid, salicylic acid, 2,3,4-trihydroxybenzoic acid, aurintricarboxylic acid and aurintricarboxylic acid ammonium salt were investigated as additives for the dispersion and charging of MnO_2 nanoparticles. The adsorption of the organic molecules on the MnO_2 nanoparticles involved the interaction of COOH groups and OH groups with Mn atoms on the particle surfaces and complexation. The results showed that adjacent OH groups, as well as adjacent OH and COOH groups bonded to the aromatic ring of the phenolic molecules enabled enhanced adsorption of the organic molecules. It was found that EPD of MnO_2 and MWCNTs can be achieved using 3,4-dihydroxybenzoic acid, 2,3,4-trihydroxybenzoic acid, and aurintricarboxylic acid as a common dispersants and charging additives.

Aurintricarboxylic acid ammonium salt provided a charge required for efficient dispersion and EPD of MWCNTs and graphene.

New dispersion methods allowed the formation of composite electrodes by colloidal techniques, such as EPD or slurry impregnation of MnO_2 and MWCNTs into advanced current collectors, such as porous nickel foam and nickel plaque. The composite electrodes showed excellent capacitive performance with large material loading in 0.5 M Na_2SO_4 electrolyte. MnO_2 and MWCNTs can form a porous network, which is beneficial for the electrolyte access to the active materials. The effect of the MWCNTs concentration, scan rate and electrodes type on the capacitive behaviour was discussed. It was found that the addition of MWCNTs can improve the capacitive performance of MnO_2 electrodes and reduced equivalent series resistance.

Acknowledgement

First and foremost I offer my sincerest gratitude to my supervisor, Dr. Igor Zhitomirsky, who has supported me throughout my thesis with his patience and knowledge. I attribute the level of my Master's degree to his encouragement and effort and without him this thesis, too, would not have been completed or written.

Also I would give many thanks to all my team members in Dr. Igor Zhitomirsky's lab, Yaohui Wang, Deepak Kumarappa, Sun Yanchao, Lijia Yang, Imran Deen, Xiaofei Li, and Xin Pang for their kind help and friendship.

The Department of Materials Science & Engineering has provided the support and equipment I have needed to complete my studies. I am very thankful for the financial support from the Natural Science and Engineering Research Council of Canada (NSERC).

Finally, I take this opportunity to express my profound gratitude to my family for the moral support and patience during my study in Canada.

Table of Contents

List of Figures

List of Tables

Chapter 1 Introduction

With depletion of natural oil, alternative energy sources and methods of energy storage become increasingly important. Electrochemical supercapacitors (ESs) have attracted wide attention for energy storage due to their unique characteristics in term of high power density, excellent reversibility and longer cyclic life than conventional batteries[1]. Potential applications of ESs are: automobiles, portable electronic devices such as cellular phones, portable drills, camera flash lights, etc.

An ES is similar to a capacitor by design and construction, with an electrolyte instead of a dielectric material. ESs are categorized into two types based on the charge-storage mechanism[1]: (1) the electrochemical double layer capacitors (EDLC) and (2) pseudocapacitors. EDLC mechanism is based on the separation of charges at the interface between a solid electrode and an electrolyte[2], whereas pseudocapacitance involves fast, reversible Faradaic reactions which occur in the bulk of the electrode materials or at the electrode surface over an appropriate range of potentials[3]. ESs exhibit capacitance in the range from microfarads (μF) to thousands of farads (kF), at least 1,000 times larger than the capacitance of a typical electrolytic capacitor. ESs are also characterized by lower internal resistance compared to batteries. Active electrode materials such as carbon-based nanomaterials (carbon nanotubes, carbon fibers, graphene, etc.), conducting polymers (polyaniline, polypyrrole, etc.), and metal oxides (oxides of manganese, ruthenium, nickel, etc.) have received the most interest.

Many transition-metal oxides have been shown to be excellent electrode materials for ESs. Recently, a hydrous form of ruthenium oxide, RuO_2, in aqueous H_2SO_4 has been found to possess very high specific capacitance (SC) (720 F g^{-1}), which is associated with pseudocapacitance. Although RuO_2 system gives very high SC, it is quite expensive. To bring down the cost, oxides of iron, vanadium, nickel and cobalt in aqueous electrolytes have been explored. Of all the cheap metal oxides, MnO_2 is the most promising. Low cost, environmentally friendly, long cyclic life, high capacitance (the theoretical SC ~1370 F g^{-1})[4], and natural abundance of MnO_2 are its main features. Its potential application as an electrode material for ESs is being extensively studied. The main drawback of MnO_2 is poor electronic and ionic conductivity which results in low utilization of high theoretical SC in devices. The SC of MnO_2 reported in literature[5-7] is in the range of 100-300 F g^{-1}, which is quite low compared to its theoretical value. The problem of low conductivity of MnO_2 can be addressed by using MnO_2 composites. Conductive additives, such as carbon black, are usually added to MnO_2 in order to increase its electronic conductivity and improve the power density and energy density.

Chapter 2 Literature Review

2.1 History of supercapacitors technology

Supercapacitors, also called ultracapacitors, or electrochemical capacitors, have been known from the 1800s; however, in 1957 by H.I. Becker[8] of General Electric, the first electrical device using double-layer charge storage was patented by using porous carbon electrodes in an aqueous electrolyte. Eventually Standard Oil of Ohio's (SOHIO)[9] researchers developed the modern versions of devices and achieved higher energy density by utilizing the double-layer capacitance of high area carbon in a non-aqueous electrolyte, in 1966. In 1978, the term "supercapacitors" was quoted by NEC under the licences of SOHIO, to supply backup power for maintaining computer memory[10]. Also in the same year Panasonic began manufacturing double-layer capacitors, called 'Goldcap', in Japan. These were initially developed primarily to replace the unreliable coin cell batteries used in memory back-up applications at that time. The major differences between the Panasonic and NEC products were the electrolytes; NEC used an aqueous electrolyte in a 'pasted electrode' with bipolar cell construction; Panasonic, on the other hand, used a non-aqueous electrolyte and pasted electrode in the cell construction. The advantages of the Panasonic electrolyte is a higher unit cell operating voltage. Between 1975 and 1981 a different principle, called pseudocapacitors, was developed by B. Conway. Ruthenium oxide was the first expended material to prepare the electrodes of pseudocapacitors[11, 12]. However, the Ru-based materials are very expensive. Therefore, researchers investigated other metal oxides, such as manganese oxides and others.

The market for EDLCs is currently valued at approximately a half-billion dollars and continues to grow. Today several companies such as Maxwell Technologies, NEC/TOKIN, ELNA, Panasonic, and several others invest in electrochemical capacitor development.

2.2 Principles of energy storage

According to the energy storage mechanism, double layer capacitors are classified in two main types[1]: (1) electrochemical double-layer capacitors and (2) pseudocapacitors. In addition, hybrid systems were developed, which combined Faradaic and non-Faradaic process to store charge. In this chapter the charging mechanism of ESs and the difference in principles of energy storage of batteries and ESs will be discussed and compared.

2.2.1 Electrochemical double-layer capacitors

Electric double-layer capacitors (EDLCs) are based on the operating principle of the electric double-layer (Helmholtz layer) that is formed at the interface between activated a carbon electrode and an electrolyte. The principle behind the capacitor is demonstrated in Figure 2-1. When the voltage is applied, the positive and negative charges are distributed close to each other over an extremely short distance. Such a charge distribution is known as an electrical double-layer.

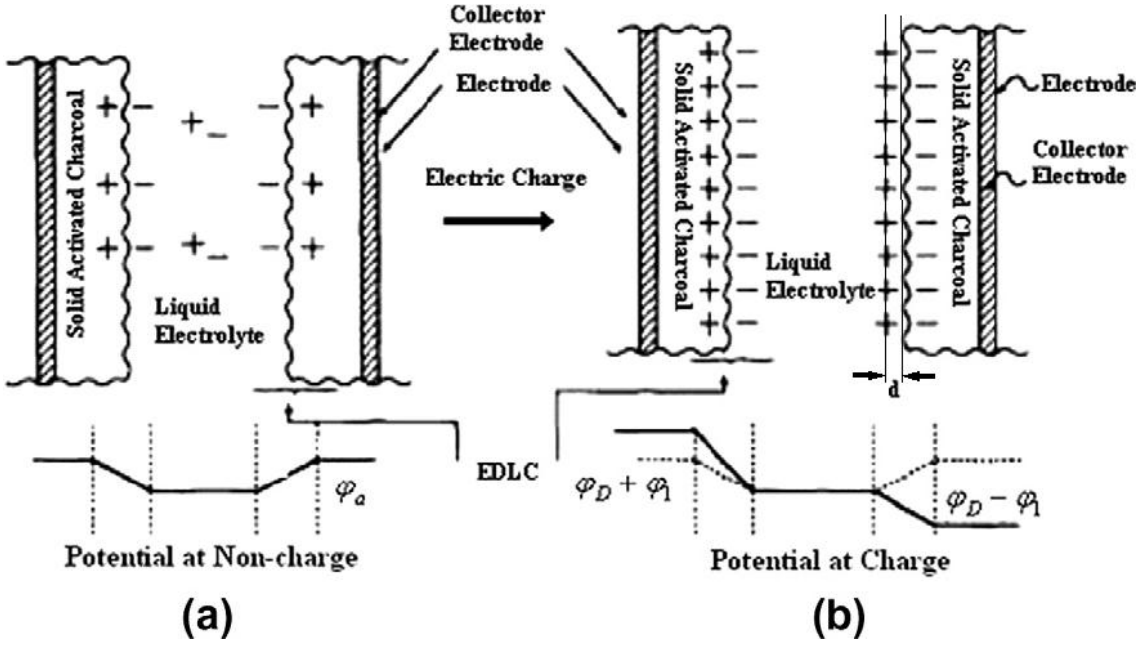

Figure 2-1 The principle of EDCL charge storage mechanism[13]

The double-layer capacitance can be estimated by the formula, similar to the conventional capacitors.

$$C = \varepsilon\varepsilon_0 A/d \qquad (2\text{-}1)$$

where ε is the dielectric constant of the double-layer region, ε_0 is the permittivity of free space, A is the surface area of the electrode and d is the thickness of the double layer, which depends on the concentration of the electrolyte and on the size of the ions.

EDLC has considerably more energy than the traditional capacitor. The first reason is that high-surface-area active materials are used in EDLC. The surface area A is much larger

than conventional capacitor`s electrode surface area. And the second one is the thickness of double-layer charge separation is very small. Other benefits of EDLC are: environmentally friendly, very high reversibility in repetitive charge/discharge and long cyclic life (>500,000)[14].

2.2.2 Pseudocapacitors

The energy storage mechanism of pseudocapacitors is much more complicated than the EDLC. The energy is stored when the oxidation state of the metal oxide is changed whereas the potential change at the electrode surface[1]. Pseudocapacitors or redox ESs, are based on the fast and reversible surface reactions for charge storage. Particle sizes, surface area, porosity, conductivity of active material, nature of the electrolyte and cell design are important factors, controlling the capacitive behaviour of the electrode materials. In the comparison to capacitance of EDLC, capacitance of pseudocapacitors is 10-100 times higher because the ions and cations actually diffuse into the electrode material rather than forming a double layer on the surface[15]. The capacitance can be calculated by following equation:

$$C = Q_{tot}/V_{tot} \qquad (2\text{-}2)$$

where Q_{tot} is the total charge and V_{tot} is the voltage change for charge/discharge of the electrode.

2.2.3 Hybrid systems

Hybrid capacitors offer many advantages and the minimize disadvantages of EDLCs and redox capacitors. Moreover, hybrid capacitors show better capacitive behaviour[16]. Hybrid capacitors combine Faradaic and non-Faradaic processes to store charge. Their energy and power density are much higher than corresponding parameters of EDLCs. On the other hand, their cycling stability is much better than that of pseudocapacitors. The principle of hybrid system is based on electrode combinations, classified as asymmetric, composite and battery type electrodes[16]. Asymmetric hybrids combine an EDLC electrode with a pseudocapacitor electrode. The composite electrode integrates carbon-based materials with conducting metal oxide or polymer in a single electrode with different charge storage mechanisms. Battery type hybrids combine ES electrodes with battery electrodes.

2.2.4 Power density and energy density

Energy density and power density are two major parameters for energy storage devices. Energy density represents the amount of energy stored per unit mass, while power density describes how fast the energy is released. The energy density (E) and power density (P) are calculated by:

$$E=CV^2/2m \quad (2\text{-}3)$$

$$P=V^2/4Rm \quad (2\text{-}4)$$

where C is the capacitance, V is the voltage, R is the equivalent series resistance (ESR) and m is the deposited mass. The equations indicate that capacitance voltage window must be high and ESR must be low for an ideal energy storage system. The power-energy characteristic of conventional capacitors, ES, battery and fuel cell are shown in the Ragone plot in Figure 2.2.

As it seen in the Figure 2-2, batteries and fuel cells have greater energy density than conventional capacitors and ES; on the other hand, they possess lower power density. Even though conventional capacitors process high power density, they have low energy density and cannot be used for long duration application. Meanwhile, ES fills the gap between batteries, fuel cell and conventional capacitors. ESs have lower energy density than batteries and fuel cell; however, they have the advantages of higher power density, higher cyclic life and reversibility.

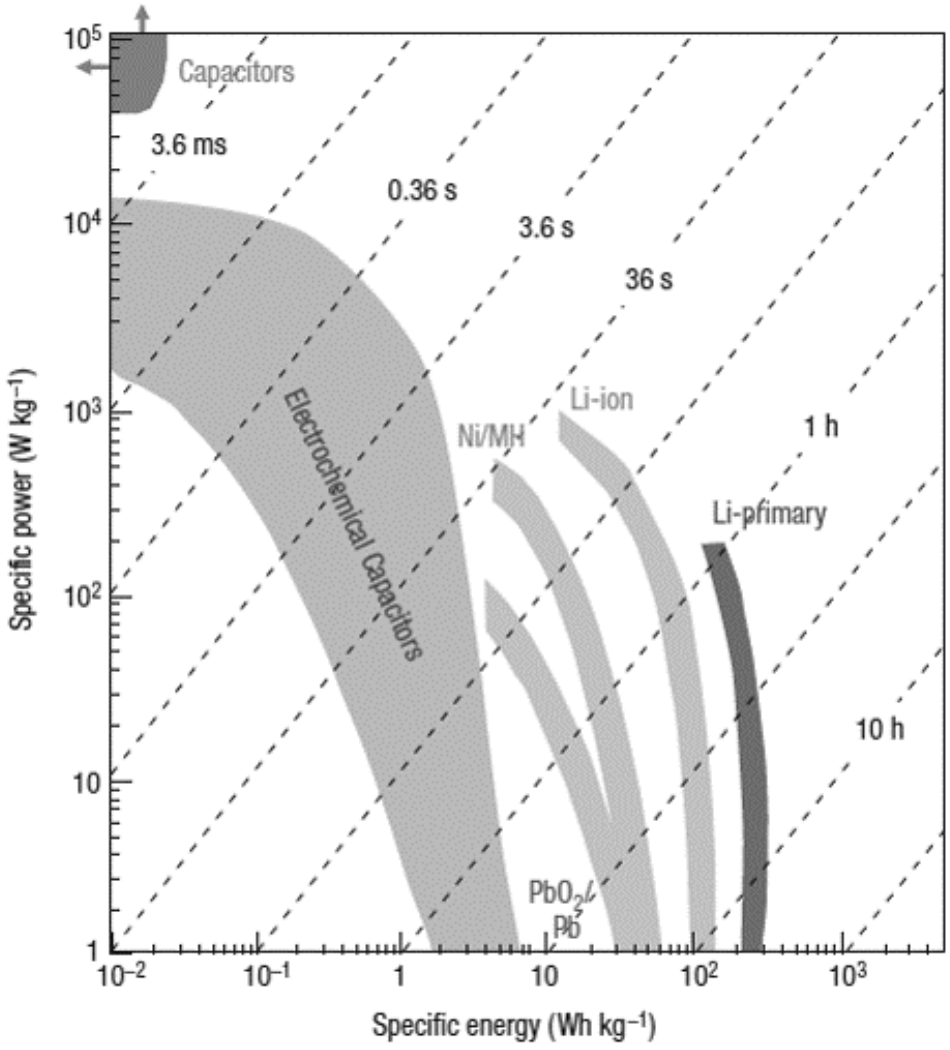

Figure 2-2 Sketch of Ragone plot for various energy storage and conversion devices. The cross line is the time constants of the devices, obtained by dividing the energy density by the power[17].

2.2.5 Applications of supercapacitors

Due to limited energy and power density, ESs were mostly used for memory back-up in early years. As for back-up source, the ESs are mostly used for memories, system boards, clocks, microcomputers. The increasing research helped to enhance their energy and power density. Therefore, ES can be usable for many applications such as small portable electronics, transportation and industrial equipment.

As main power source, the ESs can deliver large current pulses in milliseconds. ES can support fuel cells and batteries in automotive applications. Due to their high energy density, fuel cells and batteries are promising energy storage devices for electric vehicles. However, high power requirement is the biggest problem which can be addressed by ESs. ESs offer advantage of high charge-discharge rate[18, 19].

2.3 Electrode materials

As discussed earlier, ES can be divided into three types. The selection of electrode materials plays an essential role in specifying the ESs' electrical behaviour. As Figure 2-3 shows, ESs can be classified into three different materials, carbon based, metal oxides, and conducting polymers.

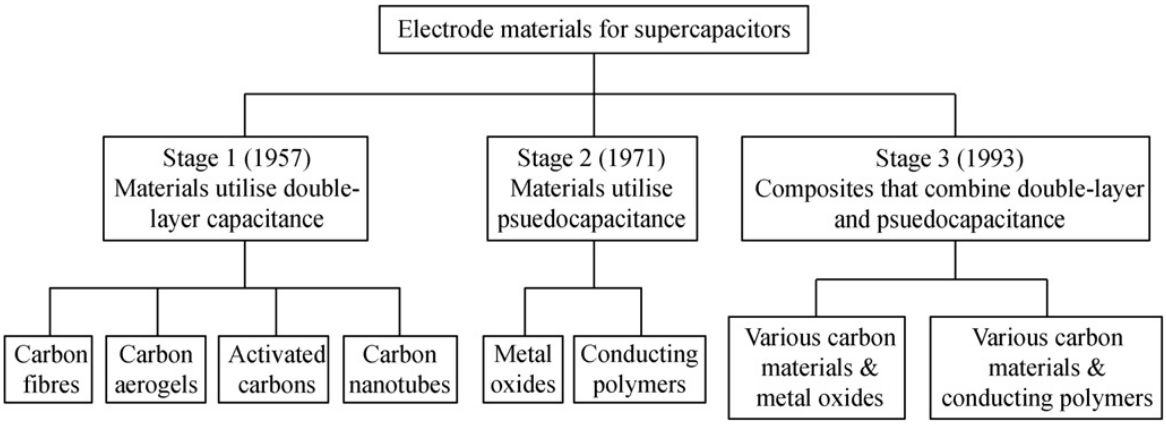

Figure 2-3 Taxonomy of the supercapacitor materials[20].

2.3.1 Carbon supercapacitors

The advantages of carbon materials are high conductivity, high surface area, corrosion resistance, high temperature stability, controlled pore structure, processability and compatibility in composite materials[21]. The relatively low cost makes carbon materials especially attractive for ES applications. The first two properties, high conductivity and high surface area, are most important factors for EDLC. If those two are low, the maximum power density of the capacitor will be limited. Activated carbons, carbon aerogels, carbon fibres and carbon nanotubes are different forms of carbon materials, commonly used as electrode materials for ESs.

2.3.1.1 Activated carbons

As mentioned above, high surface area is one of the advantages of carbon materials. In an attempt to achieve a high capacitance, the electrode surface area is additionally increased

by activating carbon[21], in the range from 500 to ~3000 m^2 g^{-1}. The process of increasing electrode surface area consists of thermal and chemical treatment of carbonaceous material. There are mainly three classes of pores classified by International Union of Pure and Applied Chemistry (IUPAC)[22]; (1) micropores (diameter < 2nm), (2) mesopores (diameter < 2 - 50 nm) and (3) macropores (diameter > 50nm). Nevertheless, not all pores are electrochemically accessible. The larger size of electrolyte ions causes the restriction of the movement of electrolyte. Additionally, the high surface area and porosity can result in a poor conductivity, which is affecting power density[23]. Because of the smaller size of solvent ions and a higher dielectric constant of aqueous electrolyte, it provides higher capacitance value (in the range from 100 to 200 F g^{-1}) than in organic electrolyte (in the range of 50 to 150 F g^{-1})[24].

The influence of pore size distribution of activated carbon on capacitance, development of low cost carbon based materials, design of electrodes are major areas of research in EDLCs[23, 25].

2.3.1.2 Carbon Aerogels

The advantages of carbon aerogels such as high surface area (400 to 1000 m^2 g^{-1}), electrical conductivity, environmental compatibility, uniform pore size (between 2 to 50 nm), high density and chemical stability make them very promising materials for future energy related applications. Additionally, the surface area, pore size and volume can be modified independently of each other. Carbon aerogels are prepared by the pyrolysis of

organic aerogels and usually synthesized by the poly-condensation of resorcinol and formaldehyde. They can also be produced as monoliths, composites, thin films, powders or microspheres. In order to increase the capacitive performance, different methods have been investigated, such as thermal activation, electrochemical activation and chemical vapour impregnation[21, 26, 27].

2.3.1.3 Carbon fibers

Carbon fibers are well known since the late 1950s. A carbon fiber is a long, thin strand of material about 10 μm in diameter and composed mostly of carbon atoms. They can be woven to a certain pattern or just placed randomly. The most noteworthy application in this class is the carbon fiber composite. The certain pattern makes the fiber incredibly strong for its size. Several thousand carbon fibers are twisted together to form a yarn, which may be used by itself or woven into a fabric. Mostly, carbon fibers are used as a composite material. Consequently, the yarn or fabric is combined with epoxy and wound or molded into shape to form various composite materials. Carbon fiber composites were first used only by space industry due to high manufacturing costs. However, in the past two decades cheaper manufacturing methods allowed carbon fibers composites to be used in wide range applications such as military and airplane manufacturing where the demands for this material was at peak. Yet it is not to be restricted with airplane components, carbon fiber components, which also are used to make racing car bodies, golf club shafts, fishing rods, automobile springs, bicycle frames and many other

components where high strength and light weight are needed. CNTs are attractive materials for ESs because of high conductivity and low percolation threshold.

2.3.1.4 Carbon nanotube

Carbon nanotubes (CNTs) have attracted great attention owing to their unique pore structure characteristics, such as good electrical conductivity, high strength, good electrolyte accessibility, good chemical and thermal stability which are important for ESs electrode applications[23, 28, 29].

CNTs are ideal hollow tubes rolled up from two-dimensional graphene sheet. CNTs were classified as Multi-Wall Carbon Nanotubes (MWCNTs)[30] and Single-Wall Carbon Nanotubes (SWCNTs)[31] by Lijima, as shown in Figure 2- 4. Depending on the number of tubes, SWCNTs are 1-2 nm in diameter and tens of microns in length.

CNTs have amazing mechanical and electrical properties which contribute to high strength and conductivity. Thoteson et al.[32] reported that elastic modules of CNTs are greater than 1TPa and strengths 10-100 times higher than the strongest steel at a fraction of the weight. Also, the theoretical and experimental results show superior electrical properties of CNTs. Collins et al.[33] reported that CNTs can produce high electric current carrying capacity, which is 1000 times higher than that of copper wires.

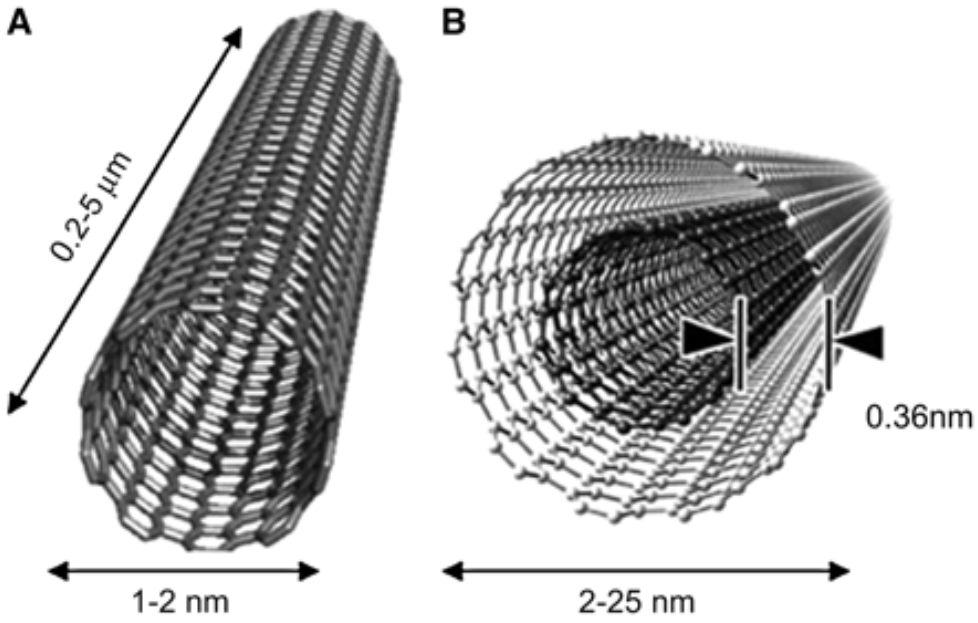

Figure 2-4 Conceptual diagram of single-walled carbon nanotube (SWCNT) (A) and multiwalled carbon nanotube (MWCNT) (B) delivery systems showing typical dimensions of length, width, and separation distance between graphene layers in MWCNTs[34].

Their unique properties allow them to be used in many industrial applications. They are attractive in field of reinforcements in composites, sensors and probes, energy storage, electrochemical devices, nanometer sized electronics and etc.

2.3.2 Metal oxides

Besides carbon, metal oxides offer an attractive alternative as electrode materials due to high SC at low resistance, suitable for ES application. Transition metal oxides such as

RuO_2, NiO, MnO_2, Fe_3O_4, V_2O_5 etc. have been extensively studied as electrodes for pseudo-capacitors.

2.3.2.1 Ruthenium oxide

Among metal oxides, ruthenium oxide (RuO_2) has been widely studied due to metallic conductivity, high SC, electrochemical reversibility, and long cyclic life[35-37]. Low equivalent resistance (ESR), 10^{-5} Ω lower than that of the other electrode materials, enables to achieve high energy and power density when RuO_2 is used as an electrode material[38]. RuO_2 makes itself a perfect electrode material for ESs due to its ability to combine the metallic type conductivity and excellent reversible Faradaic reactions (redox reactions). The redox reactions happen inside the bulk of material and also at the electrode/electrolyte interface[3]. The redox reaction of RuO_2 can be expressed as:

$$RuO_2 + xH^+ + xe^- \longleftrightarrow RuO_{2-x}(OH)_x \qquad (2\text{-}5)$$

where, $0 \leq x \leq 2$, Ru oxidation states can change from (II) to (IV)[17]. Annealing conditions directly affect the SC of the hydrous RuO_2 (600 to 1000 F g^{-1})[39]. Figure 2-5 illustrates a typical CV of $RuO_2 \cdot xH_2O$, which indicates the ideal charge/discharge behaviour in 0.5 M H_2SO_4 in the voltage range of 0 to -0.9 V at different scan rates[40]. Yet the only problem with $RuO_2.xH_2O$ is high cost for commercial applications. Therefore, high cost and rarity of RuO_2 have induced a search for alternative electrode materials.

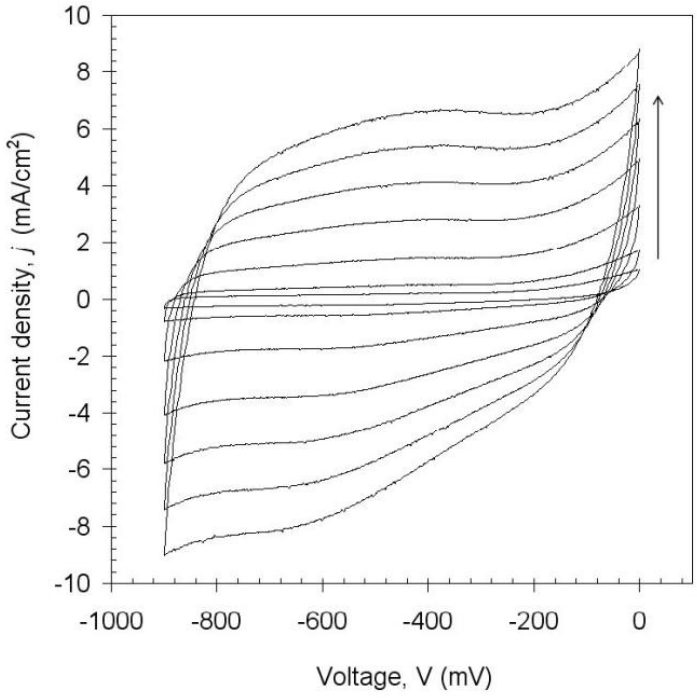

Figure 2-5 The CV curves of ruthenium oxide electrode at different scanning rates in 0.5 M H_2SO_4[40].

2.3.2.2 Nickel Oxide

Nickel oxide (NiO) is one of the promising materials for ES application due to its easy synthesis, environmental friendliness, relatively high SC (theoretical value of 2584 F g^{-1}), and low cost[41]. NiO films have been prepared in three different ways, thermal treatment of electrodeposited $Ni(OH)_2$[42, 43], sol-gel[44], and electrostatic spray deposition[45]. The redox reaction of NiO can be expressed[42, 44]:

$$NiO + OH^- \longleftrightarrow NiOOH^- + e^- \quad (2\text{-}6)$$

According to Cheng et al.[46], nickel oxide electrochemical surface reactivity is dependent on its crystalline structure. Therefore, the value of x of NiO_x is being affected by temperature significantly, correspondingly the SC. For instance, SC of 696 F g^{-1} can be reached at 250 ^oC, yet when heated to 300 ^oC the capacitance reduced[46]. Besides the temperature, the preparation process is also important for the electrochemical behaviour of NiO[47]. For example, the maximum SC of cubic structure of NiO was 167 F g^{-1}, with sol-gel method it increased to 200 – 250 F g^{-1}, and SC reached 696 F g^{-1} after sample annealed at 250 ^oC[46].

However, NiO based electrode has some disadvantages, such as poor cyclic stability and high resistivity (low electrical conductivity).

2.3.2.3 Cobalt oxide

Cobalt oxide (Co_3O_4) has been reported to be potential material for ESs applications due to excellent reversible redox behaviour, high conductivity, good corrosion stability and long-term performance[48]. The redox reaction of Co_3O_4 originates from the following charge storage mechanism[49]:

$$Co_3O_4 + H_2O + OH^- \longleftrightarrow 3CoOOH + e^- \qquad (2\text{-}7)$$

The SC value of 165 F g^{-1} has been reported for Co_3O_4-based electrodes in a 1.0 M aqueous KOH electrolyte at 10 mV s^{-1} scan rate by Kandalkar et al[50]. Cobalt oxide has

negative voltage capacitive behaviour; therefore, it can be coupled with other positive electrodes. For instance, The highest SC value of $Co_{0.72}Ni_{0.28}$ LDHs (cobalt-nickel layered double hydroxides) has been reported 2104 F g^{-1} [45]. Therefore, Co/Ni composites are promising materials for ESs.

2.3.2.4 Iron oxide

Iron oxide (Fe_3O_4) is another potential material for ES electrode due to low cost. However, its low SC is the biggest problem for future application. For instance, the Fe_3O_4 electrode presented SC of 3, 5-25, 118-170 F g^{-1} in aqueous 1.0 M KOH, Na_2SO_4, Na_2SO_3, respectively[51].

2.3.2.5 Vanadium oxide

Vanadium oxide (V_2O_5) has been widely researched as electrode materials for ESs in aqueous and organic electrolytes. The SC of 350 F g^{-1} has been reported for amorphous V_2O_5 in KCl aqueous electrolyte[52]. According to Lee and Goodenough[52], the K^+ ions were involved in the ES redox reaction of amorphous V_2O_5. Vanadium oxide has been used in electrochemical redox reactions with Li ions in an organic electrolyte as in lithium secondary batteries[53]. The low electronic conductivity is the biggest complication; however, metal fibres and carbonaceous materials composites have been prepared to improve the electronic conductivity of V_2O_5. Unfortunately, the SC of the V_2O_5 electrode

exhibits a quick fade over only a few hundred cycles[54]. Electrochemical capacitors require long-term stability of the active electrode materials. Therefore, V_2O_5 has a disadvantage of low cyclic stability.

2.3.2.6 Manganese oxide

As an alternative to RuO_2, manganese oxides (MnO_2) offer the advantages of relatively low cost, low toxicity, and environmental safety, as well as high theoretical capacitance (~1300 F g^{-1})[55]. MnO_2 have been used for lithium batteries[56], sensors[57], catalysts[58], alkaline Zn/MnO_2 cells[59] applications. MnO_x has been considered a promising alternative material for ES electrodes since 1999 by Lee et al.[60]. The synthesis of manganese oxide thin film comprehend electrochemical deposition[61, 62], electrospinning[63], hydrothermal[64], sol-gel[65], electrostatic spray deposition[66, 67] and other chemical methods[68-70]. Figure 2.6 shows cyclic voltammetry (CV) of electrophoretically deposited MnO_2 electrode at different scan rates in 0.1M Na_2SO_4 electrolyte[45]. The SC values of MnO_2 have mostly been reported in the range of 100 and 350 F g^{-1} [71-73], which is far from the theoretical capacitance value ~1300 F g^{-1}. Pang et al.[74] prepared a thin MnO_2 layer (~4 µg cm^{-2}) by a sol-gel method and achieved 700 F g^{-1} in potential window 0-0.9 V. However, the SC value decreased with the increasing film thickness and scan rate[37, 73, 74]. The capacitance of manganese oxide is attributed to reversible redox transitions involving exchange of protons and/or cations with the electrolyte[75]. The capacitive behaviour is attributed to the reaction[74, 75]:

$$MnO_{\alpha}(OC)_{\beta} + \delta C^{+} + \delta e^{-} \longleftrightarrow MnO_{\alpha-\beta}(OC)_{\beta+\delta} \quad (2\text{-}8)$$

where $C^{+} = Li^{+}, Na^{+}, K^{+}$, $MnO_{\alpha}(OH)_{\beta}$ and $MnO_{\alpha-\beta}(OH)_{\beta+\delta}$ indicate aqueous manganese oxide at high and low oxidation states, respectively.

There are also several challenges for MnO_x as ES electrode. (a) Poor electronic conductivity and low surface area. To improve these, several approaches have been investigated, one of which is doping other metal into MnO_x. For instance, the nickel doping increased the surface area of MnO_x by around 46% and the SC by 37% [76]. Doping with ruthenium[77], nickel[78], Mo[79] and also activated carbon, CNTs, graphite, and conducting polymers have been helpful to improve conductivity. (b) Poor ionic conductivity[5]. Nanostructured MnO_x materials have been investigated to improve ionic conductivity. For example, multilayered MnO_2 yielded high ionic conductivity even at the high potential scan rate of 100 mV s^{-1} [80]. Figure 2-6 shows typical cyclic voltammetry (CV) of chemically deposited MnO_2 electrode at different scanning rates in 1.0M Na_2SO_4 electrolyte.

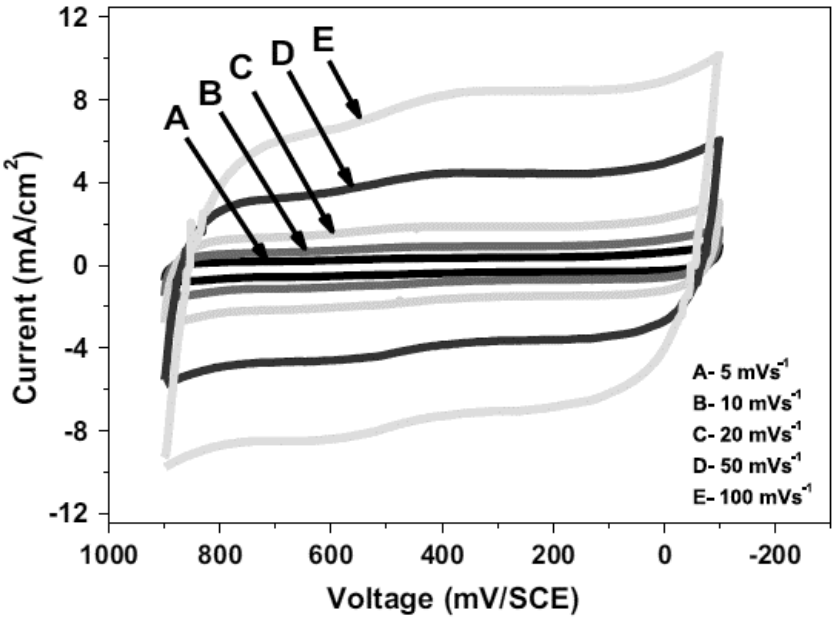

Figure 2-6 The typical cyclic voltammetry (CV) of MnO_2 electrode at different scanning rates; (A) 5, (B) 10, (C) 20 (D) 50 and (E) 100 mV s^{-1} in 1.0 M Na_2SO_4 electrolyte[45].

2.3.2.7 Other metal oxides

Many other metal oxide materials, such as SnO_2, In_2O_3, IrO_2, Bi_2O_3, et al. have also been studied as electrode materials for ES. Amongst the metal oxide materials, RuO_2, MnO_2, Co_3O_4, and NiO have been mostly studied because other metal oxides suffer from one problem or another, such as low capacity, poor cyclic capability, low electric conductivity, high cost and so on. Their applications as ES electrode materials seem

unrealistic for today's technology. Figure 2-7 represent comparison of different metal oxide thin film SC values as ES electrode materials.

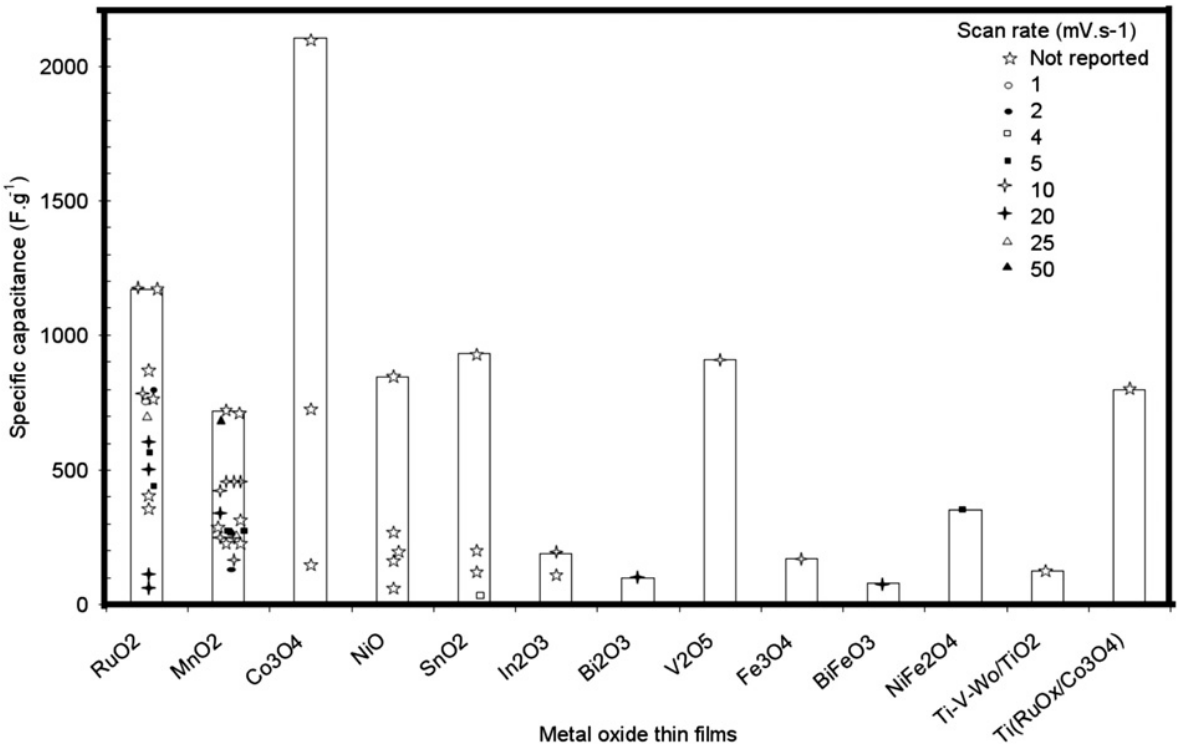

Figure 2-7 Comparison of metal oxides SC values at different scan rates[45].

2.3.3 Conducting polymers

Conducting polymers (CPs) have been regarded as promising materials for ES application because of low cost, low environmental impact, high conductivity in doped state, high voltage window, high storage capacity, high porosity, and high reversibility[81, 82]. The charge/discharge behaviour of CPs electrode is related to Faradaic reaction process. As shown in Figure 2-8, when oxidation occurs, ions are transferred to polymer backbone.

During the discharge types of charged polymers, n-doped and p-doped, return to neutral states, and the ions are released from backbone into the electrolyte. The positively-charged polymers, acquaints by oxidation, are termed as p-doped, and negatively-charged polymers accomplished by reduction are termed as n-doped.

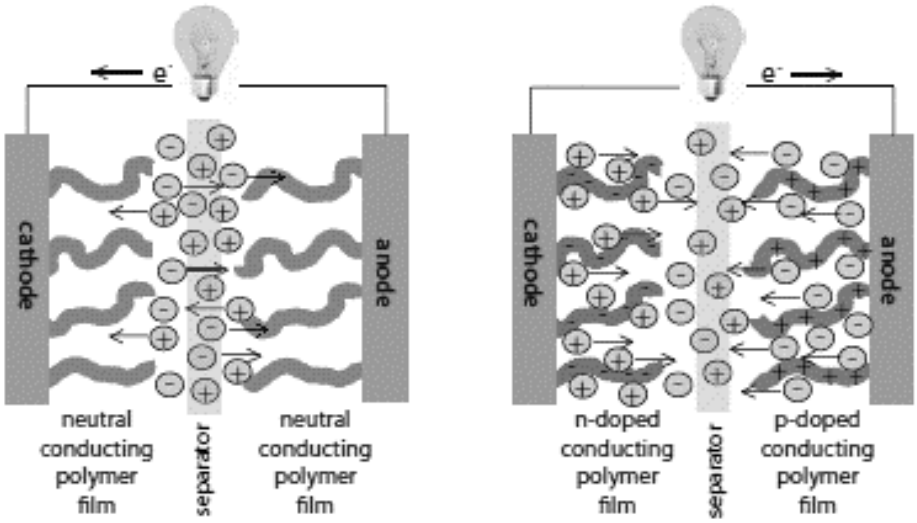

Figure 2-8 Electroactive polymer-based electrochemical capacitor schematic showing electron flow and ion movement during charge (right) and discharge (left)[83].

The most commonly utilized CPs are polyaniline (PANI)[84], polypyrrole (PPy)[85], polythiophene (PYh)[86] and their corresponding derivatives. The main disadvantage of CPs as ESs electrode material is poor mechanical stability during cycling due to swelling and shrinking. It is well known that CNT has a great mechanical behaviour. Therefore, regarding composite electrodes, adding carbon, especially CNTs into CPs will be an effective solution[87]. For example, a PANI/CNT composite electrode had high SC value of

1030 F g^{-1}, superior rate capability of 95%, capacity retention at 118 A g^{-1}, and high stability, which is only 5.5% capacity loss after 5000 cycles, between -0.2 and 0.7 V (vs SCE) at 10mA in 1 M H_2SO_4 electrolyte[88]. Additionally, potential range is crucial for CPs, inherently for ES applications. Beyond this range, the polymer can be switched to neutral state. Table 1 illustrates the potential range for composite CPs for ESs applications.

Table 1 SC of CPs-based composites[89]

CPs-based composite	Specific capacitance/F g^{-1}	Electrolyte	Voltage window/V	Current load or scan rate	Reference
Ppy-20wt%MWNTs/ PANI-20wt% MWNTs	320 (Type II)	1.0 M H_2SO_4	0–0.6	5 mV s^{-1}	163
PANI-20 wt% MWNTs	670 (3-Electrode)	1.0 M H_2SO_4	−0.8–0.4	2 mV s^{-1}	
	344 (Type I)		0–0.6		
Ppy-20 wt% MWNTs	506 (3-Electrode)	1.0 M H_2SO_4	−0.6–0.2	5 mV s^{-1}	
	192 (Type I)		0–0.5 (*vs.* Hg|Hg_2SO_4)		
PEDOT-Ppy (5 : 1)	230 (3-Electrode)	1.0 M $LiClO_4$	−0.4–0.6 (*vs.* SCE)	2 mV s^{-1}	168
	290 (3-Electrode)	1.0 M KCl	−0.4–0.6 (*vs.* SCE)	2 mV s^{-1}	
	276 (Type I)	1.0 M KCl	0–1.0 (*vs.* SCE)	3 mA cm^{-2}	
Ppy-CNTs//PmeT-CNTs	87 (Type II)	1.0 M $LiClO_4$ in AC	0–1.0	0.62 A g^{-1}	169
PPy-65 wt% carbon	433 (3-Electrode)	6.0 M KOH	−1.0–0(*vs.* Hg|HgO)	1 mV s^{-1}	170
Ppy-graphene	165 (Type I)	1.0 M NaCl	0–1.0	1 A g^{-1}	171
Ppy-MCNTs	427 (3-Electrode)	1.0 M Na_2SO_4	−0.4–0.6 (*vs.* Ag|AgCl)	5 mV s^{-1}	172
Ppy-29.22 wt% mica	197 (3-Electrode)	0.5 M Na_2SO_4	−0.2–0.8 (*vs.* SCE)	10 mA cm^{-2}	173
Ppy-67.36 wt% mica	103 (3-Electrode)				
Ppy-RuO_2	302 (3-Electrode)	1.0 M H_2SO_4	−0.2–0.7 (*vs.* Hg|HgO)	0.5 mA cm^{-2}	174
Ppy-MnO_2	602 (3-Electrode)	0.5 M Na_2SO_4	−0.5–0.5 (*vs.* Ag|AgCl)	50 mV s^{-1}	151
PANI-Ti	740 (3-Electrode)	0.5 M H_2SO_4	−0.2–0.8 (*vs.* Ag|Ag^+)	3 A g^{-1}	175
PANI-80wt% graphene	158 (3-Electrode)	2.0 M H_2SO_4	0–0.8 (*vs.* AgCl|Ag)	0.1 A g^{-1}	176
PANI-50wt% graphene	207 (3-Electrode)				
PANI-10wt% graphene	320 (3-Electrode)				
MPANI/CNTs	1030 (3-Electrode)	1.0 M H_2SO_4	−0.2–0.7 (*vs.* SCE)	5.9 A g^{-1}	164
PANI-Si	409 (3-Electrode)	0.5 M H_2SO_4	0–0.8 (*vs.* AgCl|Ag)	40 mA cm^{-2}	177
PEDOT-MCNTs (70 : 30)	120 (Type I)	1.0 M H_2SO_4		2 mV s^{-1}	146
	80	6.0 M KOH			
	60	1.0 M $TEABF_4$ in AN			
PEDOT-MCNTs (80 : 20)	160 (AC as the negative electrode)	1.0 M $TEABF_4$ in AN	0–1.5	0.2 A g^{-1}	

Note: PPy: polypyrrole; PANI: polyaniline; Type I, II: defined by A. Rudge *et al.*;[139] PEDOT: poly(3,4-ethylenedioxythiophene); PTh: poly(thiophene); PMeT: poly(3-methylthiophene); PFPT: poly[3-(4-fluorophenyl)thiophene]; AN: acetonitrile; $TEABF_4$: tetraethylammonium terafluoroborate; PC: propylene carbonate; 3-electrode: standard 3-electrode cell; SCE: saturated calomel electrode; AC: activated carbon.

2.4 Electrolytes

The electrolyte is also as important as the two electrodes in ESs design. The fundamental aspects of electrolytes include: wide voltage window range, high electrochemical stability, high ionic concentration and low resistivity, volatility, viscosity, toxicity, solvated ionic radius, low cost as well as purity. Power density is dependent on the cell's ESR, which depends strongly on electrolyte conductivity. ESs cell voltage is limited by the electrolyte decomposition at high potential; therefore, energy density is also limited by the electrolyte.

The electrolytes for ESs can be classified into three types: aqueous electrolyte, organic electrolyte, and ionic liquids.

2.4.1 Aqueous electrolyte

Aqueous electrolytes offer benefits of a higher conductivity, solubility of the salts, ionic concentration, and the lower cost compared with the organic electrolytes. Due to the higher ionic concentration and smaller ionic radius, aqueous electrolytes may provide higher capacitance and higher power compared to the organic electrolytes. However, the biggest disadvantage of aqueous electrolytes is their small voltage window, typically 1.2 V, much lower than the organic electrolytes, above 2 V. According to Equation (2.3), the low operating voltage induces a low energy density. These disadvantages can be partially compensated by the low ESR of aqueous electrolyte. H_2SO_4, KOH, Na_2SO_4, NH_4Cl and NaOH are mostly used electrolytes in ESs as acid and alkaline electrolytes because of

their high conductivity and proton transport mechanism. According to Long et al.[90], asymmetric cell design by using two different electrochemical processes improves low voltage window. For instance, Fe_3O_4 composite electrode as a negative electrode and MnO_2 composite electrode as a positive electrode in a hybrid capacitor allowed voltage window of 1.8 V.

2.4.2 Organic electrolytes

The large advantage of organic electrolytes over aqueous electrolyte is large voltage window as high as 2.7 V. Therefore, higher voltage window can increase the energy density because the energy density is proportional to the voltage square as it can be seen in Equation 2.3. Normally, organic electrolytes' voltage window is typically 2.3 V, with some possible achievement it increases to 2.7 V in short time. With the extreme purification procedure voltage window of 3.2 V was achieved by some companies. However, high resistivity (20-60 Ω) of organic electrolytes is the cause of lower power density than aqueous electrolytes, because the resistivity of organic electrolytes is at least 20 times higher than aqueous electrolytes. Additionally the pore size of electrodes for organic electrolytes is also larger because of the large size of organic molecules[91]. Acetonitrile and propylene carbonate (PC), triethylmethylammonium tetrafluoroborate ($TEMABF_4$) are most commonly used solvents. Although acetonitrile can dissolve larger amounts of salt than other solvents, environmental and toxic effects pose problems. PC-based electrolytes are environmentally friendly and can contribute a wide electrochemical

window as well as good conductivity[89]. Although organic electrolytes are most commonly used in ESs due to high voltage window, higher cost, lower conductivity, smaller power capability, more complex production conditions are still needed to be developed.

2.4.3 Ionic Liquids

Ionic liquids (ILs) are synthesized by combination of cations and anions. The advantages of ILs are that they are non-flammable and non-corrosive, thermally and hydrolytically stable, wide liquid phase range (-100-400 ^{o}C), low vapour pressure, adjustable viscosity, high ionic conductivity (~10^{-3}-10^{-2} S cm^{-1}), non-toxicity and large electrochemical window[92]. The wide electrochemical window of ILs electrolytes has significantly enhanced energy and power density. Moreover, the high ionic concentration of ILs is possibly terminated the electrolyte depletion problem, which significantly improved capacitors performance. Despite all these advantages, ILs are too expensive for commercial applications for near future.

2.5 Design of supercapacitors

The ESs are built on three important parameters; the SC value, cell voltage and ESR. These parameters are directly related to the energy and power densities of ESs. As seen in

Figure 2-9, representation of a ES and battery are mostly similar; both of them comprised two electrodes and a separator between electrodes and an aqueous electrolyte.

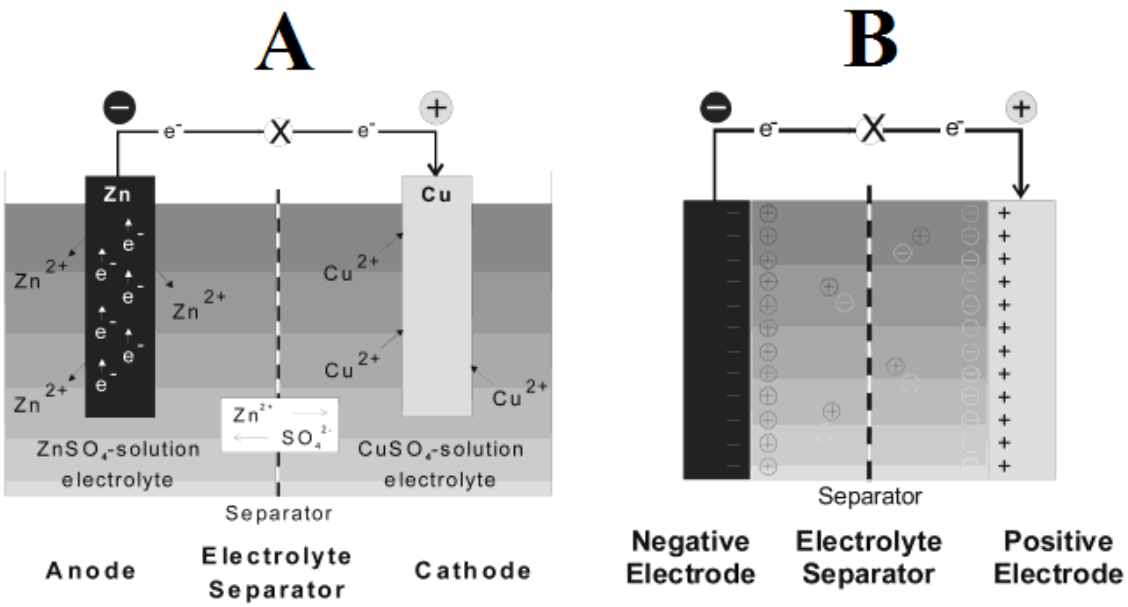

Figure 2-9 Representation of (A) Battery and (B) ESs[93].

The electrode material, which has a very good electrochemical conductivity, is very important for achieving high SC value. Another feature of the materials of ESs is being possessed a high specific surface area to reinforce their charge-storage capability. The high porosity of electrodes also helps to enhance the capacitance value of ESs. The high porosity allows electrolyte ions to penetrate into the porous electrodes.

The specific energy and power, Eq (2.3) and (2.4) respectively, are proportional to the square of operating voltage. Therefore, the specific energy and power are affected by the low cell voltage. In order to meet the operating voltage requirements, ES cells must be

connected in series. This reduces the capacitance value and increases the resistance of the cells. Asymmetric cell design, combination of Faradaic and non-Faradaic processes by coupling an EDLC and pseudocapacitors electrode, is developed to avoid the small cell voltage. New electrolytes development is also important as much as electrode material to enhance high voltage window.

As discussed before, the maximum power density is dependent on ESR, which included the ionic and electronic resistance. The high ESR not only causes low power density but also low efficiency. The electrolyte and separator, current collector, contact resistance between the current collector and active materials and other contact resistances are the four different causes of increasing or decreasing value of ESR.

The choosen electrolyte, electrode materials, separator thickness and porosity are playing critical roles in the ESs performance. Additionally, environmental issue, the mechanical and electrochemical stability, and self-discharge of ESs need to be considered.

2.6 Fabrications of supercapacitors

The fabrication of ES cells are based on five steps; coating the electrodes, winding, filling with an electrolyte, testing and welding and sealing.

2.6.1 Electrode fabrication

The most important step is the electrode coating, which affects capacity, life expectancy, self-discharge, resistance and cost of ESs. There are various types of methods for coating

ESs electrode, such as sol-gel method[7, 74], chemical precipitation method[60], electrodeposition[71] and other methods[67, 94]. MnO_2 is one of the most attractive electrode materials for ESs application. MnO_2 films generally are used for producing thin film electrodes and for modifying interface between current collector and electrodes material, while composite materials are used to produce bulk electrodes. There are two kinds of electrodes, (i) thin film electrodes and (ii) composites electrodes.

2.6.1.1 Thin film electrodes

Manganese oxide films are prepared by sol-gel method by either dip-coating or drop coating[74]. A thin film coating is formed on clean substrate by dipping the foil into the sol and withdrawing it at a controlled speed for the dip-coating procedures whereas sols are dropped directly onto a horizontal substrate forming a small circular spot, then left to dry in the air for drop-coating procedures. According to Pang et al.[74], thin manganese oxide film, which prepared by sol-gel method, achieved SC value of 700 F g^{-1}. The thickness variations can be obtained by repeating the dip- and drop-coating procedures. However, complicated procedures and some undesirable effects on electrochemical properties and conductivity of electroactive materials make sol-gel unpopular technique for fabricating electrodes for ESs.

Schoonman et al.[95] have developed an electrospray deposition (ESD) technique for transition metal oxide films to be used in various applications, such as ESs, organic solar cells, gas sensors electrodes and so on. ESD method is the technique of spraying various

kinds of solution of biomacromolecules and/or synthetic polymers, to form nano-sized particles and fibers (nano-fiber),which were deposited on a substrate using electrostatic force (Figure 2-10). The major advantages of the ESD method are simply easy set-up, low cost, environmentally friendly precursors, high deposition efficiency and easy control of the surface morphology of deposited layers. The main disadvantage is that the process is restricted to diluted precursor solutions with low conductivity (<5 mS cm^{-1})[96].

Electrochemical deposition methods is one of the most attractive methods due to high purity, high uniformity, low operating temperature, controlled deposition rate and controlled microstructure[97]. In this work manganese oxide films were prepared by anodic electrodeposition technique. The brief outline of the technique is given below.

Electrodeposition, which comprises electrophoretic deposition (EPD) and electrolytic deposition (ELD), is one of the most popular methods due to low cost, rigid control of deposition rate, uniformity and film thickness. Figure 2-11 illustrates schematic of electrolytic and electrophoretic deposition.

Electrodeposition is an attractive technique for surface engineering. Electrodeposition of ceramic and composite films is currently under investigation for various applications, such as catalysis, fuel cells, ESs, protection of metals, biomedical implants, quantum dots and batteries[98]. EPD is achieved via the electrophoretic motion of charged particles in a suspension and film formation at the electrode under an applied electric field. This method requires the fabrication of stable suspensions, containing well dispersed charged colloidal particles. In electrolytic deposition method, ceramic particles are produced in

electrode reactions from solutions of metal salts and form a solid deposit at the electrode surface.

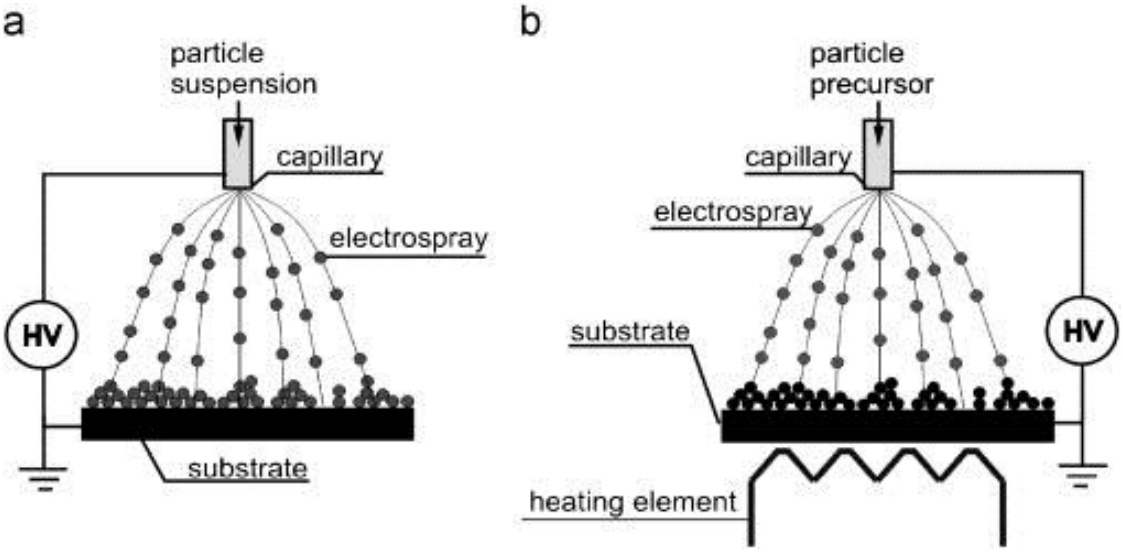

Figure 2-10 Scheme of electrospray deposition of micro- and nano-thin film: (a) from a solution or suspension of particles to be deposited and (b) from a precursor thermally decomposed on the substrate[99].

The deposition rate of the EPD technique is much faster than that of the ELD, resulting in significantly higher deposit thicknesses. Therefore, ELD enables the fabrication of thin nanostructured ceramic films while EPD is normally utilized to produce thick films. Figure 2-12 represents the different thickness of coatings obtained by the EPD and ELD.

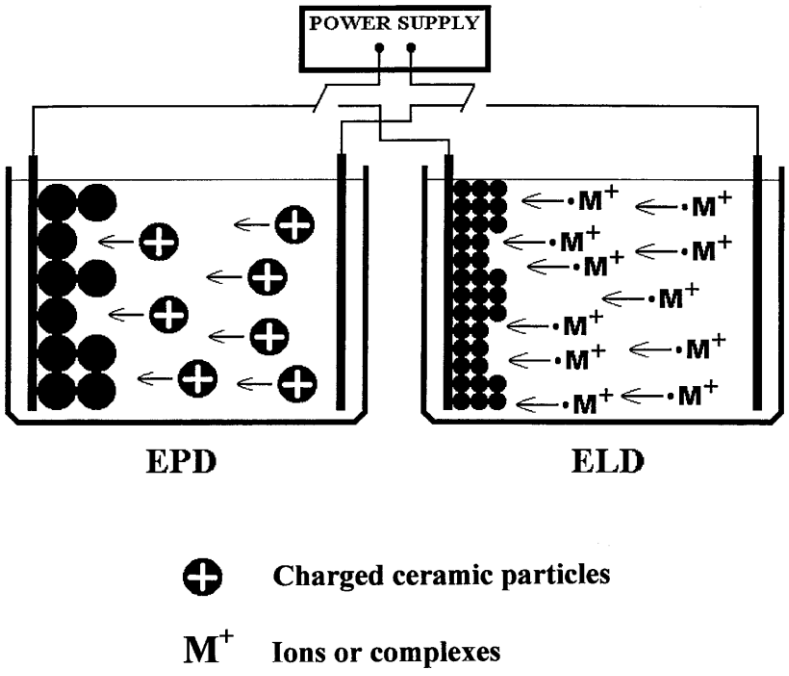

Figure 2-11 Schematic of cathodic EPD and ELD[100]

EPD method has been widely used and continues to being used in many technologies such as fuel cells, ESs, protective coatings, solar cells and so on. Researchers mostly focused on the development of charging additives, dispersants and binders for the EPD of ceramic particles and composites. In this work, anodic process has been used due to lower cost compared to cathodic process. However, oxidation is one of the major disadvantages of anodic process.

Typically, there are two kinds of solvents, water and organic liquids, used for EPD and ELD (Table 2)[100]. The solvents used in electrodeposition must dissolve inorganic salts and organic additives and should be inert with respect to the powder (EPD) and ions (ELD)[100]. It should be referred that the adsorbed water in deposits can result in shrinkage

and cracking during drying while non-aqueous solvents prevent the deposits from hydrating. Consequently, in order to obtain a crack-free deposit by ELD, while the sufficient amount of water is required for the formation of particles, mixed solvents such as the methanol-water or ethanol-water systems, are favoured.

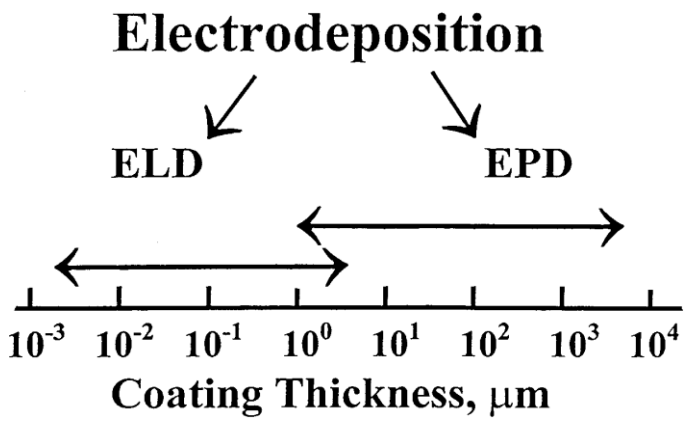

Figure 2-12 Thickness of films deposited using ELD and EPD[100]

The organic liquids are superior to water as a suspension media for EPD. The use of water-based suspensions causes gas formation from the hydrolysis of water, preventing the deposition of uniform adherent layers and yielding pinholes. However, the addition of inorganic salts to the suspensions and the adsorption of ions on ceramic particles can result in deposit contamination. The charges of the colloidal particles could originate from the adsorbed polyelectrolytes or dispersants[101]. Nevertheless, the application of relatively large polyelectrolyte macromolecules for the EPD of nanomaterials presents difficulties related to the bridging flocculation of the nanoparticles[100]. The use of advanced dispersing agents with functional groups containing phosphorus[102] and sulphur[103] introduces inherent problems related to deposit contamination. Despite the

impressive progress achieved in the EPD of various materials, there is a need for simple and versatile methods for the efficient dispersion, charging and deposition of ceramic nanoparticles[101].

Table 2 Features of two processes[100]

Table 2. Electrophoretic and Electrolytic Deposition of Ceramic Materials		
	Electrophoretic Deposition	**Electrolytic Deposition**
Medium	Suspension	Solution
Moving Species	Particles	Ions or complexes
Electrode Reactions	None	Electrogeneration of OH- and neutralization of cationic species
Preferred Liquid	Organic solvent	Mixed solvent (water-organic)
Required Conductivity of Liquid	Low	High
Deposition Rate	1-10^3 μm/min	10^{-3}-1 μm/min
Deposit Thickness*	1-10^3 μm	10^{-3}-10 μm
Deposit Uniformity†	Limited by size of particles	On nm scale
Deposit Stoichiometry	Controlled by stoichiometry of powders used for deposition	Can be controlled by use of precursors
*Controlled by variation of deposition time, voltage, or current density. † Controlled by electric field.		

For enhancing the adherence and strength of the deposited material and preventing cracking, binders are usually added to suspensions or solutions. The particle size and particle surface area decide the optimal amount of binder. Chemical compatibility of components, solubility of binder and additives, viscosity and electric resistivity of the suspension are important points while choosing a binder-dispersant-solvent system. Nonionic-type polymers (polyvinyl alcohol, polyvinyl butyral, ethyl cellulose, and polyacrylamide) are mostly used as binders in EPD. In order to achieve a crack-free

deposit by ELD, while maintaning sufficient amount of water, which is required for the formation of particles, mixed solvents in the methanol-water or ethanol-water systems, are favoured. Some binders, such as poly(dimethyldiallylammonium chloride) (PDDA) or polyethylenimine (PEl) with inherent binding properties, are favoured in ELD as well as EPD and can diminish the cracking problem in electrolytic deposits[104].

The particles in suspensions must be electrically charged and well dispersed to permit electrophoresis in an EPD process. In aqueous media, the charge at the particle-solvent interface could originate from adsorption or desorption of ions, or dissociation of surface groups. Surfaces of oxide particles dispersed in water tend to coordinate water molecules to form hydroxylated surfaces. The hydroxylated surfaces can be positively or negatively charged depending on the pH[100]. Alcohols behave as proton donors for particle charging as well[105], and can ionize to RCH_2O^- and $RCH_2OH_2^+$. Besides, there are a variety of additives that can be used to control particle charge in suspensions. Acids, cations (Mg^{2+}, Ca^{2+}, Al^+, etc.), organic marco-molecules can be used as charging agents in suspensions. The bath compositions for EPD included various additives, which provided stabilisation and charging of inorganic particles in the suspensions[100]. Several investigations were focused on the development of new mechanisms of particle charging and the study of the influence of charging additives on the deposition rate[106].

In a typical ELD process, the deposition is achieved by passing an electric current between two electrodes immersed in an electrolyte. The deposition current and the cell potential are the most important factors to determine the course of the reactions. In a

galvanostatic synthesis, a delicate control can be exercised over the rate of the reaction leading to deposits with good adhesion and a controlled morphology, while a potentiostatic synthesis, yield a pure single phase product corresponding to the applied potential. ELD can be achieved by anodic deposition and cathodic deposition techniques.

2.6.1.1.1 Electrodeposition of manganese oxides

Manganese oxides in various crystalline and amorphous forms have been widely formed on conductive substrates. EPD and ELD methods have been developed for the deposition of nanostructured MnO_2 films[101]. $MnSO_4 \cdot 5H_2O$ electrolyte has been investigated for an anodic ELD method by Hu et al.[75]. Meanwhile, Chang et al.[107] obtained anodic deposits from $Mn(CH_3COO)_2$ by ELD. Chen et al.[108] compared the electrochemical behaviour of hydrous manganese oxide from different manganese precursors by anodic ELD, such as $Mn(CH_3COO)_2 \cdot 4H_20$ $MnSO_4 \cdot 5H_2O$, $MnCl_2 \cdot 4H_2O$ and $Mn(NO_3)_2 \cdot 4H_20$. Electrochemical oxidation of the films resulted in the formation of electrochemically active MnO_2 phase, which showed high capacitance. On the other side, manganese oxide particles can be deposited in the ethanol suspensions. According to Cheong et al.[109] the well dispersed and stable suspensions of manganese oxide particles can be obtained using sodium alginate as an additive and manganese oxide can be positively charged and deposited by EPD. Also Chen et al.[110] achieved cathodic EPD of manganese oxide powder using sulphuric acid as additive in ethyl alcohol.

2.6.1.2 Composite electrodes

The manufacturing of efficient ES requires higher materials loadings using light weight current collectors. Many successful efforts have been made in the area of the fabrication of composite materials, where higher electronic conductivity has been achieved by the use of conductive additives[6, 7, 111]. The SC of 72 F g^{-1} in the 0.1 M K_2SO_4 electrolyte was reported for composite manganese dioxide - acetylene black electrodes with material loading in the range of 10-40 mg cm^{-2} [111].

The porous current collectors improve performance of the electrochemically active materials. Therefore, porous nickel foams are used in industry as advanced current collectors for nickel-cadmium, nickel-metal hydride, nickel-zinc, and lithium ion batteries[112, 113]. For instance, in the batteries, nickel foams contain active material within their light weight web, which provides structural strength, improves electrolyte access to the active material, provides high electronic conductivity and reduces contact resistance. Composite electrodes are produced by pasting slurry of active material into porous nickel foam, followed by impregnation, drying and calendering. The high porosity and large pore size of nickel foams allow for easy impregnation of the active material slurry into the porous current collectors. However, the increase in foam porosity resulted in reduced electronic conductivity but this problem has been addressed by the use of conductive additives[112].

Chapter 3 Objectives

Manganese oxides have become very promising material for ESs applications. However there are certain drawbacks related to the fabrication of MnO_2 electrodes such as:

- Highly agglomerated powders:
    - $KMnO_4$ reacts with organic dispersants
    - Only very DILUTE suspensions of MnO_2 nano-particles can be obtained and stabilized
    - MnO_2 can be easily reduced to form other oxides which are not electrochemically active
    - High electronic and ionic conductivity is required for charge/discharge

The objective of this research is;

- Development of advanced composite electrodes for electrochemical supercapacitors.
- Development of common dispersing agents for simultaneous dispersion of MnO_2, carbon nanotubes and graphene.
- Development of EPD and colloidal casting methods for fabrication of composites.
- Design, investigation of microstructure, and electrochemical behaviour of advanced electrodes for supercapacitors.

Chapter 4 Experiment Procedures

4.1 Materials

The following materials were purchased from Sigma Aldrich Co., USA;

(i) $KMnO_4$

(ii) 3,4-dihydroxybenzoic acid (DHB)

(iii) 3,4-dihydroxyphenylacetic acid (DHP)

(iv) 3,4-dihydroxyhydrocinnamic acid (DHC)

(v) 3,4,5-trihydroxybenzoic acid (THB)

(vi) Hydrocinnamic acid (HCA)

(vii) 3-(4-hydroxyphenyl)propionic acid (HPA)

(viii) Salicyclic acid (SCA)

(ix) 2,3,4-trihydroxybenzoic acid (THBA)

(x) 3-5-dihydroxybenzoic acid (DHBA)

(xi) Phthalic acid (PA)

(xii) 1,2,3-Benzenetricarboxylic acid hydrate (BTC)

(xiii) Aurintricarboxylic acid (ATA)

(xiv) Aurintricarboxylic acid ammonium salt (aluminon)

(xv) Ethanol

Additionally,

(xvi) Multiwalled carbon nanotubes (MWCNTs) were supplied by Arkema Inc., USA

(xvii) Graphene was purchased from Graphene Supermarket, USA company

(xviii) Polyvinyl butyral (PVB) was purchased from Richard E.Mistler, Inc.

4.2 Synthesis of MnO_2

Manganese dioxide powders for EPD were prepared by the reduction of 0.2M $KMnO_4$ aqueous solutions with ethanol using the reduction reaction:

$$4MnO_4^- + 3CH_3CH_2OH + 4H^+ \rightarrow 4MnO_2 + 3CH_3COOH + 5H_2O \qquad (4\text{-}1)$$

Mixing was performed by the slow addition of ethanol to the $KMnO_4$ solution. A dark-brown suspension was obtained. Stirring was performed using a magnetic bar at room temperature during 20 h. The powder, obtained by the filtration of the suspension, was washed with water to remove potassium ions. Drying was performed in air at 20 ^oC[114]. The preparation process is shown in Figure 4-1.

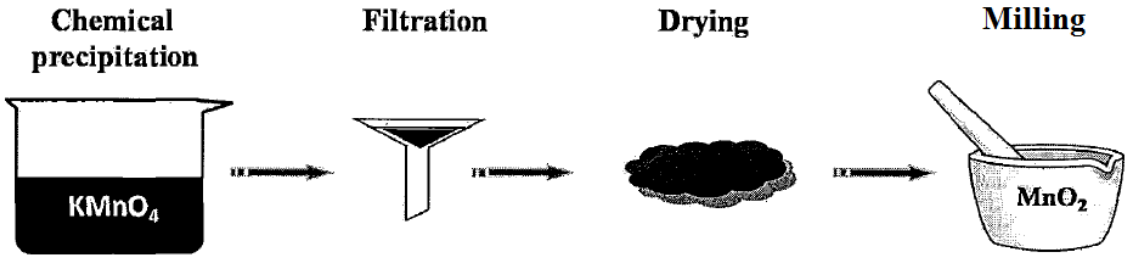

Figure 4-1 The preparation process of MnO_2

4.3 Experimental setup for electrodeposition

Electrophoretic deposition method was employed for the fabrication of MnO_2.MWNTs, MnO_2-graphene nanoparticle composite films. The electrodeposition cell included a substrate centered between two Pt counter electrodes. Platinum plates were placed on either side of the stainless steel substrate separated at a distance of 15 mm. The time of deposition was varied from 1 to 8 minutes. After deposition, the stainless steel substrate with film deposited is allowed to dry at room temperature for 48 h. The schematic diagram of electrodeposition process is shown in the Figure 4-2.

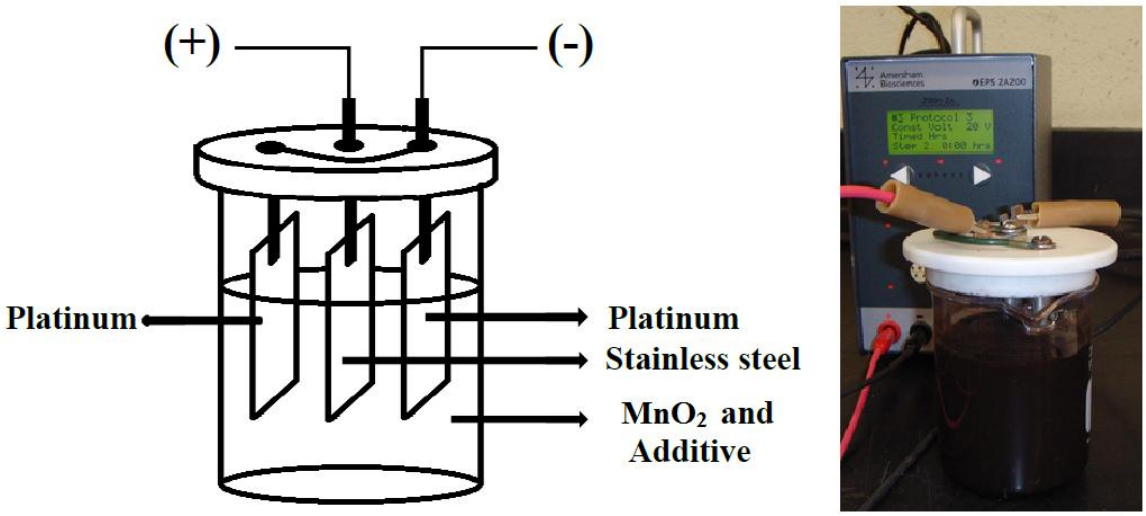

Figure 4-2 Schematic representation of experimental set-up in electrodeposition.

The volume of the cell was 280 ml. An electrophoresis power supply EPS 601 (Amersham Biosciences) was employed to provide the DC electric field for electrodeposition, using a constant voltage mode.

4.4 Electrodeposition procedures

Anodic deposits were obtained on various conductive substrates under constant current or constant voltage conditions. These substrates include stainless steel 304 foils (25x50x0.1 mm), Nickel Plaque (10x30x0.3 mm), Pt foils (50x50x0.l mm) and platinized silicon wafers (10x50x1.5 mm). Schematic illustration of Nickel Plaque and platinized silicon wafers experimental set-up is as same as stainless steel procedures shown in Figure 4.2.

Electrophoretic deposits were obtained on stainless steel substrates from the 4 - 10 g L^{-1} MnO_2 suspension in ethanol. The concentrations of DHB, DHP, DHC, THB, HCA, HPA, SCA, THBA, DHB, DHBA, ATA, PA, and BTC in the suspensions were varied in the range of 0–0.5 g L^{-1}. Before the deposition, the suspensions were ultrasonicated for 10 min in order to achieve a homogeneous dispersion of the MnO_2 particles. The deposition was performed at a constant voltage of 20 V. High voltage offers the advantage of high deposition rate. However, gas evolution at high voltages can result in low deposit adhesion.

EPD was also performed from 0-1 g L^{-1} aluminon suspension in water, containing 0.5 g L^{-1} MWCNTs and graphene or 10 g L^{-1} MnO_2 suspension in water, containing 0.5 g L^{-1} MWCNTs and 0-0.5 g L^{-1} THBA, and ATA as a dispersing and charging agent. The EPD cell included a substrate and Pt counter electrode. The deposition voltage of aluminon was in the range of 7–10 V in order to reduce gas evolution.

4.5 Slurry procedure

The slurry was prepared by mixing the MnO_2 powders with MWCNT, ATA and polyvinyl butyral (PVB) binder. The slurry was then impregnated in to the porous INCOFOAM® current collectors followed by drying and calendering to desired thickness[112]. INCOFOAM® current collectors with a volumetric porosity of 95% were made by Vale Inco using carbonyl technology[113]. The total mass of slurry in the composite electrodes was 20-55 mg cm^{-2}. A schematic representation of the electrode fabrication process by impregnation of Nickel Foam current collector is shown in Figure 4-3.

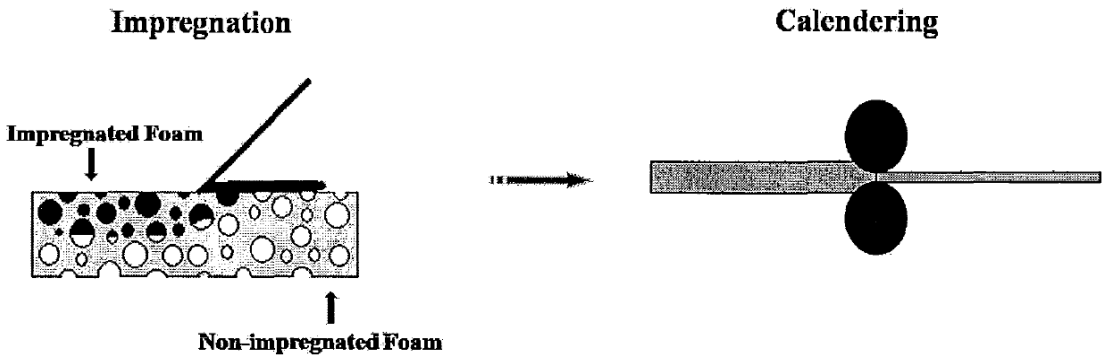

Figure 4-3 Fabrication of nickel foam based electrodes by impregnation

4.6 Materials Characterization

4.6.1 Investigation of deposition yield

A Mettler Toledo AXI0S DeltaRange analytical balance, which has a readability of 0.01 mg, was used to measure the weight of the foil substrate before and after the deposition, followed by drying at room temperature for 24 hr. Then the weight of a deposited coating was obtained.

4.6.2 Thermogravimetric and differential thermal analysis

Thermogravimetric analysis (TGA) is an analytical technique used to determine a material's thermal stability and fraction of volatile components by monitoring the weight change that occurs as a specimen is heated. In addition to weight changes, the instruments also record the temperature difference between the specimen and one or more reference pans (differential thermal analysis, DTA) , which can be used to monitor the energy released or absorbed via chemical reactions or phase transformations during the heating process.

In this work, the deposits removed from stainless steel substrates were studied by TGA and DTA, which were carried out in air between room temperature and 800°C at a heating rate of 5°C min^{-1} using a thermo analyzer (Netzsch STA-409)

4.6.3 Scanning electron microscopy

The scanning electron microscope (SEM) is a type of electron microscope that images the sample surface by scanning it with a high-energy beam of electrons in a scan pattern. The electrons interact with the atoms that make up the image producing signals that contain information about the sample's surface topography, composition and other properties.

The microstructures of the deposited films were investigated by SEM using a JEOL JSM-7000F scanning electron microscope equipped with Energy Dispersive Spectroscopy (EDS). The samples for SEM observations of film surfaces and cross sections were obtained by EPD of polymer and composite films on platinized silicon wafers. The samples were placed on a conductive sample holder using a conductive adhesive copper tape.

4.6.4 Fourier transform infrared spectroscopy

Fourier Transform Infrared Spectroscopy (FTIR) is an analytical technique used to identify organic (and in some cases inorganic) materials. This technique measures the absorption of various infrared light wavelengths by the material of interest. These infrared absorption bands identify specific molecular components and structures. In this work, the deposits removed from stainless steel substrates were studied by FTIR using Bio-Rad FTS-40 instrument.

4.7 Electrochemical Characterization

Electrochemical characterization of the deposited films and fabricated composite electrodes was studied using a potentiostat (PARS-TAT 2273, Princeton Applied Research) controlled by a PowerSuite electrochemical software shown in Figure 4-4. A standard three electrode cell contained a working electrode, a platinum gauze counter electrode and a standard calomel reference electrode (SCE). The surface area of the working electrodes was 1 cm^2. Testing was performed in the 0.5 M Na_2SO_4 aqueous solution, degassed with a purified nitrogen gas.

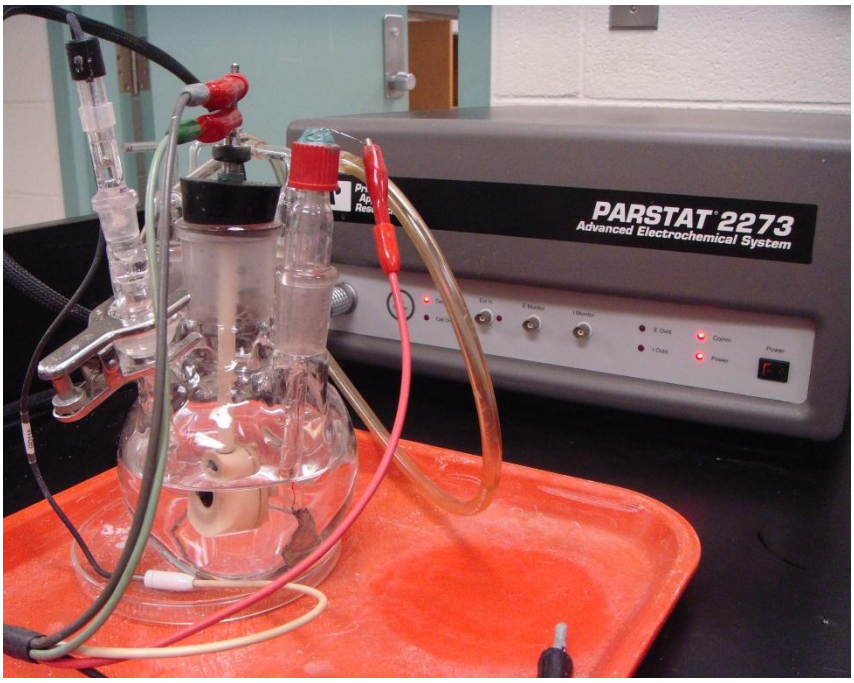

Figure 4-4 Schematic representation of experimental set-up with potentiostat.

Cyclic voltammetry (CV) measures charge-response with regard to a charging voltage, and is therefore a means of evaluating capacitance. In CV analysis, a series of charging

voltages at a constant sweep rate (dV/dt) are applied and the current response is recorded. An ideal capacitor with no resistance would display a rectangular shape. CV studies were performed within a potential range of 0 – 0.9 V vs. SCE at scan rates of 2 - 100 mV s^{-1}.

The ES was calculated using half the integrated area of the CV curve to obtain the charge (Q), and subsequently dividing the charge by the mass of the film (m) and the width of the potential window (ΔV):

$$C=Q/m\Delta V \qquad (4\text{-}2)$$

Faster sweep rates correspond to charging and discharging at higher power levels. Multiple plots obtained at increasing sweep rates are therefore often displayed on the same graph to demonstrate the impact of power levels on the charging characteristics. From such plots it is evident that capacitance decreases at higher frequencies.

In addition to cyclic voltammetry, electrochemical impedance spectroscopy (EIS) is a useful method to measure complex impedance of electrochemical cells. Figure 4-5 shows the equivalent circuits for an electrolytic capacitor and involves the following circuit elements: the double-layer capacitance C_{dl} a Faradaic reaction resistance R_F, a pseudocapacitance C_p, and the resistance of electrolyte R_s. At low frequency, the real part of the impedance approximately equals to the sum of R_F and R_s while at high frequency, the real part of the impedance equals to R_s. The complex impedance Z*=Z'-iZ" for the fabricated electrodes was investigated in the frequency range of 0.1 Hz- l00 kHz at a voltage of 10 mV.

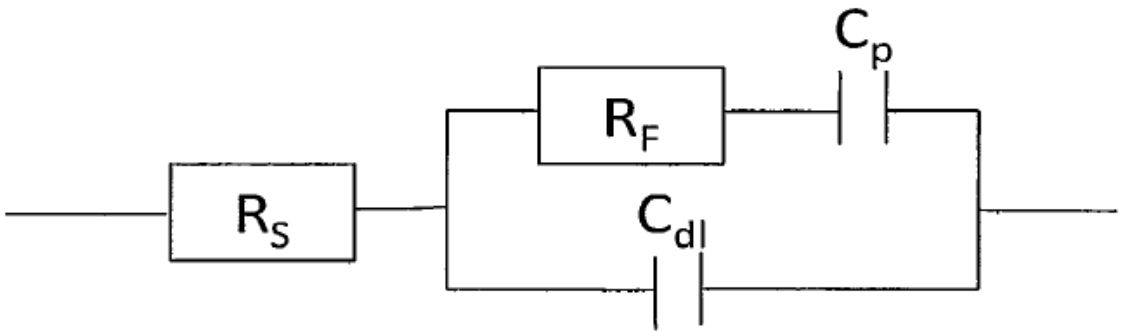

Figure 4-5 Equivalent circuit of a ES[1].

The deposition process has also been studied using a quartz crystal microbalance (QCM 922, Princeton Applied Research) controlled by a computer using a PowerSuite electrochemical software.

The mass Δm of adsorbed material was calculated using Sauerbrey's equation:

$$-\Delta F = \left[\frac{2F_0^2}{A\sqrt{\rho_q \mu_q}}\right]\Delta m \qquad (4\text{-}3)$$

where ΔF is frequency decrease of the QCM, F_0 is the parent frequency of QCM (9 MHz), A is the area of gold electrode (0.2 cm^2), ρ_q is the density of the quartz (2.65 g cm^{-3}) and μ_q is the shear modulus of quartz (2.95 x 10^{11} dyne cm^{-2}).

Chapter 5 Experimental Results and Discussion

5.1 Electrodeposition of MnO_2 with dispersing agents

One of the major issues in the ceramic processing by EPD is the fabrication of stable suspensions of charged nanoparticles. The choice of dispersing agents is extremely important for the development of EPD nanotechnology. A critical property of a dispersant is its adsorption on the particle surface. Therefore, there is a need for the development of advanced dispersing agents with strong interfacial adhesion. The approach developed in this investigation is based on the use of small organic molecules, which provide adhesion to the metal oxide surface via the complexation of metal ions at the particle surface. The strategy has emerged from the investigations of the mechanism of strong mussel adhesion to metal and mineral surfaces[115, 116]. The mussel adhesive proteins were found to have a high concentration of a catecholic amino acid, L-3,4 –dihydroxyphenylalanine (DOPA), which interacts strongly with inorganic surfaces[115]. The proposed mechanism of chemisorption of DOPA onto the oxide surface involved the deprotonation of the phenolic hydroxyl groups of the catechol and chelation of metal ions on the particle surface. However, the adsorption mechanism is not well understood.

5.1.1 Electrodeposition of MnO_2 with DHB, DHP, DHC, THB, HCA and HPA

Figure 5-1 shows chemical structures of the organic molecules used in this study. DHB, DHP, DHC contain two adjacent OH groups, bonded to the aromatic ring. Similar to DOPA, they belong to the catechol family. The length of hydrocarbon chains increases in

the order DHB<DHP<DHC. The structure of THB is similar to that of DHB, but it contains 3 adjacent OH groups. The structures of HCA and HPA are similar to the structure of DHC. However, HCA does not have OH groups bonded to the aromatic ring, whereas HPA has only one OH group (Figure 5-1). All the organic molecules contained a COOH group.

The organic molecules (Figure 5-1) were investigated for the dispersion and charging of MnO_2 nanoparticles for application in EPD. The suspensions of MnO_2 in ethanol were unstable, and exhibited relatively fast sedimentation after ultrasonication. The results presented below showed that the addition of DHB, DHP, DHC, and THB to the suspensions of MnO_2 nanoparticles resulted in improved suspension stability. However, no improvement in the stability of MnO_2 suspensions was observed after the addition of HCA and HPA. The improved stability of the suspensions, containing DHB, DHP, DHC and THB can be attributed to the adsorption of the organic molecules on the MnO_2 nanoparticles. It was suggested that the adsorbed molecules, containing dissociated COOH groups, provided electrosteric repulsion of the MnO_2 nanoparticles. Moreover, the dissociation of the COOH groups provided a negative charge required for the EPD of MnO_2.

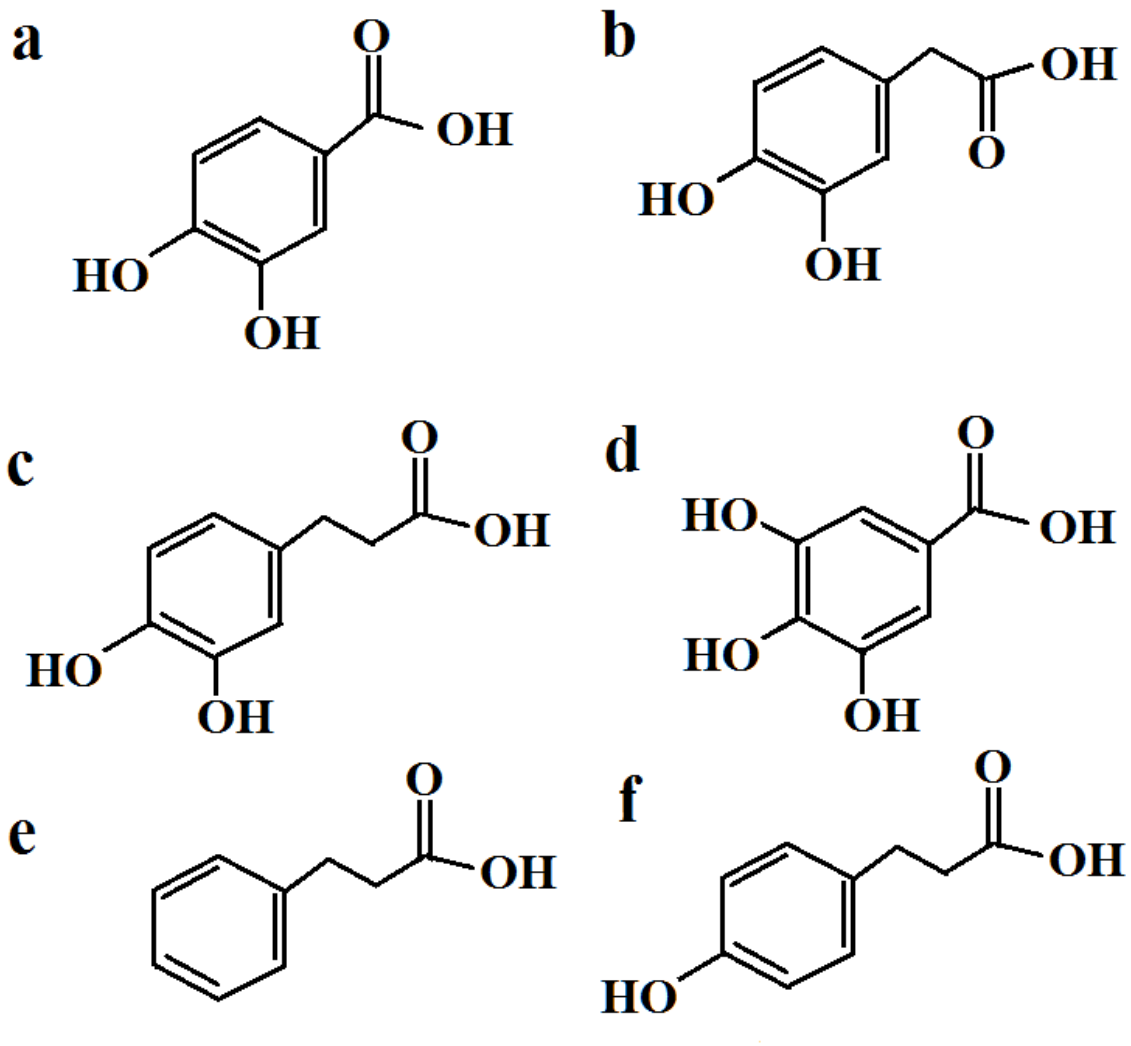

Figure 5-1 Chemical structures of (a) DHB, (b) DHP, (c) DHC, (d) THB, (e) HCA and (f) HPA

5.1.1.1 Effect of the concentration

Anodic EPD was achieved from the MnO_2 suspensions containing DHB, DHP, DHC and THB. The formation of the anodic deposits indicated that MnO_2 nanoparticles, containing

adsorbed organic molecules, were negatively charged. In contrast, no EPD was achieved from the MnO_2 suspensions containing 0-0.5 g L^{-1} of HCA or HPA. Figure 5-2 shows the deposited mass as a function of concentration of DHB, DHP, DHC and THB in the MnO_2 suspensions. No deposition was observed at DHB, DHP, DHC concentrations in the range of 0-0.05 g L^{-1} and then a significant increase in the deposition yield was observed at higher concentrations. In contrast, a significant increase in the deposition yield was observed with increasing concentration of THB in the range of 0-0.05 g L^{-1}. The deposition yield at additives concentration in the range of 0.3-0.5 g L^{-1} increased in the order DHB<DHP<DHC (Figure 5-2). The increase in the deposition yield correlates with the increase in the length of the hydrocarbon chains of the corresponding molecules (Figure 5-1). The comparison of the experimental data for DHB, DHP, DHC and THB with the results obtained for HCA and HPA indicated that the adsorption of the molecules on the MnO_2 surface is governed by the interaction of adjacent OH groups of the organic molecules with Mn ions at the particle surface. It is in this regard that DHB, DHP, DHC and THB, containing adjacent OH groups, provided improved suspension stability and enabled EPD of MnO_2 nanoparticles. However, no EPD was observed from the MnO_2 suspensions containing HCA or HPA. As pointed out above, HCA does not have OH groups bonded to the aromatic ring, whereas HPA has only one OH group.

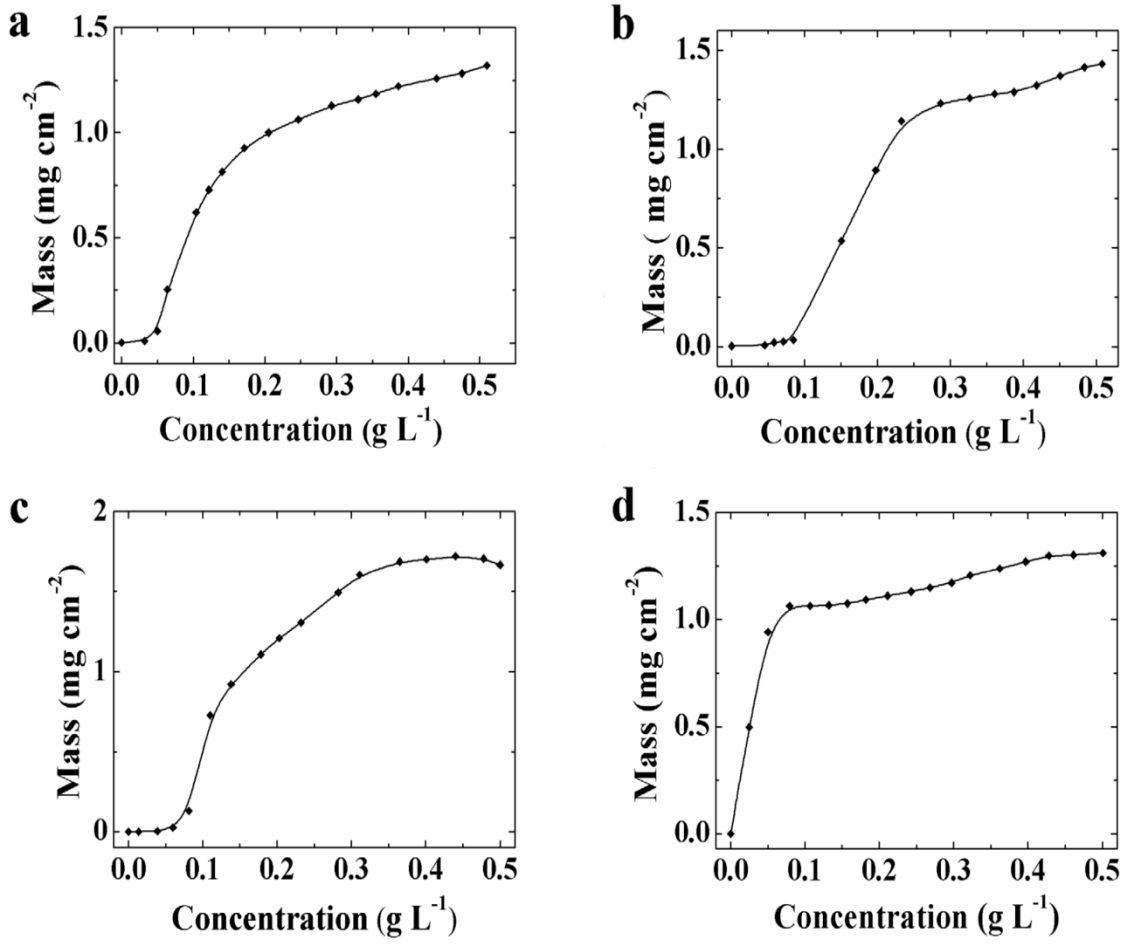

Figure 5-2 Deposit mass as a function of concentration of (a) DHB, (b) DHP, (c) DHC and (d) THB in 4 g L^{-1} MnO_2 suspension at deposition voltage of 20 V and deposition time of 5 min.

5.1.1.2 Adsorption mechanism

It was suggested that DHB, DHP, DHC and THB were adsorbed on the MnO_2 nanoparticles via the mechanism[117] involving the formation of mononuclear or binuclear

chelates (Figure 5-3). The increase in the deposition yield with increasing length of the hydrocarbon chain in the order DHB<DHP<DHC was attributed to improved dispersion, provided by the molecules with longer hydrocarbon chains. It is in this regard that the deposition rate depends on particle concentration in the suspension[118]. Therefore, particle sedimentation results in a reduced deposition rate. The comparison of the deposition yield data (Figure 5-2) for the DHB and THB indicated that THB, containing 3 OH groups (Figure 5-1), is more efficient charging additive at low concentrations in the range below 0.1 g L^{-1}. However, no significant difference in the deposition yield data (Figure 5-2) was observed in the concentration range of 0.3-0.5 g L^{-1} for DHB and THB.

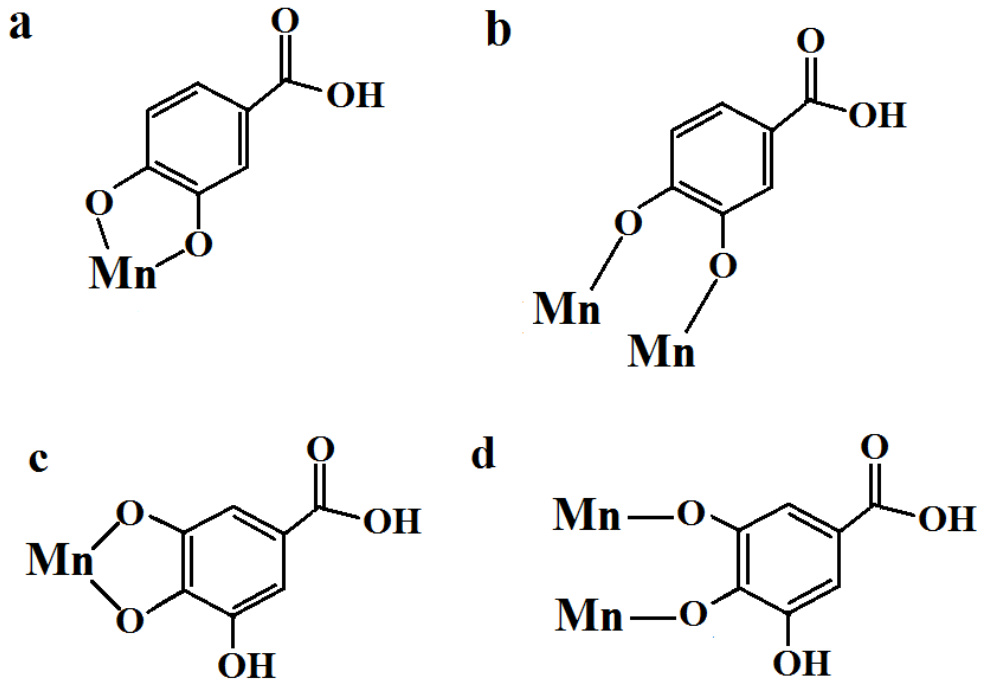

Figure 5-3 Possible coordination structures formed by chemisorption of (a, b) DHB and (c, d) THB; (a, c) mononuclear and (b, d) binuclear chelating.

5.1.1.3 Effect of the deposition time

Figure 5-4 shows deposit mass as a function of the deposition time for the deposits prepared from 4 g L^{-1} MnO_2 suspensions containing 0.5 g L^{-1} of DHB, DHP, DHC and THB. The deposit mass increased with increasing deposition time. Therefore, the amount of the deposited material can be varied.

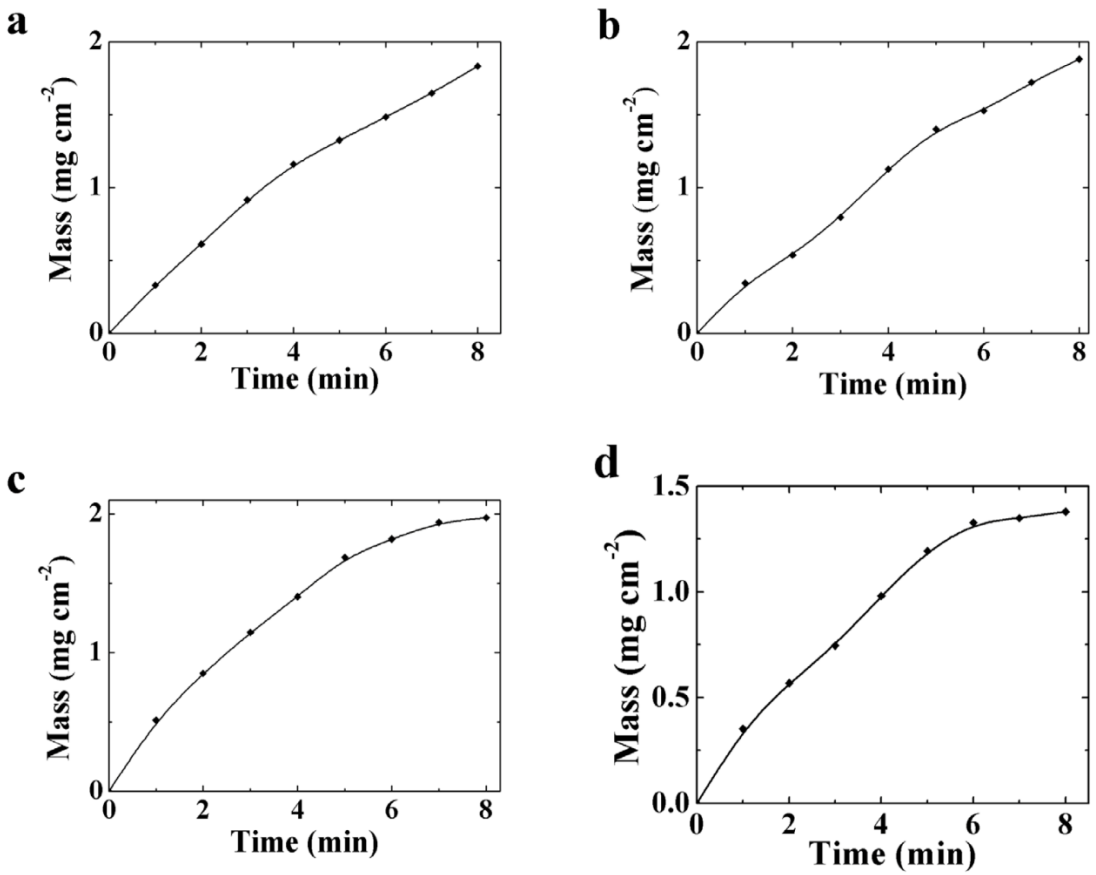

Figure 5-4 Deposit mass as a function of deposition time for 4 g L^{-1} MnO_2 suspensions containing 0.5 g L^{-1} of (a) DHB, (b) DHP, (c) DHC and (d) THB at a deposition voltage of 20 V.

The slopes of the curves decreased with increasing deposition time, indicating the decrease in the deposition rate. The decrease in the deposition rate at constant voltage EPD was observed in other investigations[119]. Such behaviour is usually attributed to the increasing voltage drop in the growing deposits and corresponding reduction in the voltage drop and electric field in the bulk of the suspension.

5.1.1.4 FTIR studies

The films prepared by EPD were investigated by FTIR method. The FTIR spectra (Figure 5-5) showed broad peaks centered at 3413 (a), 3418 (b), 3420 (c), and 3420 (d) cm^{-1} which were related to the stretching vibrations of OH group of adsorbed water molecules[120]. The bands at 1633 (a), 1628 (b), 1629 (c), and 1624 (d) cm^{-1} were attributed C-C vibrations[121] of adsorbed DHB, DHP, DHC and THB, respectively. The bands at 1385 (a), 1404 (b), 1395 (c) and 1404 (d) cm^{-1} represented the stretching vibrations of carboxyl groups of the adsorbed organic molecules[121, 122]. The bands at 1050 (a), 1051 (b), 1049 (c), and 1035 (d) cm^{-1} were attributed to the aryl-oxygen stretching vibrations of the molecules[123]. The broad bands at 559 (a), 554 (b), 552 (c), and 559 (d) cm^{-1} were related to the characteristic absorptions[120] of MnO_2. The results of FTIR investigation, coupled with the results of the deposition yield measurements, indicated the adsorption of the organic molecules on the surfaces of MnO_2 nanoparticles.

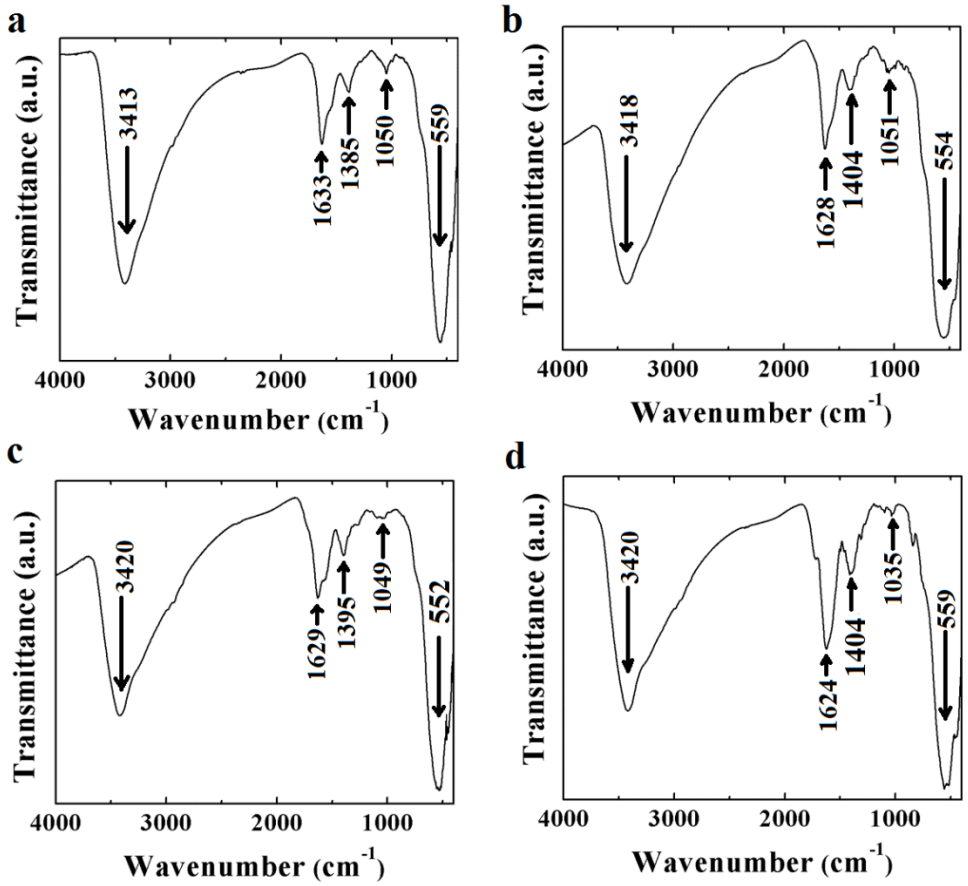

Figure 5-5 FTIR spectra for deposits prepared from 4 g L^{-1} MnO_2 suspensions containing 0.5 g L^{-1} of (a) DHB, (b) DHP, (c) DHC, and (d) THB.

5.1.1.5 SEM studies

SEM investigations of as prepared powders showed that some primary nanoparticles formed agglomerates, which were also observed in the deposited films. Figure 5-6 indicates that a more uniform distribution of MnO_2 nanoparticles with reduced particle agglomeration can be achieved adding DHB dispersant into the starting solution for powder preparation. The SEM images (Figure 5-6B) indicated that the films were crack

free. The small pores can be attributed to packin of MnO_2 nanoparticles, whereas larger pores can be attributed to gas evolution at the electrode surface during EPD.

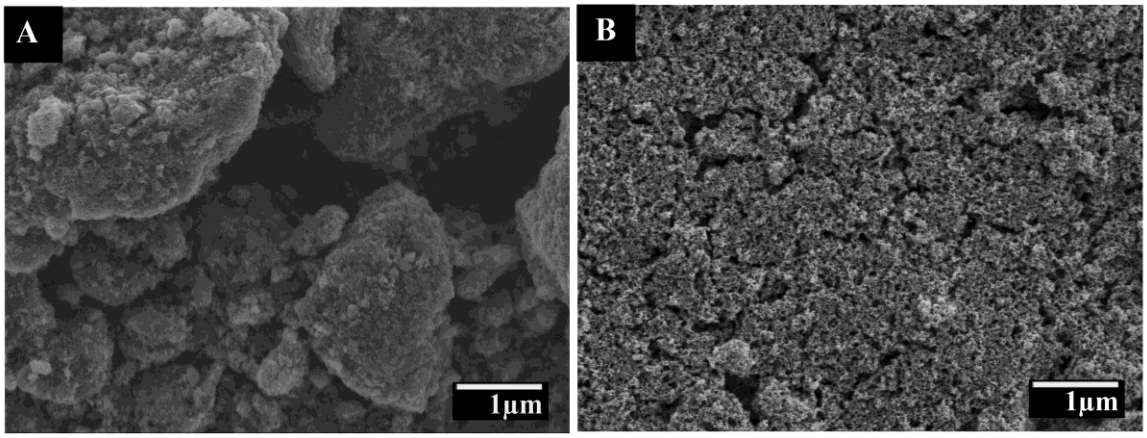

Figure 5-6 SEM images of the film prepared using DHB. (A) Agglomerated film and (B) reduced agglomerated film with same magnification.

5.1.2 Electrodeposition of MnO_2 using SCA, DHB, THBA, DHBA, PA and BTC as charging and dispersing agents

The results presented above indicated that two adjacent OH groups bonded to the aromatic ring provided catecholate type of bonding and allowed adsorption of molecules on particle surface and dispersion of MnO_2 nanoparticles. The efficiency of dispersion is influenced by the length of the hydrocarbon chain. It is important to compare the efficiency of catecholate, salicylate and carboxylate bonding and further analyze the

influence of the molecular structure on the dispersion mechanism. Figure 5-7 shows chemical structures of the organic molecules used in this study. All the molecules contain carboxylic groups. The dissociated carboxylic groups provided a charge for electrosteric dispersion and electrophoretic deposition. SCA contains adjacent OH and carboxylic group, DHB contains two adjacent OH groups, and THBA contains three adjacent OH and a carboxlic group, bonded to the aromatic ring. Similar to DOPA, DHB belongs to the catechol family. DHBA contained two OH groups and one carboxylic group, bonded to non-adjacent carbon atoms of the aromatic ring. PA and BTC do not have OH groups bonded to the aromatic ring. PA and BTC have two and three adjacent carboxlic groups, respectively (Figure 5-7).

The organic molecules (Figure 5-7) were investigated for the dispersion and charging of MnO_2 nanoparticles for application in EPD. The suspensions of MnO_2 in ethanol were unstable, and exhibited relatively fast sedimentation after ultrasonication. Sedimentation experiments showed that the addition of SCA, DHB, and THBA to the suspensions of MnO_2 nanoparticles resulted in improved suspension stability. However, the stability of SCA suspension was poor. No improvement in the stability of MnO_2 suspensions was observed after the addition of DHBA, PA and BTC. The improved stability of the suspensions, containing SCA, DHB, and THBA can be attributed to the adsorption of the organic molecules on the MnO_2 nanoparticles. It was suggested that the adsorbed molecules, containing dissociated COOH groups, provided electrosteric repulsion of the

MnO_2 nanoparticles. Moreover, the dissociation of the COOH groups provided a negative charge required for the EPD of MnO_2.

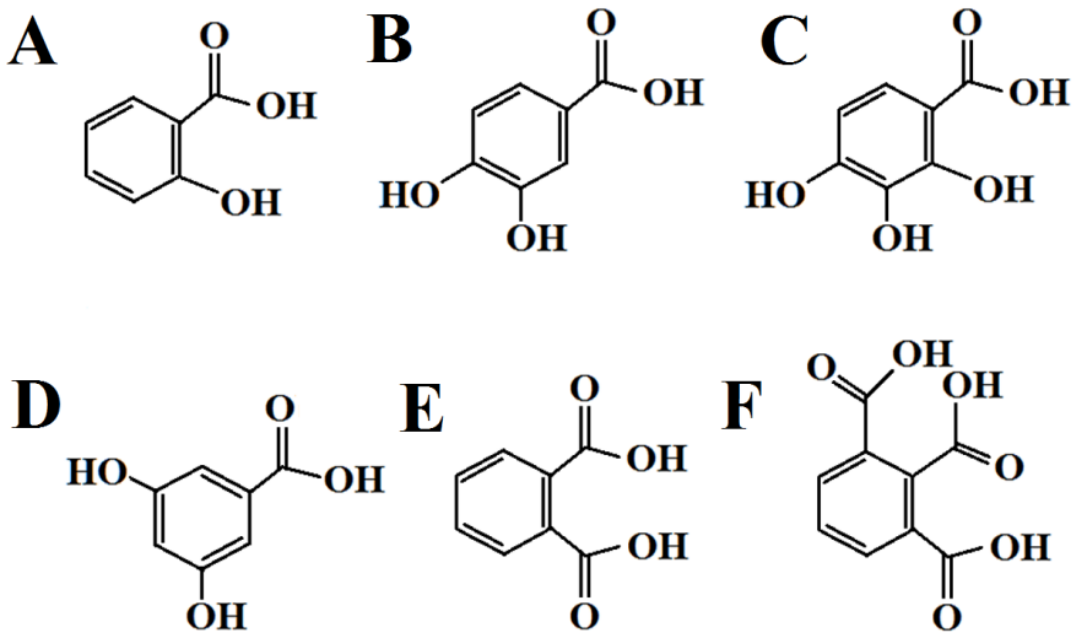

Figure 5-7 Chemical structures of (a) Salicyclic acid (SCA), (b) 3,4-Dihydroxybenzoic acid (DHB), (c) 2,3,4-Trihydroxybenzoic acid (THBA), (d) 3-5Dihydroxybenzoic acid (DHBA), (e) Phthalic acid (PA), (f) 1,2,3-Benzenetricarboxylic acid hydrate (BTC)

5.1.2.1 Effect of the concentration

Anodic EPD was achieved from the MnO_2 suspensions containing SCA, DHB, and THBA. The formation of the anodic deposits indicated that MnO_2 nanoparticles, containing adsorbed organic molecules, were negatively charged. In contrast, no EPD was achieved from the MnO_2 suspensions containing 0-0.5 g L^{-1} of DHBA, PA, and BTC. Figure 5-8 shows deposit mass as a function of concentration of SCA, DHB, and THBA in the MnO_2 suspensions. The increase in SCA concentration in the range of 0-0.45 g L^{-1} resulted in a linear increase in the deposition yield. Further increase in the SCA concentration did not result in significant changes in the deposition yield. On the other hand, no deposition was observed at DHB concentration in the range of 0-0.13 g L^{-1} and at THBA concentration in the range of 0-0.05 gL^{-1}, then a significant increase in the deposition yield was observed at higher concentrations. The deposition yield increased with the increasing concentration of DHB and THBA, showed a maximum at 0.35 g L^{-1}DHB, and 0.28 g L^{-1} THBA and then decreased. The comparison of the experimental data provided an insight into the influence of chemical structure of the molecules on their adsorption on the MnO_2 nanoparticles, dispersion and deposition. The results indicated that the number and position of OH groups are important factors controlling the adsorption behaviour (Figure 5-7). The comparison of the experimental data for SCA, DHB, and THBA with the results obtained for DHBA, PA and BTC indicated that the adsorption of the molecules on the MnO_2 surface is governed by the interaction of adjacent OH and $COOH^-$ groups of the organic molecules with Mn ions at the particle surface. It is in this regard that SCA, DHB, and THBA containing adjacent OH groups or

adjacent OH and carboxylic groups, provided improved suspension stability and enabled EPD of MnO_2 nanoparticles. However, no EPD was observed from the MnO_2 suspensions containing DHBA even though it has two OH groups, bonded to the non-adjacent carbon atoms of the aromatic ring. As pointed out above, PA and BTC do not have OH groups bonded to the aromatic ring, whereas PA and BTC have two $COOH^-$ groups.

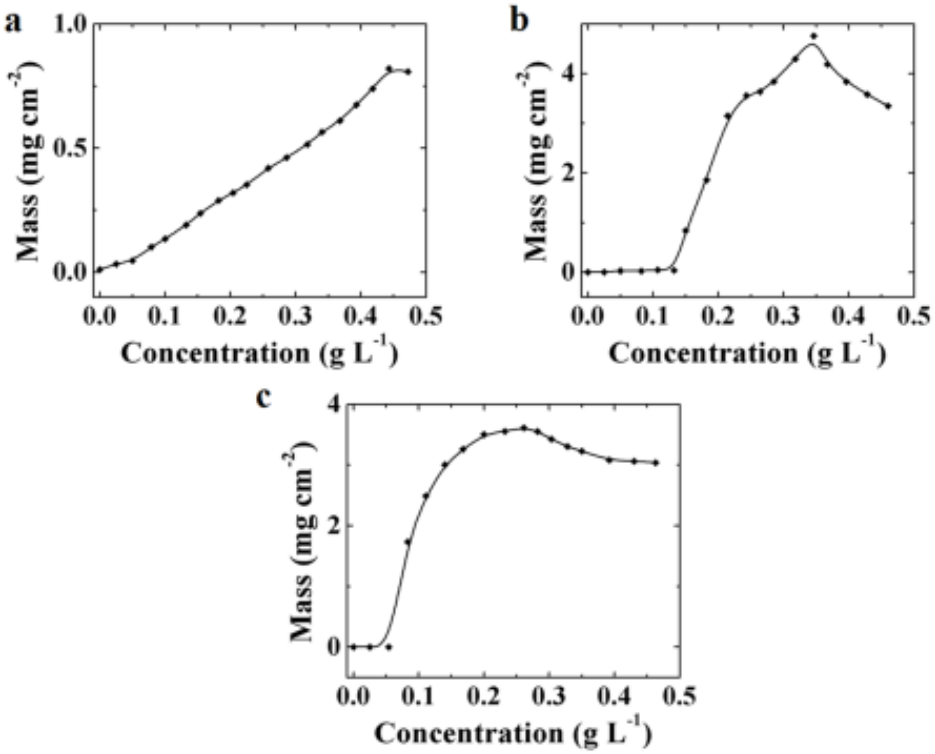

Figure 5-8 Deposit mass as a function of concentration of (a) SCA, (b) DHB, and (c) THBA in 10 g L^{-1} MnO_2 suspension at deposition voltage of 20 V and deposition time of 5 min.

The suspension stability of SCA, DHB and THBA is shown in Figure 5-9. The suspensions, containing DHB and THBA showed significantly higher stability compared to the suspension containing of SCA. For instance, the suspension of SCA, Figure 5-9 (a), precipitated in 1 h. DHB, Figure 5-9 (b), precipitated in a day and THBA, Figure 5-9 (c), remained stable during couple days after ultrasonic agitation.

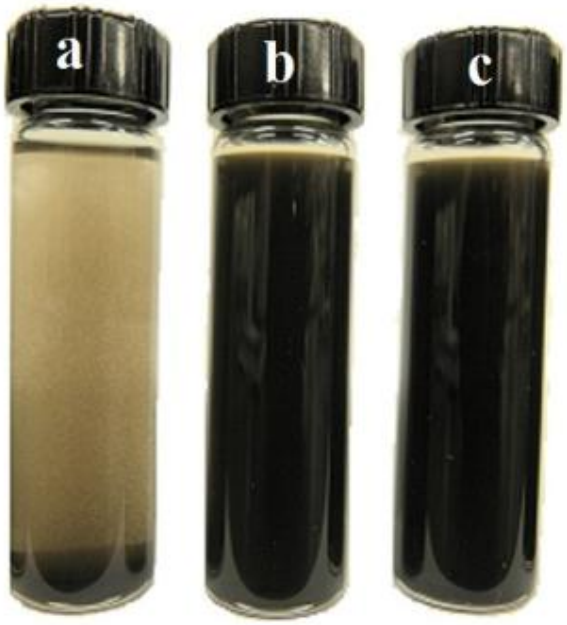

Figure 5-9 comparison of suspension stability of (a) SCA, (b) DHB, and (c) THBA in 10 g L^{-1} MnO_2 suspension with 0.5 g L^{-1} additive concentration after 1 h.

5.1.2.2 Adsorption mechanism

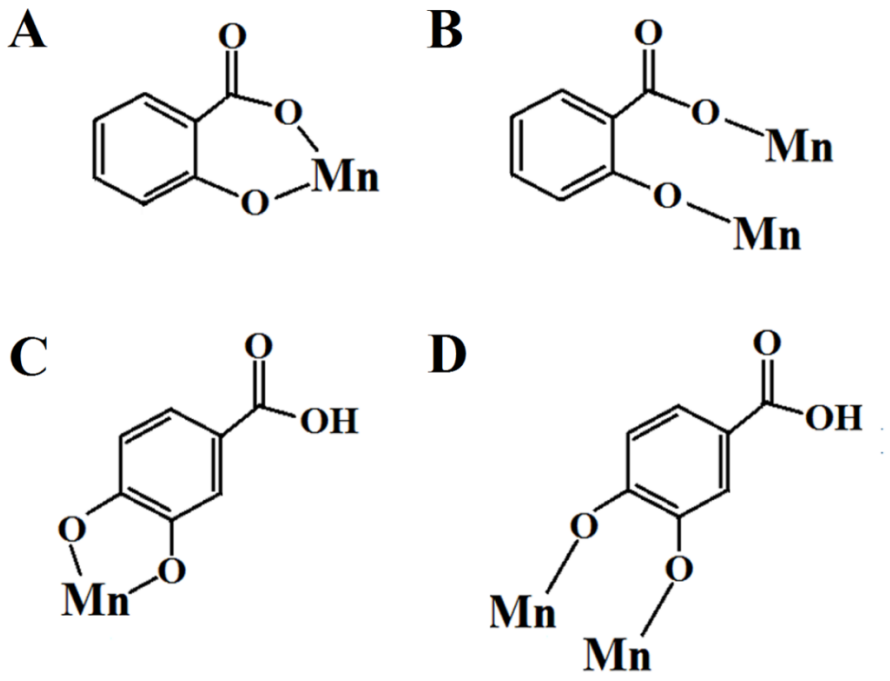

Figure 5-10 Possible coordination structures formed by chemisorption of (A, B) SCA and (C, D) DHB; (A, C) mononuclear and (B, D) binuclear chelating.

The adsorption mechanism of SCA, DHB, and THBA is shown in Figure 5-10. The adsorption depends on the number of OH groups and position of the OH groups in aromatic rings. The increase in the deposition yield in order SCA < THBA < DHB was attributed to improved dispersion. It is in this regard that the deposition rate depends on particle concentration in the suspension[100, 124]. Therefore, particle sedimentation results in a reduced deposition rate. The comparison of the deposition yield data (Figure 5-8) for the SCA and DHB indicated that SCA was containing one OH group, adjacent to $COOH^-$ (Figure 5-7), and DHB was containing two OH groups, not adjacent to COOH group.

SCA deposited at low concentration in range below 0.1 g L^{-1}. However, significant difference in the deposition yield data (Figure 5-8) was observed in the concentration range of 0.15 - 0.5 g L^{-1} for SCA and DHB. Figure 5-10 shows salicylate type of bonding, involving adjacent OH and COOH groups and catecholate type of bonding involving two OH groups. The catecholate type of bonding is much stronger, compared to salicylate type. It results in improved dispersion. Both mechanisms can be suggested for THBA.

5.1.2.3 Effect of the deposition time

Figure 5-11 shows deposit mass as a function of the deposition time for the deposits prepared from 10 g L^{-1} MnO_2 suspensions containing 0.5 g L^{-1} of SCA, DHB, and THBA. The deposit mass increased with increasing deposition time. Therefore, the amount of the deposited material can be varied.

The slopes of the curves decreased with increasing deposition time, indicating the decrease in the deposition rate. The decrease in the deposition rate at constant voltage EPD was observed in other investigations[125]. Such behaviour is usually attributed to the increasing voltage drop in the growing deposits and corresponding reduction in the voltage drop and electric field in the bulk of the suspension.

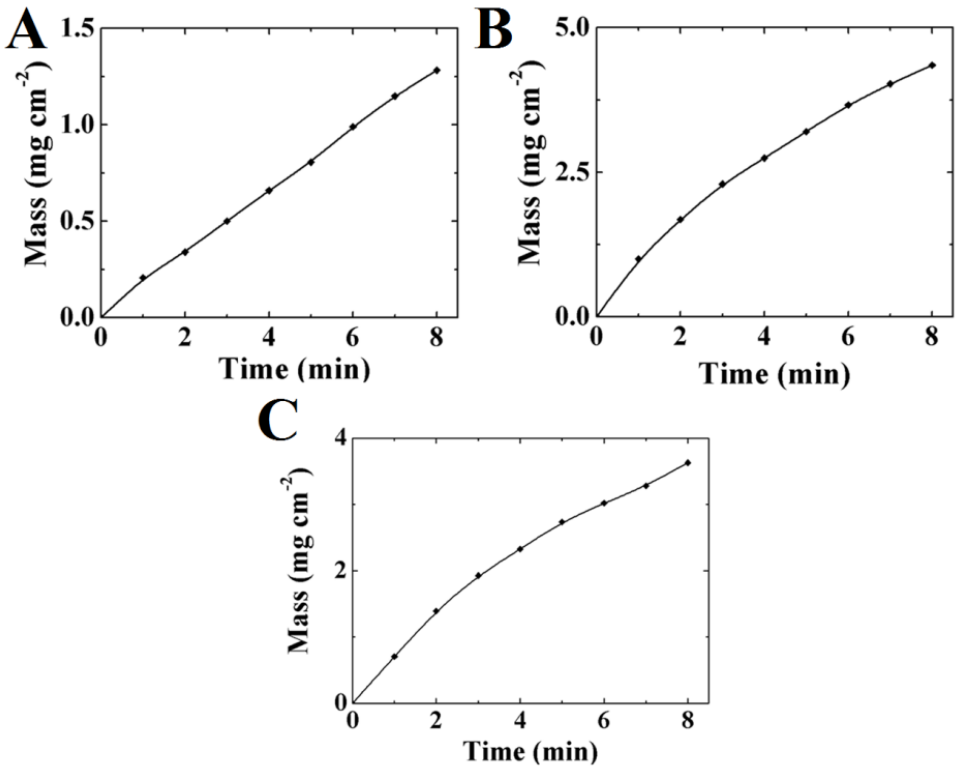

Figure 5-11 Deposit mass as a function of deposition time for 10 g L^{-1} MnO_2 suspensions containing 0.5 g L^{-1} of (a) SCA, (b) DHB, and (c) THBA at a deposition voltage of 20 V.

5.1.2.4 FTIR studies

The films prepared by EPD were investigated by FTIR method. The FTIR spectra (Figure 5-12) showed broad peaks centered at 3375 (a), 3389 (b), and 3380 (c) cm^{-1} which were related to the stretching vibrations of OH group of adsorbed water molecules. The bands at 1601 (a), 1617-1539 (b), and 1624 (c) cm^{-1} were attributed C-C vibrations of adsorbed

SCA, DHB, and THBA, respectively. The bands at 1455-1348 (a), 1539-1384 (b), and 1415 (c) cm^{-1} represented the stretching vibrations of carboxyl groups of the adsorbed organic molecules. The bands at 1234-1036 (a), 1020 (b), and 1022 (c) cm^{-1} were attributed to the aryl-oxygen stretching vibrations of the molecules. The broad bands at 501 (a), 504 (b), and 517 (c) cm^{-1} were related to the characteristic absorptions of MnO_2. The results of FTIR investigation, coupled with the results of the deposition yield measurements, indicated the adsorption of the organic molecules on the surfaces of MnO_2 nanoparticles.

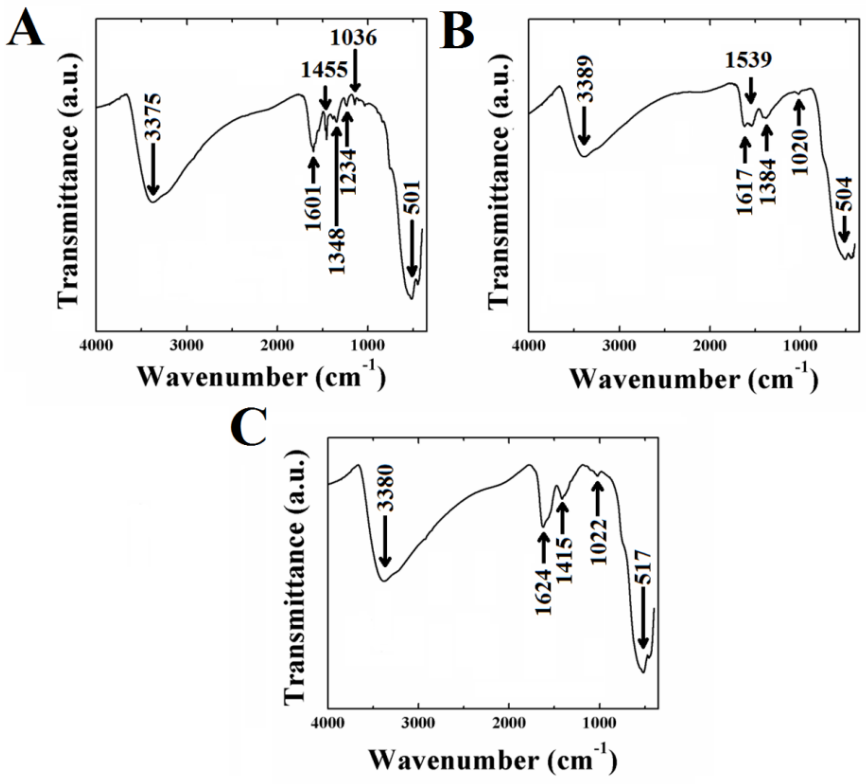

Figure 5-12 FTIR spectra for deposits prepared from 10 g L^{-1} MnO_2 suspensions containing 0.5 g L^{-1} of (A) SCA, (B) DHB, and (C) THBA.

5.1.2.5 SEM studies

SEM investigations of as prepared powders showed that some primary nanoparticles formed agglomerates, which were also observed in the deposited films (Figure 5-13A). Figure 5-13 B indicates that more uniform distribution of MnO_2 particles with reduced particle agglomeration can be achieved adding THBA as dispersant into solution for powder fabrication. The films prepared using THBA as a dispersing agent for precipitation and EPD were crack-free and porous (Figure 5-13B). The porosity can be attributed to packing of MnO_2 particles and gas evolution during deposition.

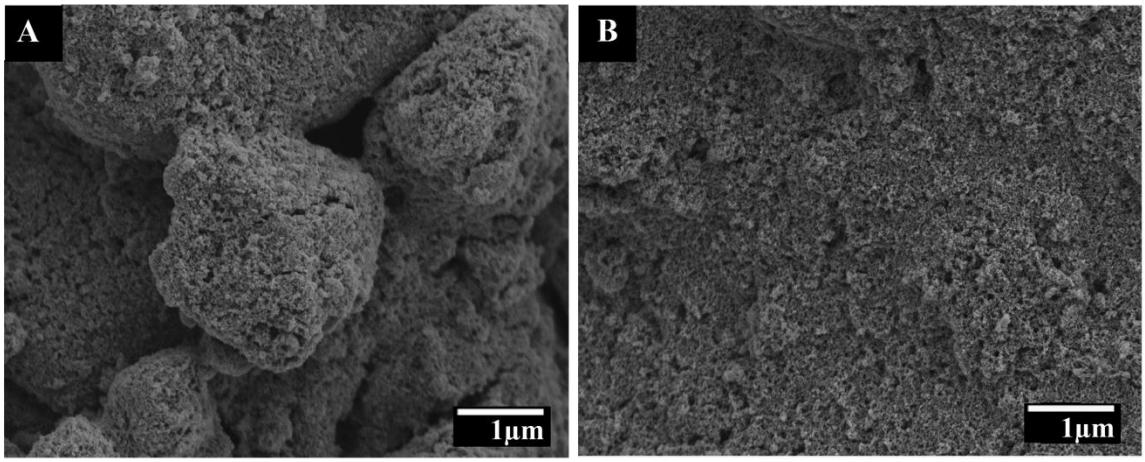

Figure 5-13 SEM images of the film prepared using THBA; (A) agglomerated film and (B) reduced agglomerated film with same magnification.

5.1.2.6 TGA & DTA studies of MnO_2/MWCNTs using THBA composite films

The films were studied by TGA and DTA. The TGA of pure MnO_2 (Figure 5-14a) showed mass loss, which could be attributed to the dehydration. The total mass loss at

800 ^{o}C was found to be 15 wt.%. Weight gain of 0.95 wt.% was recorded in the range of 440-500 ^{o}C and a corresponding DTA (Figure 5-15a) curve showed small exotherm, which could be attributed to the oxidation. It is suggested that as prepared powders contained a small amount of Mn^{3+} oxide which was oxidized to form Mn^{4+} oxide.

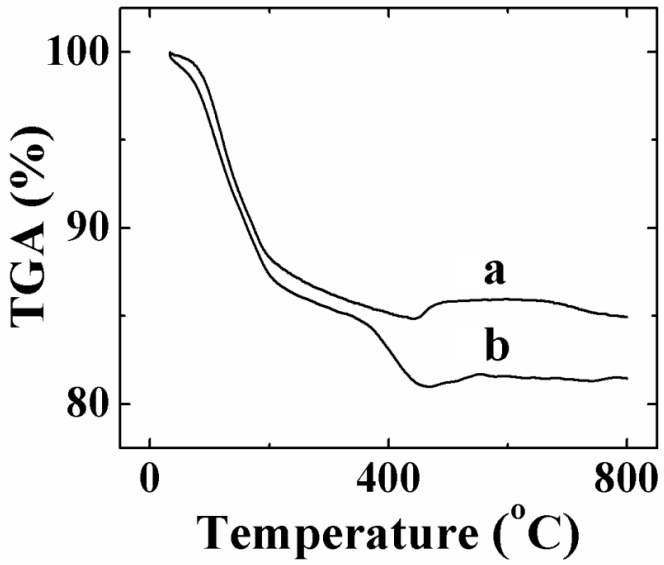

Figure 5-14 TGA data of (a) pure MnO_2 nanoparticles and (b) deposit prepared from 10 g L^{-1} MnO_2, 2 g L^{-1} CNTs and 0.5 g L^{-1} THBA aqueous solution.

Figure 5-14b shows the TGA data of MnO_2/MWCNTs deposit, prepared from suspensions, containing 10 g L^{-1} MnO_2, 2 g L^{-1} MWCNTs and 0.5 g L^{-1} THBA. The TGA data of MnO_2/MWCNTs (Figure 5-14b) showed a sharp reduction in sample weight below 200 ^{o}C, then sample weight decreased gradually with increasing temperature. Weight loss of 18 wt.% observed at 425 ^{o}C can be related to burning out of MWCNTs. The difference in total mass loss (Figure 5-14a, b) indicated the co-deposition of MnO_2

and MWCNTs. Weight gain of 0.65 wt.% observed in the range of 465-560 ^{o}C could be attributed to oxidation. The total weight loss at 800 ^{o}C was found to be 18.6 wt.%. The corresponding TGA data showed a broad exothermic peak, centered at 800 ^{o}C, which confirmed that the deposit contained MWCNTs. It should be noted that burning out of MWCNTs can be influenced by MnO_2 matrix, which limited the oxygen transfer and removal of oxidation products. This can explain the broad exothermic effect, extended to relatively high temperatures (Figure 5-15).

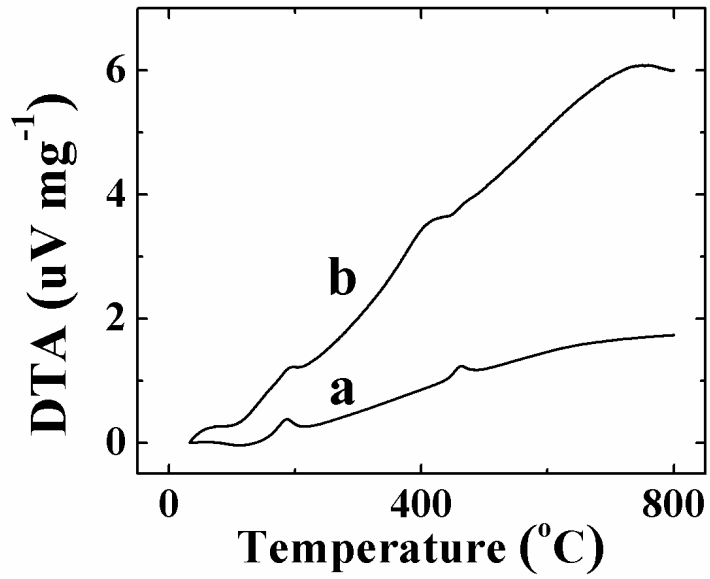

Figure 5-15 DTA data of (a) pure MnO_2 nanoparticles and (b) deposit prepared from 10 g L^{-1} MnO_2, 2 g L^{-1} CNTs and 0.5 g L^{-1} THBA aqueous solution.

5.1.3 Electrodeposition of MnO_2 with aurintricarboxylic acid

Figure 5-16 (a) shows that the chemical structure of aurintricarboxylic acid (ATA) includes three aromatic groups, OH groups and carboxylic groups bonded to the aromatic rings. ATA was dissolved in ethanol and used as a dispersing and charging agent for EPD of MnO_2.

The adsorption mechanism of ATA in MnO_2 suspension is shown in Figure 5-16b.

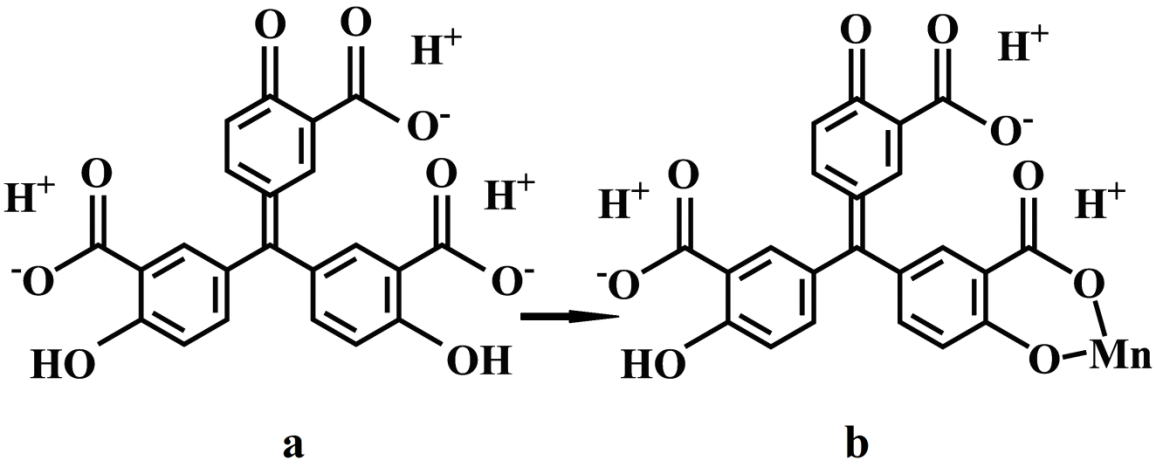

Figure 5-16 (a) Structure of aurintricarboxlic acid (ATA), (b) adsorption of ATA on the surface of MnO_2

5.1.3.1 Deposition yield study of MnO_2 films prepared using ATA

Figure 5-17 shows deposit mass versus ATA concentration in the MnO_2 suspensions. The adsorption of ATA on the surface of the MnO_2 particles resulted in electrosteric stabilization. Sedimentation experiments showed stability of the suspention during 3-4

days. Anodic deposits were obtained at ATA concentrations above 0.025 g L^{-1} ATA. The deposition yield increased significantly with increasing ATA concentration in the range from 0.025 to 0.285 g L^{-1} and slightly decreased at higher concentrations. The deposit mass increased with increasing deposition time (Figure 5-18). Therefore, the amount of the material deposited anodically can be varied.

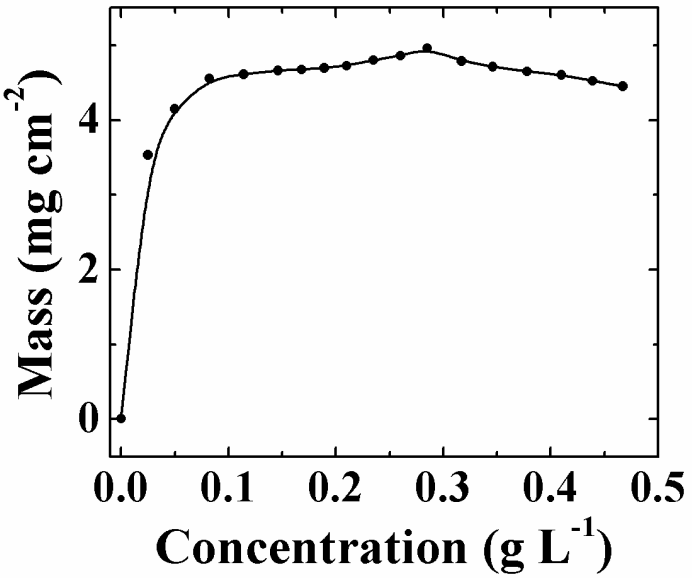

Figure 5-17 Deposit mass versus ATA concentration in 10 g L^{-1} MnO_2 suspension at a deposition voltage of 20 V and a deposition time of 5 min

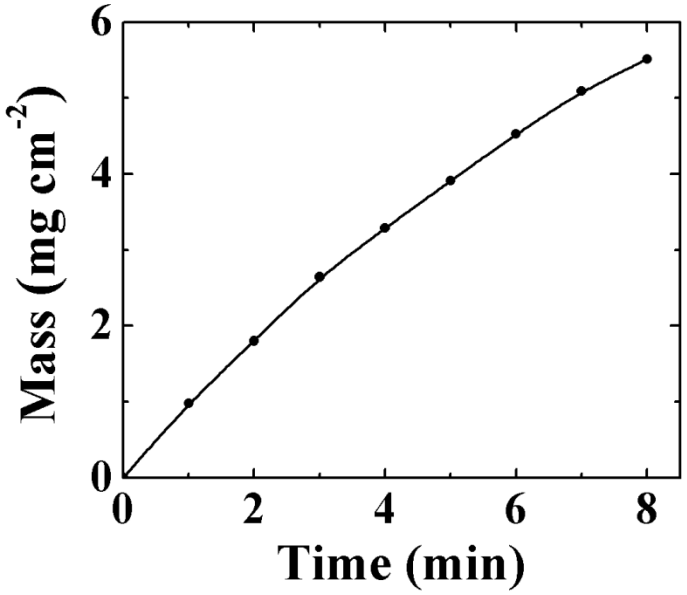

Figure 5-18 Deposit mass versus deposition time for 10 g L^{-1} MnO_2 suspension, containing 0.5 g L^{-1} ATA at a deposition voltage of 20 V.

5.1.3.2 FTIR study of MnO_2 films deposited using ATA

The films prepared by EPD were investigated by FTIR method. The FTIR spectra (Figure 5-19) showed broad peaks centered at 3394 cm^{-1} which were related to the stretching vibrations of OH group of adsorbed water molecules. The bands at 1615 - 1569 cm^{-1} were attributed C-C vibrations of adsorbed ATA. The bands at 1426 - 1311 cm^{-1} represented the stretching vibrations of carboxyl groups of the adsorbed organic molecules. The bands at 1032 - 911 cm^{-1} were attributed to the aryl-oxygen stretching vibrations of the molecules. The broad bands at 513 cm^{-1} were related to the characteristic absorptions of

MnO_2. The results of FTIR investigation, coupled with the results of the deposition yield measurements, indicated the adsorption of the organic molecules on the surfaces of MnO_2 nanoparticles.

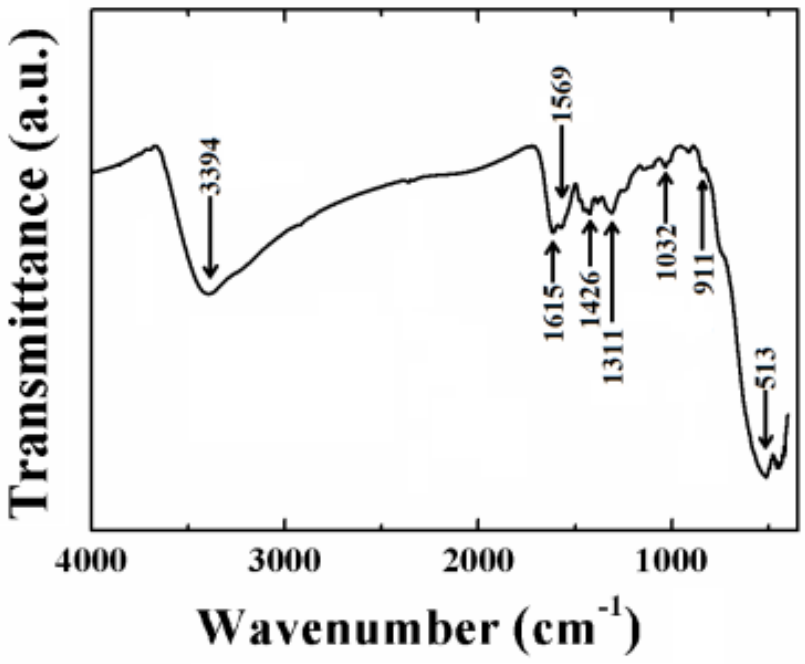

Figure 5-19 Fourier-transform infrared sectra of a deposit prepared from the 10 g L^{-1} MnO_2 suspension containin 0.5 g L^{-1} ATA

5.1.3.3 SEM study of MnO_2 film deposited using ATA

Figure 5-20 shows a typical SEM image of the films deposited by anodic deposition. The deposition resulted in the formation of dense and uniform films. SEM studies showed that film thickness could be varried in the range of 0-5 μm by adjusting deposition voltage

(from 5 to 15 V) and deposition time (0 – 10 min). The increase in the film thickness with increasing voltage was attributed to increasing electric field in the suspension.

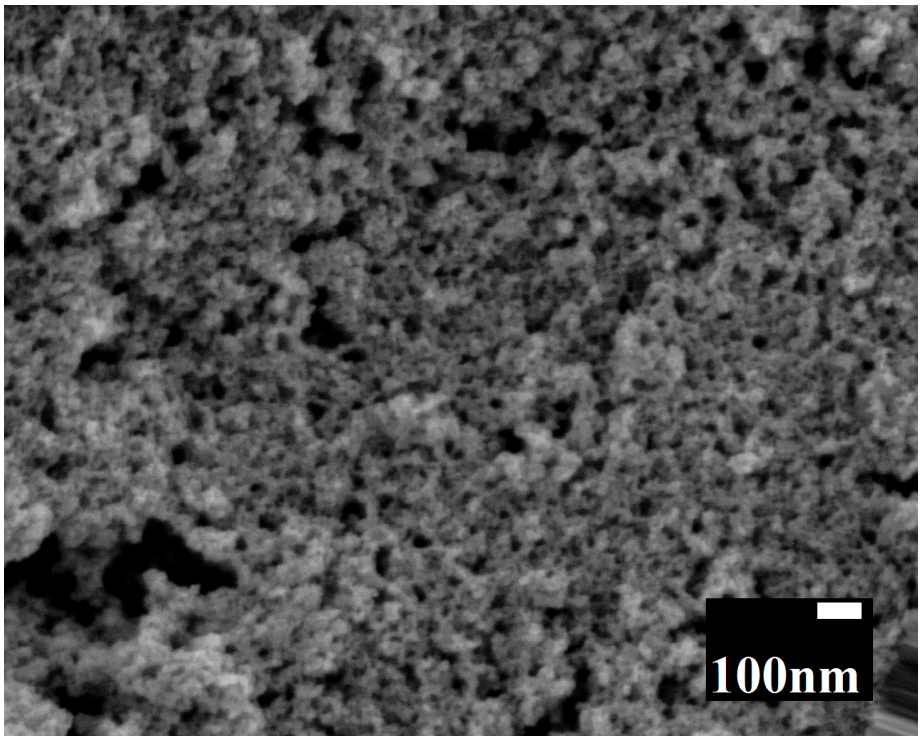

Figure 5-20 SEM image of MnO_2 film prepared from 10 g L^{-1} MnO_2 suspension, containing 0.5 g L^{-1} ATA in ethanol at a deposition voltage of 20 V and deposition time of 2 min

5.2 Electrodeposition of ATA

The chemical structure of aurintricarboxylic acid ammonium salt (aluminon) (Figure 5-21) includes three aromatic groups, OH groups and carboxylic groups bonded to the

aromatic rings. The carboxylic groups of aluminon (Figure 5-21) can provide a charge required for efficient dispersion and EPD.

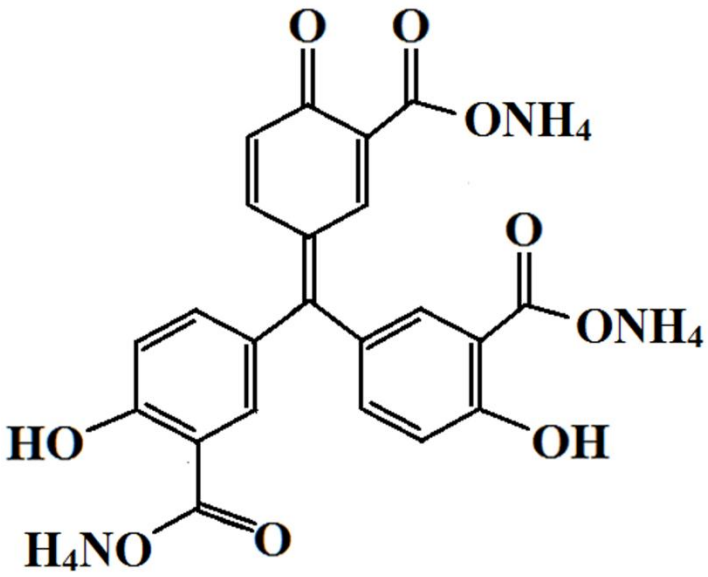

Figure 5-21 Chemical structure of aluminon

The application of aluminon as a charging and dispersing additive for EPD requires the investigation of electrochemical behaviour of this material. A thin red film was formed at the stainless steel working electrode at a potential of ~1 V. According to Y. Sun et al.[125] the current decreased with increasing cycle number during potentiodynamic cyling of electrode in aluminon solutions. Such decrease can be attributed to film growth at the potentiodynamic conditions. It is suggested that the increase in film thickness resulted in increasing film resistance. As a result, the current decreased with increasing cycle number.

It is suggested that the dissociation of aluminon (Figure 5-21) resulted in the formation of anionic species, containing $COOH^-$ groups, which migrated towards the anode. The electrochemical reaction of decomposition of water

$$2H_2O \rightarrow O_2 + 4H^+ + 4e^- \quad (5\text{-}1)$$

resulted in H^+ generation and a pH decrease at the anode surface. Therefore, the formation of ATA films can be expected as a result of the charge compensation and protonation of $COOH^-$ groups at the anode surface. It should be noted that ATA is insoluble in water. Therefore, the charge compensation and formation of ATA promoted film formation.

5.2.1 QCM study of ATA deposition

The results of potentiodynamic investigations are in good agreement with the constant voltage deposition data. Figure 5-22 shows deposition yield measured using QCM as a function of deposition time. The deposit mass increased with increasing time, indicating the formation of films of different mass. Therefore, the amount of the deposited material can be varied.

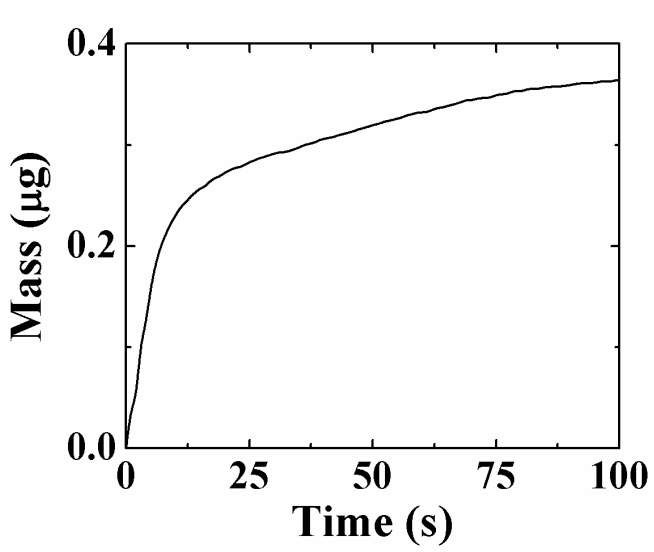

Figure 5-22 Deposition yield measured using QCM for 0.2 g L^{-1} aluminon solution at deposition voltage of 5 V

5.2.2 AFM study of ATA films

Figure 5-23 shows an AFM image of a film prepared from 1 g L^{-1} aluminon solution at a deposition voltage of 10 V. The root mean-square surface roughness was found to be 3.5 nm. The surface roughness of the films can be attributed to the gas evolution at the cathode surface during electrodeposition.

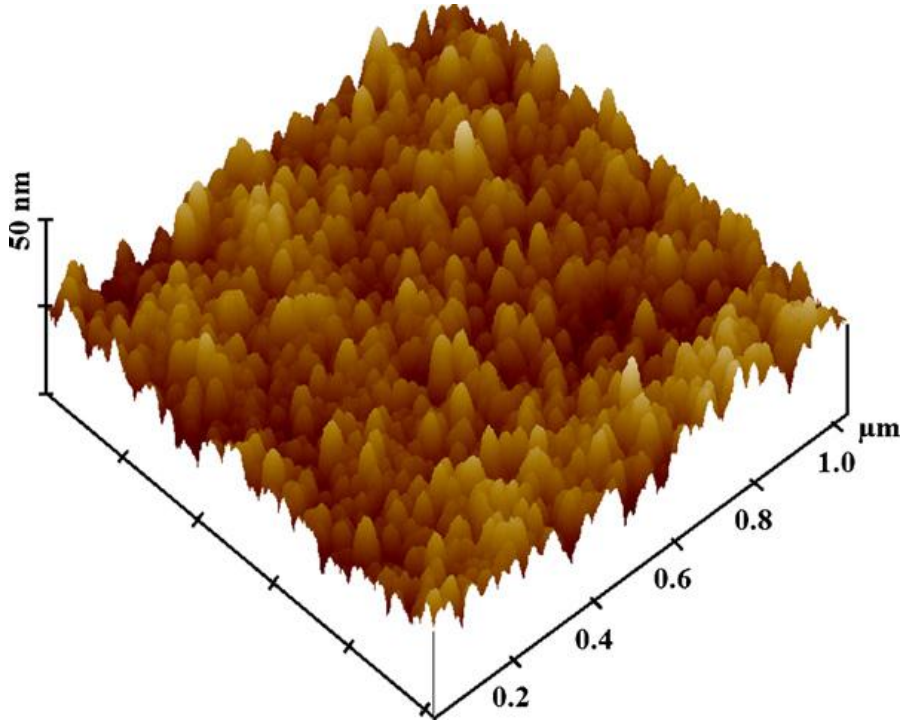

Figure 5-23 AFM image of a film prepared from 1 g L^{-1} aluminon solution at adeposition voltage of 10 V

5.2.3 Electrodeposition of aurintricarboxylic acid with graphene and MWCNTs

The conjugated bonds formed by carbon atoms of aurintricarboxylic acid make this material attractive for the dispersion of carbon nanotubes and graphene. It is known that aromatic compounds with conjugated bonds interact strongly with sidewalls of carbon nanotubes and graphene through π - π stacking[126-128]. It was shown[126] that the adsorption affinity of the phenolic molecules to carbon nanotubes increased with the increasing number of aromatic rings and OH groups bonded to the aromatic rings. It is in this regard

that 1-naphthol and pyrogallol showed better adsorption on CNT compared to phenol[126]. The carboxylic groups of aluminon (Figure 5-21) can provide a charge required for efficient dispersion and EPD.

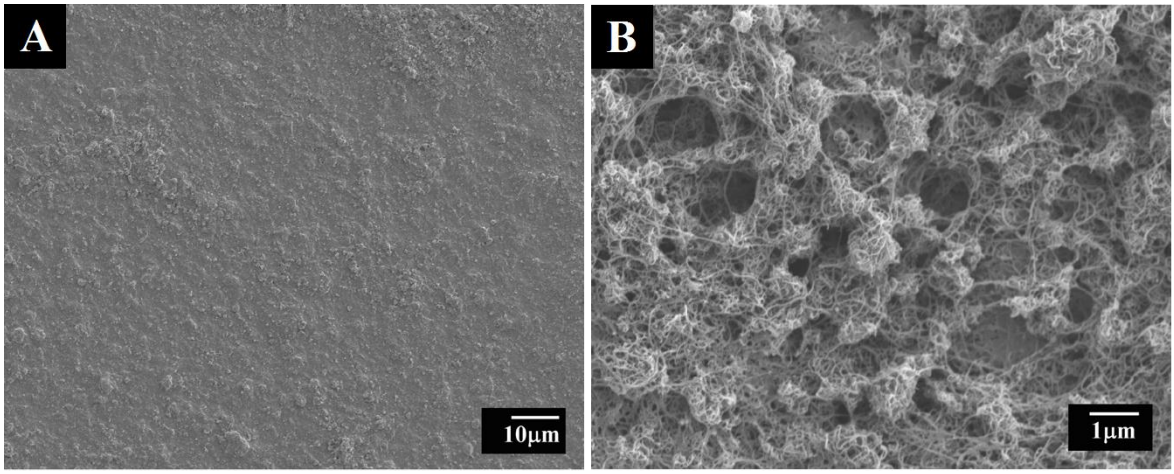

Figure 5-24 SEM images at different magnifications of a deposit obtained from 1 g L^{-1} aluminon solution, containing 0.5 g L^{-1} MWCNTs at a deposition voltage of 7 V.

It was found that aluminon allows efficient dispersion of carbon nanotubes and graphene. Sedimentation experiments showed that carbon nanotube and graphene suspensions were stable at least 7 days. The adsorption of aluminon on carbon nanotubes and graphene allowed efficient dispersion and provided a negative charge for EPD. It is suggested that adsorption was attributed to π - π stacking mechanism. Figures 5-24 and 25 show SEM images of the surfaces of the deposits at different magnifications. The low magnification images indicated that the films were continuous and crack-free. The high magnification images showed that the films contained carbon nanotubes (Figure 5-24B) and graphene (Figure 5-25B) and exhibited porosity. The charge neutralization of aluminon and the

formation of insoluble aurintricarboxylic acid at the electrode surface allowed the deposition of carbon nanotubes and graphene. Moreover, good film forming properties of aurintricarboxylic acid promoted deposit formation.

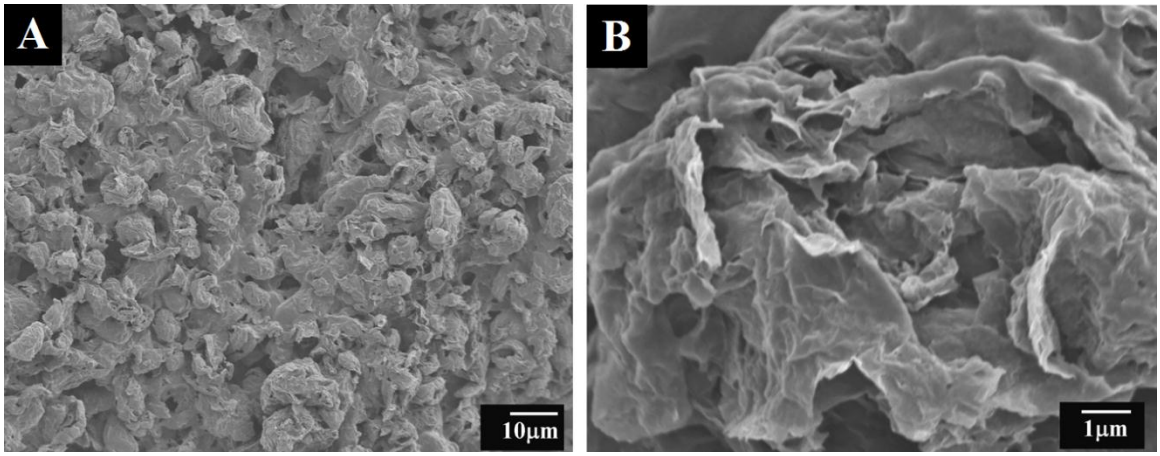

Figure 5-25 SEM images at different magnifications of a deposit obtained from 1 g L^{-1} aluminon solution, containing 0.5 g L^{-1} graphene at a deposition voltage of 7 V.

5.3 Studies of MnO_2/MWCNTs composites

Conductive additives, such as carbon black, are usually added to manganese dioxide in order to increase the electronic conductivity of the composite electrodes and improve power-energy characteristics of ES[60]. However, the SC of carbon additives is low; therefore the carbon additive content in the composite materials must be optimized. The use of carbon nanotubes as conductive additives has benefits of high surface area and low percolation threshold[129]. Therefore, the formation of composite electrodes containing manganese dioxide and carbon nanotubes offers an advantage of improved contact

between two different materials, lower binder and carbon content, which can result in improved electrochemical properties of the composite electrodes.

In this work MnO_2/MWCNTs composite electrodes were prepared using DHB, THBA and ATA as dispersing agents and different types of current collectors, such as nickel foams, stainless steels and nickel plaques.

5.3.1 Nickel foam based composite electrodes

Porous nickel foams are in high demand for applications in nickel–cadmium[112, 113], nickel–zinc[130], lithium ion[131] batteries and electrochemical supercapacitors (ESs)[132]. In the batteries and supercapacitors, nickel foams are used as high surface area current collectors, containing highly accessible active material within their conducting light weight web, which provides structural strength[133].

Electrodes are produced by pasting a slurry of active material into a porous nickel foam, followed by impregnation, drying and calendering (Figure 4-3). The high porosity and large pore size of nickel foams allow for easy impregnation of the active material slurry into the porous current collectors. However, the increase in foam porosity resulted in reduced conductivity[112]. This problem has been addressed by the use of conductive additives, which formed a secondary conductivity network[112] within the nickel foam cells. The addition of nickel filaments[112] or carbon nanotubes[134] to the active material enabled enhanced conductivity for high power applications. The use of nickel foam current

collectors for batteries allowed the fabrication of advanced electrodes[112, 113] with lower internal resistance, better electrolyte access to active material and improved electrochemical performance.

The slurry, containing 0.615 g L^{-1} MWCNTs, 0.062 g L^{-1} ATA and 0.062 g L^{-1} PVB was added to 2.4 g $KMnO_4$ aqueous solution reduced with ethanol. Mixed suspension was stirred for 20 h. The total mass of manganese dioxide and MWCNT in the composite electrodes was 38 and 40 mg cm^{-2}. The impregnated INCOFOAM® was roller pressed to ~20% of initial thickness in order to achieve final porosity of 30%[112]. Cyclic voltammetry (CV) studies were performed within a potential range of 0–0.9 V vs SCE at scan rates of 2–100 mV s^{-1}. The SC was calculated using Eq. 4-2.

5.3.1.1 Capacitive behaviour studies of composite electrode

Electrochemical testing in the 0.5 M Na_2SO_4 solutions revealed capacitive behaviour of the composite electrode. Figure 5-26A and Figure 5-26B show typical CVs at different scan rates for the composite electrode with material loading of 38 and 40 mg cm^{-2}, respectively. Within potential range of 0-0.9 V versus SCE the composite electrode showed capacitive like current-potential responses, indicated by the box shape of the CVs.

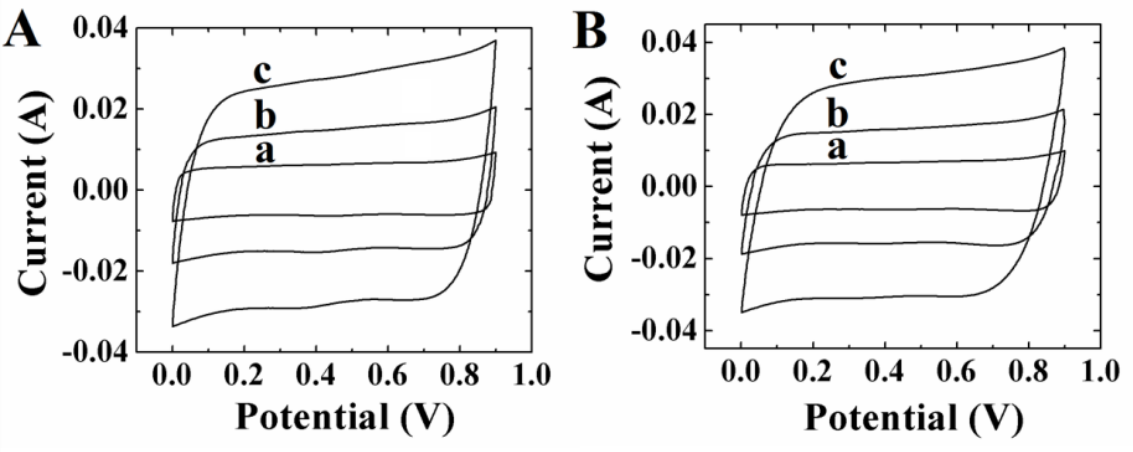

Figure 5-26 CV of as prepared (A) 40 mg cm^{-2} and (B) 38 mg cm^{-2} film deposited on nickel foam from MnO_2/MWCNTs containing ATA and PVB solution at the scan rate of (a) 2 mV s^{-1}, (b) 5 mV s^{-1}, and (c) 10 mV s^{-1}.

The composite electrodes, containing 38 and 40 mg cm^{-2}, showed SC value of 84 and 77 F g^{-1}, respectively, at a scan rate of 2 mV s^{-1}. It is important note that the increasing thickness of composite electrode induced low SC value (Figure 5-27). The SC value decreased significantly at higher scan rates to 12.5 and 17.6 F g^{-1}, respectively. The reduction in the SC value is especially evident at a scan rate of 100 mV s^{-1}.

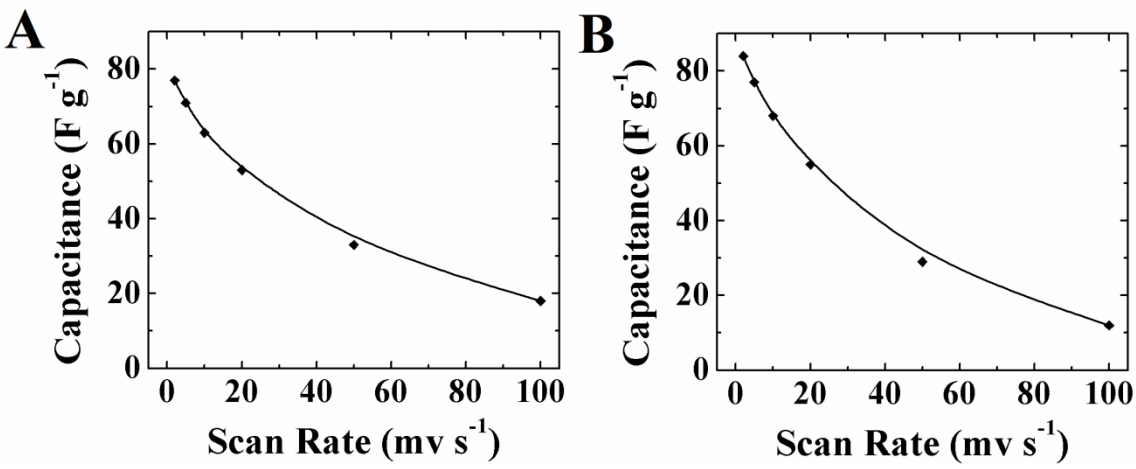

Figure 5-27 SC versus scan rate for composite electrodes containing (A) 40 and (B) 38 mg cm^{-2} MnO_2/MWCNTs tested in 0.5 M Na_2SO_4 solutions.

5.3.1.2 Impedance spectroscopy

Figure 5-28 shows complex impedance of the electrode in the frequency range of 100 mHz to 100 kHz. The equivalent circuit for electrochemical supercapacitors was discussed in detail by Conway[1]. The high frequency value of the real part of complex impedance has been used for the estimation of equivalent series resistance which was found to be ~ 0.92 and 1.4 Ω cm^2, for the electrodes with material loadings of 40 and 38 mg cm^{-2}, respectively. It is suggested that the further optimization of electrode composition and microstructure will result in reduced resistance and improved capacitive behaviour.

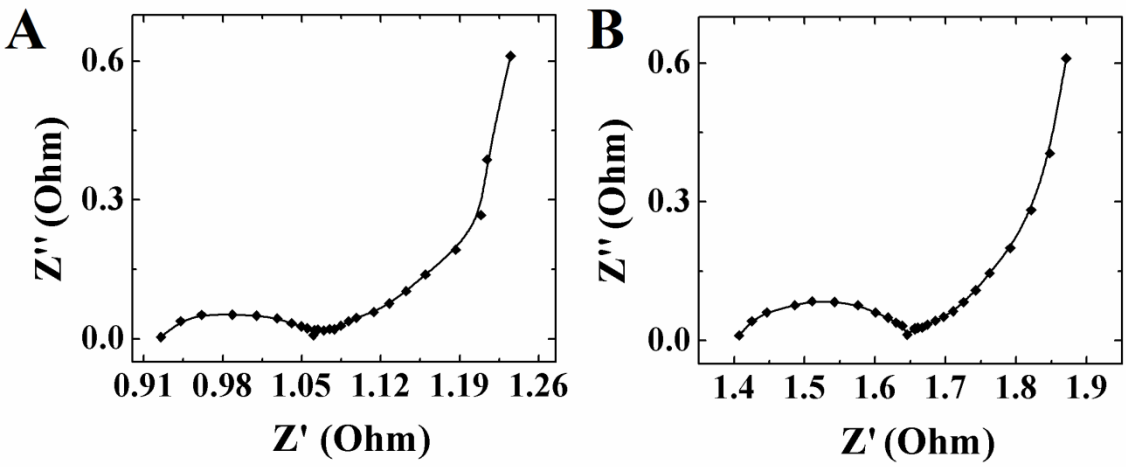

Figure 5-28 Impedance data with Z´ as the real part Z´´ as the imaginary part of the (A) 40 mg cm^{-2} and (B) 38 mg cm^{-2} films prepared on nickel foam from MnO_2/MWCNTs containing ATA and PVB solution.

5.3.2 Nickel plaque based composite electrodes

Another type of nickel material is nickel plaque, also widely used in industry for the fabrication of electrodes for rechargeable batteries[135]. Nickel plaques are designed for high power applications. Active materials are impregnated chemically or electrochemically into the porous nickel structures, which are used as current collectors[136]. Nickel plaques are current collectors of choice for battery applications demanding high power and reliability, along with long cycle life, such as batteries for aerospace and railway applications, power tools, and some portable electronics[135]. The pore size of nickel plaques is smaller compared to that of foams. The smaller pore size

decreases the distance for electrons to travel from the current collector into the active material during cell discharge, and consequently improves the discharge rate characteristics for high power applications[136].

The SEM image (Figure 5-29A) shows small particle size of nickel plaque in the range of 0.5-2 µm, which forms a conductive porous matrix. It was suggested that high surface area, small particle size, porosity and conductivity of nickel plaques are beneficial for application in ESs. The SEM image of the impregnated material shows porous microstructure of MnO_2/MWCNT composite (Figure 5-29B). The arrows (Figure 5-29B) indicated MWCNTs.

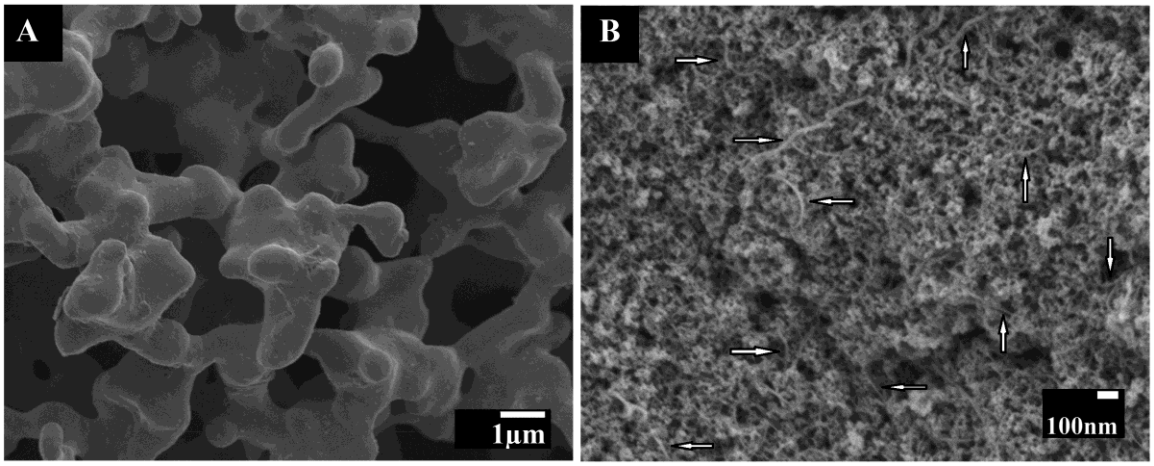

Figure 5-29 SEM images of Nickel plaque; (A) before impregnation and (B) Nickel plaque impregnated using 10 g L^{-1} MnO_2, 2 g L^{-1} CNTs and 0.5 g L^{-1} THB suspension at 7 V and 2 min, material loading of 2.18 mg cm^{-2}.

5.3.2.1 Effect of active material composition

Figure 5-30 shows the influence of active material composition on the capacitive behaviour of the electrodes. For manganese dioxide electrodes, the relatively small area of the CV indicated poor capacitive behaviour. The composite electrodes containing MWCNTs showed box shape CVs (Figure 5-30). The electrodes, containing 10 g L^{-1} MnO_2 mixed with 1 and 2 g L^{-1} MWCNTs, showed SC value of 132 and 140 F g^{-1}, for film mass 1.27 and 1.78 mg cm^{-2}, respectively, at a scan rate of 2 mV s^{-1}.

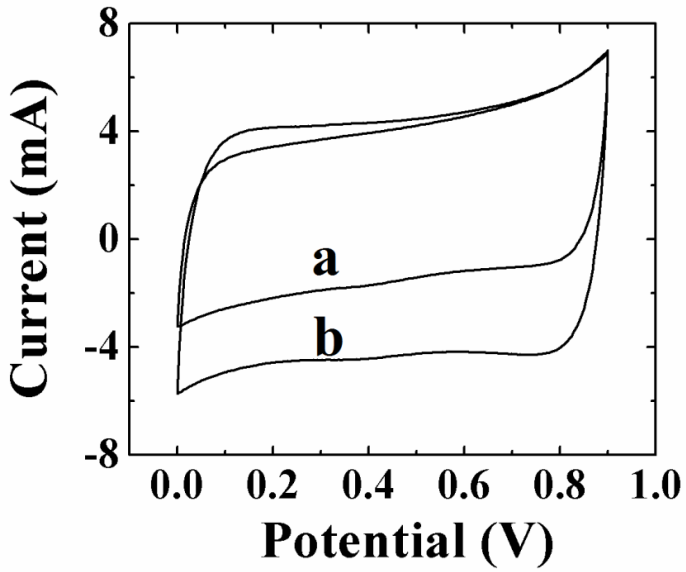

Figure 5-30 CVs at a scan rate of 20 mV s^{-1} for composite electrodes, prepared using suspensions, containing 10 g L^{-1} MnO_2, (a) 1 g L^{-1}, (b) 2 g L^{-1} MWCNTs, and 0.5 g L^{-1} THBA, tested in the 0.5 M Na_2SO_4.

The increase in MWCNTs content from 1 to 2 g L^{-1} resulted in increase in SC from 109 to 120 F g^{-1} at a scan rate of 20 mV s^{-1} and from 98 to 104 F g^{-1} at a scan rate of 50 mV s^{-1}

(Figure 5-31). The increase in SC can be attributed to increasing conductivity of the composite materials and changes in the composite microstructure associated with increasing MWCNTs content from 1 to 2 g L^{-1}. Recent studies showed that MWCNTs can reduce the aggregation of nanoparticles of active material, inducing better distribution of the particles in the netlike MWCNTs structure[137]. Reduced agglomeration of the particles resulted in improved electrochemical performance of the composite electrodes.

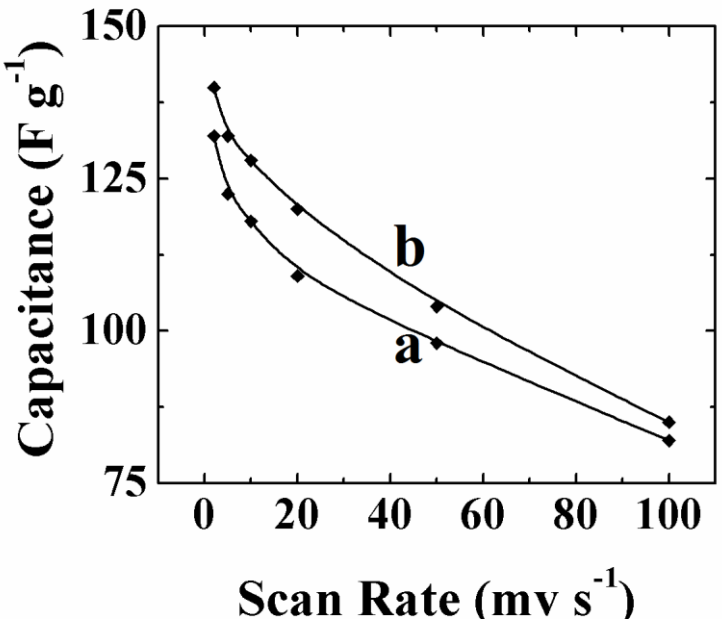

Figure 5-31 SC versus scan rate for composite electrodes, prepared from suspensions, containing 10 g L^{-1} MnO_2 (a) 1 g L^{-1}, (b) 2 g L^{-1} MWCNTs, and 0.5 g L^{-1} THBA, tested in the 0.5 M Na_2SO_4.

5.3.2.1.1 Impedance spectroscopy

Figure 5-32 shows complex impedance of the electrodes in the frequency range from 100 mHz to 100 kHz. The high frequency value of the real part of complex impedance has been used for the estimation of equivalent series resistance, which was found to be ~ 2 and 1.4 Ω cm^2, for the sample prepared from 10 g L^{-1} MnO_2 slurries, containing 1 and 2 g L^{-1} MWCNTs, respectively. It is suggested that the further optimization of electrode composition and microstructure will result in reduced resistance and improved capacitive behaviour.

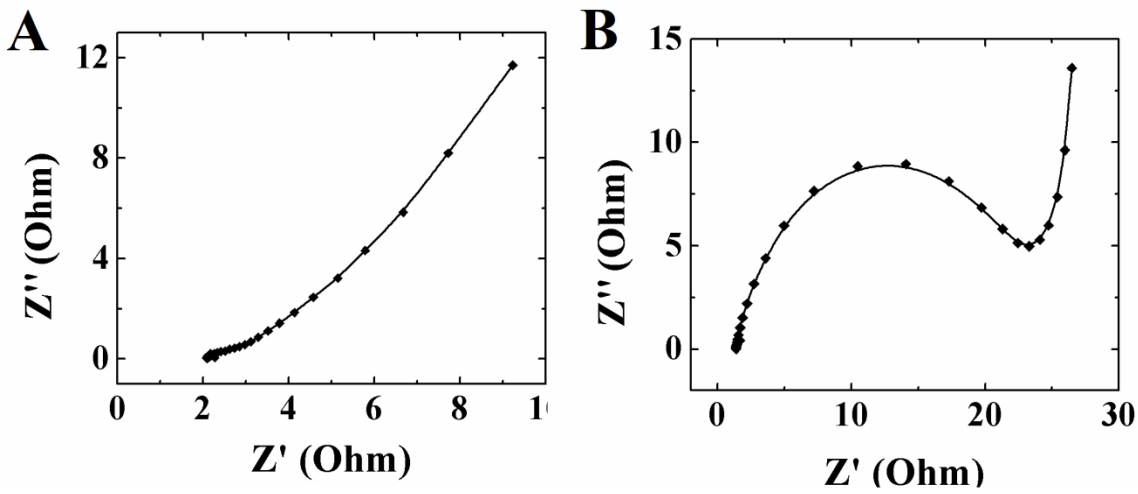

Figure 5-32 Impedance data with Z´ as the real part Z´´ as the imaginary part for the nickel plaque based electrodes prepared from 10 g $L^{-1}$$MnO_2$ and (A) 1 g L^{-1} and (B) 2 g L^{-1} CNTs suspensions, containing 0.5 g L^{-1} THBA.

5.3.3 Stainless steel based composite electrodes

The capacitive behaviour of the films prepared by EPD was investigated in the potential range of 0-0.9 V versus SCE. Figure 5-33 shows typical CVs of MnO_2/MWCNTs electrodes, prepared using DHB and THBA and tested in the 0.5 M Na_2SO_4 solutions at scan rate of 20 mV s^{-1} in the potential range of 0-0.9 V versus SCE.

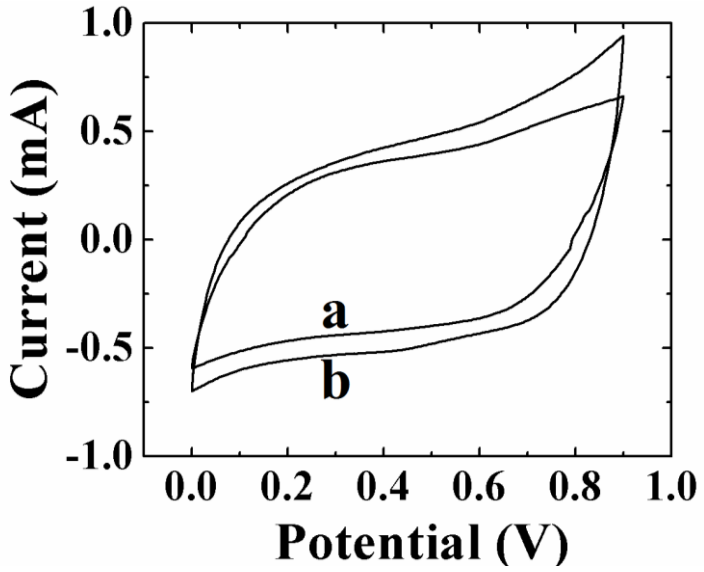

Figure 5-33 CVs at a scan rate of 20 mV s^{-1} for composite electrodes, prepared from suspensions, containing 10 g L^{-1} MnO_2, 0.1 g L^{-1}MWCNTs and (a) 0.3 g L^{-1} DHB, (b) 0.2 g L^{-1} THBA, tested in the 0.5 M Na_2SO_4.

The SC value of the obtained films was calculated from the CV curves using Equation 4-2. The results presented in Figure 5-34 indicated that the SC value measured at a scan rate of 2 mV s^{-1} for MnO_2/MWCNT composites prepared using DHB and THBA was 264 and 268 F g^{-1}, respectively. The decrease in SC value with increasing scan rate could be

attributed to low electronic and ionic conductivity of manganese dioxide. THBA dispersing agent allowed better capacitive performance than DHB for composite films prepared from 10 g L^{-1} MnO_2 and 0.1 g L^{-1} MWCNTs suspensions.

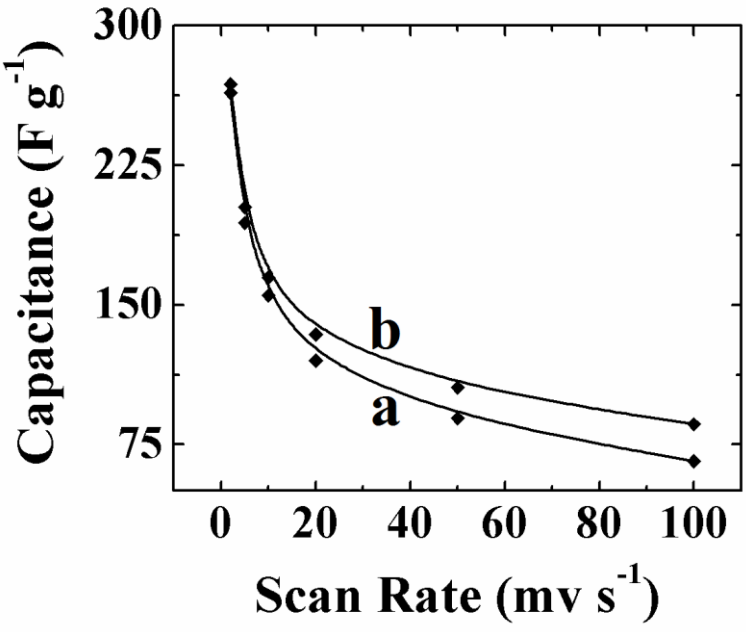

Figure 5-34 SC value versus scan rate for composite electrodes prepared from slurries containing 10 g L^{-1} MnO_2, 0.1 g L^{-1} MWCNTs and (a) 0.3 g L^{-1} DHB and (b) 0.2 g L^{-1} THBA, tested in the 0.5 M Na_2SO_4.

5.3.3.1 Impedance Spectroscopy

Figure 5-35 shows complex impedance of the electrode in the frequency range from 100 mHz to 100 kHz. The equivalent circuit for electrochemical supercapacitors was discussed in detail by Conway. The high frequency value of the real part of complex

impedance has been used for the estimation of equivalent series resistance which was found to be ~ 6.45 and 3.98 Ω cm^2, for films prepared from slurries containing 10 g L^{-1} MnO_2, 0.1 g L^{-1} MWCNTs and for mass loading 0.156 and 0.135 mg cm^{-2}, respectively. It is suggested that the further optimization of electrode composition and microstructure will result in reduced resistance and improved capacitive behaviour.

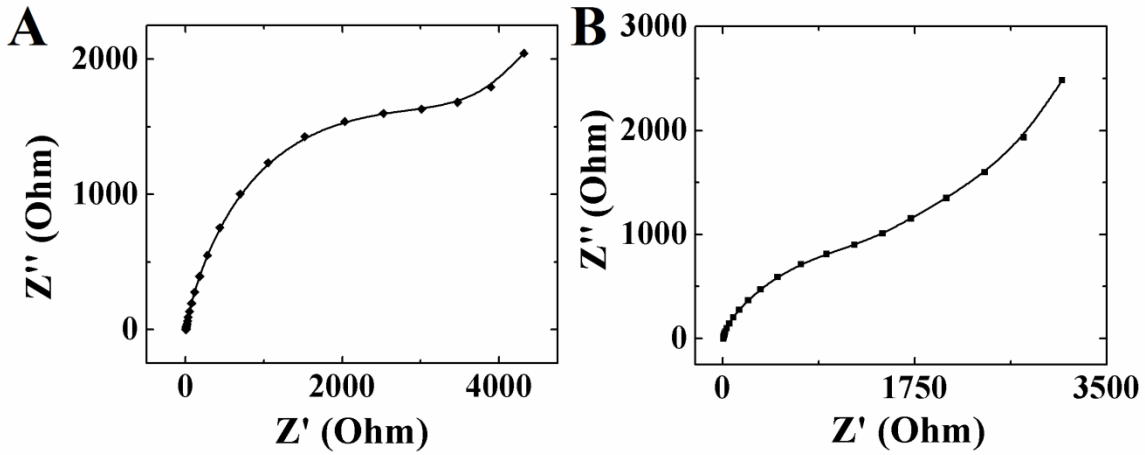

Figure 5-35 Impedance data with Z´ as the real part Z´´ as the imaginary part for the deposit obtained on stainless steel films from 10 g $L^{-1}MnO_2$, 0.1 g L^{-1} MWCNTs, and (A) 0.3 g L^{-1} DHB ad (B) 0.2 g L^{-1} THBA solution.

5.3.4 Comparison of capacitive behaviour of electrodes prepared using stainless steel and nickel plaque current collectors

The capacitive behaviour of the electrodes prepared using different collectors was studied in 0.5 M Na_2SO_4 solutions. Figure 5-36 A shows typical CVs of nickel plaque and

stainless steel obtained at scan rates of 5 mV s^{-1}. The box shape of the CVs indicated capacitive properties of the coatings in the voltage window of 0–0.9 V. The increase in material loading resulted in increased area of the CVs, which was related to increased capacitance of the electrodes. The nickel plaque's samples showed larger CV areas, which indicated high capacitance.

The SC value of the electrodes was calculated from the CV data using Eq. (4-2). The comparison of the capacitive behaviour of the electrodes prepared using EPD methods showed that nickel plaque based electrodes have higher SC value than stainless steel electrode (Figure 5-36 B). The highest SC was observed 182, 163 F g^{-1} from nickel plaque and stainless steel electrodes, for deposited mass of 2.08 and 0.650 mg cm^{-2}, respectively, at a scan rate of 2 mV s^{-1}. The SC decreased with increasing scan rate due to the electrolyte diffusion limitation in pores. The results of SC value measurements correlate with SEM observations of microstructures of impregnated plaques, which showed higher porosity of Ni plaque based electrodes.

The results of electrochemical impedance studies (Figure 5-36 C and D) are in good agreement with the SC measurements and SEM data. The detailed analysis of the behaviour of complex impedance $Z^* = Z' - iZ''$ using equivalent circuits for impregnated electrodes presents difficulties and can be a subject of separate theoretical and experimental study. However, the electrode of nickel plaque showed much lower Z´ in the whole frequency range studied, which indicated lower electrode resistance. On the

other hand, higher capacitance of the electrodes prepared by this method resulted in lower Z´´.

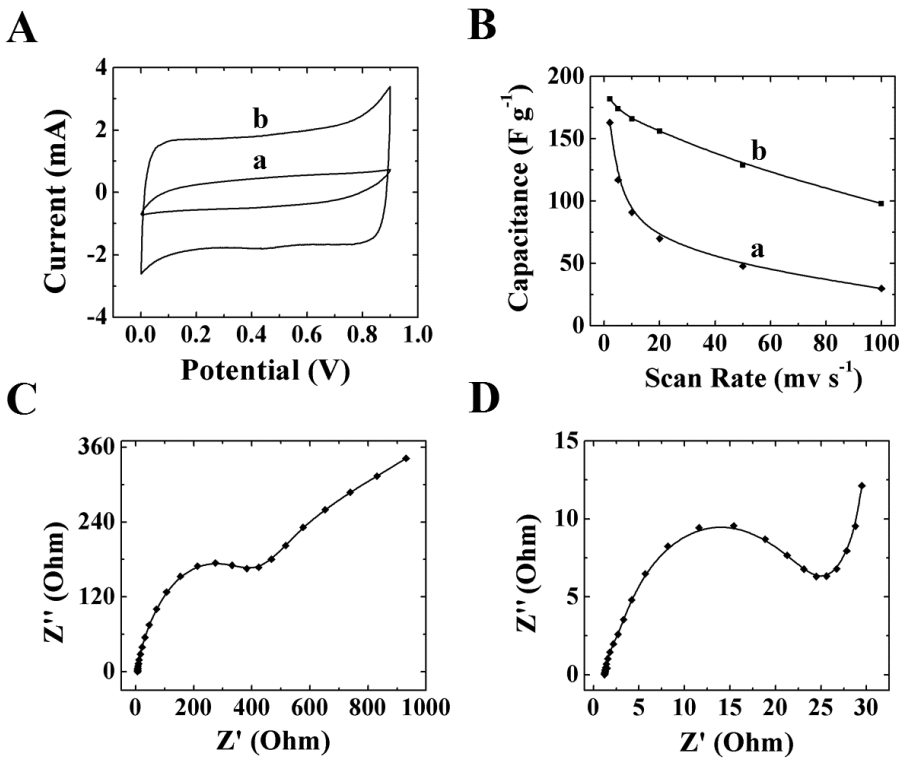

Figure 5-36 (A) CV curves at 5 mV s^{-1} scan rate for (a) stainless steel based electrode, (b) nickel plaque based electrode, (B) the comparison of capacitance of (a) stainless steel and (b) nickel plaque based electrodes, (C and D) impedance data for stainless steel and nickel based electrodes, respectively. The mass of the active material was 0.650 mg cm^{-2} for stainless steel and 2.08 mg cm^{-2} for nickel plaque based electrodes, prepared using 10 g L^{-1} MnO_2 suspensions containing 2 g L^{-1} CNTs and 0.5 g L^{-1} THBA and tested in 0.5 M Na_2SO_4 solution.

The results of this investigation showed that similar to the alkaline secondary cells, Ni plaques can be chemically and electrochemically impregnated with an active material for application in ESs.

Chapter 6 Conclusions

- The anodic EPD method has been developed for the fabrication of MnO_2 films. Benzoic acid and phenolic molecules, such as 3,4-dihydroxybenzoic acid, 3,4-dihydroxyphenylacetic, 3,4-dihydroxyhydrocinnamic acid, 3,4,5-trihydroxybenzoic acid, salicyclic acid, 2,3,4-trihydroxybenzoic acid, aurintricarboxylic acid and aurintricarboxylic acid ammonium salt were investigated as additives for the dispersion and charging of MnO_2 particles. The adsorption of the organic molecules on the oxide particles involved the interaction of COOH groups and OH groups with Mn atoms on the particle surfaces and complexation. The results of deposition yield studies and FTIR investigation showed that adjacent OH groups, as well as adjacent OH and COOH groups bonded to the aromatic ring of the phenolic molecules enabled enhanced adsorption of the molecules on oxide particles. 2,3,4-trihydroxybenzoic acid was shown to be an effective charging additive, which provided stabilization of MnO_2 particles in the suspensions and their deposition. Such organic molecules can be used for the dispersion and charging of oxide particles and for EPD of oxide films with advanced functional properties. Additionally, EPD of manganese dioxide and MWCNTs were achieved using 3,4-dihydroxybenzoic acid, 2,3,4-trihydroxybenzoic acid, and aurintricarboxylic acid as a common dispersant, charging additive and binder.

- Aurintricarboxylic acid ammonium salt (aluminon) provided a charge required for efficient dispersion and EPD. It was found that aluminon allows efficient dispersion of carbon nanotubes and graphene.
- Composite electrodes containing two different materials were fabricated by impregnation of slurries of manganese dioxide and MWCNTs into porous nickel foam and plaque current collectors. MWCNTs improved electrochemical performance of the electrodes by forming a secondary conductivity network within the porous nickel structures. The nickel foam based composite electrodes with total mass loading of 40 mg cm^{-2} showed good capacitive behaviour in the 0.5 M Na_2SO_4 solutions. The SC increased with increasing MWCNTs content in suspension in the range of 1 – 2 g L^{-1} and decreased with increasing scan rate. The highest SC of 140 F g^{-1} was obtained at a scan rate of 2 mV s^{-1} in the 0.5 M Na_2SO_4 solutions.
- The nickel plaque and stainless steel based composite electrodes with total mass loading of 2.08 and 0.650 mg cm^{-2} were compared and nickel plaque electrodes showed better capacitive behaviour in the 0.5 M Na_2SO_4 solutions. The highest SC of 182 F g^{-1} was obtained at a scan rate of 2 mV s^{-1} for materials loading of 2.08 mg cm^{-2}.

References

1. B.E. Conway, *Electrochemical Supercapacitors - Scientific Fundamentals and Technological Applications*1999, Kluwer, New York. p.

2. S. Sarangapani, B.V. Tilak, and C.P. Chen, *Materials for Electrochemical Capacitors.* Journal of The Electrochemical Society, 1996. **143**(11): p. 3791-3799.

3. J.P. Zheng and T.R. Jow, *A New Charge Storage Mechanism for Electrochemical Capacitors.* Journal of The Electrochemical Society, 1995. **142**(1): p. L6-L8.

4. S. Devaraj and N. Munichandraiah, *High Capacitance of Electrodeposited MnO_2 by the Effect of a Surface-Active Agent.* Electrochemical and Solid-State Letters, 2005. **8**(7): p. A373-A377.

5. M. Toupin, T. Brousse, and D. Bélanger, *Influence of Microstucture on the Charge Storage Properties of Chemically Synthesized Manganese Dioxide.* Chemistry of Materials, 2002. **14**(9): p. 3946-3952.

6. C. Ye, Z.M. Lin, and S.Z. Hui, *Electrochemical and Capacitance Properties of Rod-Shaped MnO_2 for Supercapacitor.* Journal of The Electrochemical Society, 2005. **152**(6): p. A1272-A1278.

7. R.N. Reddy and R.G. Reddy, *Sol–gel MnO_2 as an electrode material for electrochemical capacitors.* Journal of Power Sources, 2003. **124**(1): p. 330-337.

8. H.I. Becker, *Low voltage electrolytic capacitors*,U.S., Patent 2 800 616, 1957

9. R.A. Rightmire, *Electrical energy storage apparatus*,U.S., Patent 3 288 641, 1970

10. X. Andrieu, *Ultracapacitors for portable electronics*. Energy Storage Systems for Electronics: New Trends in Electrochemical Technology. **1**. 2000. p. 521

11. S. Hadzi-Jordanov, et al., *Reversibility and Growth Behavior of Surface Oxide Films at Ruthenium Electrodes.* Journal of The Electrochemical Society, 1978. **125**(9): p. 1471-1480.

12. S. Trasatti and G. Buzzanca, *Ruthenium dioxide: A new interesting electrode material. Solid state structure and electrochemical behaviour.* Journal of Electroanalytical Chemistry and Interfacial Electrochemistry, 1971. **29**(2): p. A1-A5.

13. P. Sharma and T.S. Bhatti, *A review on electrochemical double-layer capacitors.* Energy Conversion and Management, 2010. **51**(12): p. 2901-2912.

14. R. Kötz and M. Carlen, *Principles and applications of electrochemical capacitors.* Electrochimica Acta, 2000. **45**(15–16): p. 2483-2498.

15. A.K. Shukla, S. Sampath, and K. Vijayamohanan, *Electrochemical supercapacitors: Energy storage beyond batteries.* Current Science, 2000. **79**(12): p. 1656-1661.

16. J.C.E. Marin S. Halper, *Supercapacitors: A Brief Overview*. 2006.

17. P. Simon and Y. Gogotsi, *Materials for electrochemical capacitors.* Nat Mater, 2008. **7**(11): p. 845-854.

18. L.T. Lam and R. Louey, *Development of ultra-battery for hybrid-electric vehicle applications.* Journal of Power Sources, 2006. **158**(2): p. 1140-1148.

19. F.S. Garcia, A.A. Ferreira, and J.A. Pomilio. *Control Strategy for Battery-Ultracapacitor Hybrid Energy Storage System*. in *Applied Power Electronics Conference and Exposition, 2009. APEC 2009. Twenty-Fourth Annual IEEE*. 2009.

20. C. Peng, et al., *Carbon nanotube and conducting polymer composites for supercapacitors.* Progress in Natural Science, 2008. **18**(7): p. 777-788.

21. A.G. Pandolfo and A.F. Hollenkamp, *Carbon properties and their role in supercapacitors.* Journal of Power Sources, 2006. **157**(1): p. 11-27.

22. K.S.W. Sing, et al., *Reporting physisorption data for gas/solid systems with special reference to the determination of surface area and porosity (Recommendations 1984).* Pure and Applied Chemistry. **57**(4): p. 603-619.

23. E. Frackowiak and F. Béguin, *Carbon materials for the electrochemical storage of energy in capacitors.* Carbon, 2001. **39**(6): p. 937-950.

24. E. Frackowiak, *Carbon materials for supercapacitor application.* Physical Chemistry Chemical Physics, 2007. **9**(15): p. 1774-1785.

25. C. Arbizzani, M. Mastragostino, and F. Soavi, *New trends in electrochemical supercapacitors.* Journal of Power Sources, 2001. **100**(1–2): p. 164-170.

26. H. Pröbstle, M. Wiener, and J. Fricke, *Carbon Aerogels for Electrochemical Double Layer Capacitors.* Journal of Porous Materials, 2003. **10**(4): p. 213-222.

27. H. Pröbstle, C. Schmitt, and J. Fricke, *Button cell supercapacitors with monolithic carbon aerogels.* Journal of Power Sources, 2002. **105**(2): p. 189-194.

28. K.K.J. Kay Hyeok An, Jeong Ku Heo, Seong Chu Lim, Dong Jae Bae, and Young Hee Lee, *High-Capacitance Supercapacitor Using a Nanocomposite Electrode of Single-Walled Carbon Nanotube and Polypyrrole.* J. Electrochem. Soc., 2002. **149**(8): p. A1058-A1062

29. F. Pico, et al., *Single-Walled Carbon Nanotubes as Electrodes in Supercapacitors.* Journal of The Electrochemical Society, 2004. **151**(6): p. A831-A837.

30. S. Iijima, *Helical microtubules of graphitic carbon.* Nature, 1991. **354**(6348): p. 56-58.

31. S. Iijima and T. Ichihashi, *Single-shell carbon nanotubes of 1-nm diameter.* Nature, 1993. **363**(6430): p. 603-605.

32. E.T. Thostenson, Z. Ren, and T.-W. Chou, *Advances in the science and technology of carbon nanotubes and their composites: a review.* Composites Science and Technology, 2001. **61**(13): p. 1899-1912.

33. P.A. Philip G. Collins, *Nanotubes for Electronics.* Scientific American, 2000. **283**: p. 62-69.

34. R.M. Reilly, *Carbon Nanotubes: Potential Benefits and Risks of Nanotechnology in Nuclear Medicine.* J Nucl Med, 2007. **48**: p. 1039-1042.

35. C.-C. Hu, M.-J. Liu, and K.-H. Chang, *Anodic deposition of hydrous ruthenium oxide for supercapacitors.* Journal of Power Sources, 2007. **163**(2): p. 1126-1131.

36. B.J. Lee, et al., *Carbon nanofibre/hydrous RuO_2 nanocomposite electrodes for supercapacitors.* Journal of Power Sources, 2007. **168**(2): p. 546-552.

37. I.-H. Kim and K.-B. Kim, *Electrochemical Characterization of Hydrous Ruthenium Oxide Thin-Film Electrodes for Electrochemical Capacitor Applications.* Journal of The Electrochemical Society, 2006. **153**(2): p. A383-A389.

38. J.P. Zheng, P.J. Cygan, and T.R. Jow, *Hydrous Ruthenium Oxide as an Electrode Material for Electrochemical Capacitors.* Journal of The Electrochemical Society, 1995. **142**(8): p. 2699-2703.

39. W. Sugimoto, et al., *Charge storage mechanism of nanostructured anhydrous and hydrous ruthenium-based oxides.* Electrochimica Acta, 2006. **52**(4): p. 1742-1748.

40. W.Y.K. T. P. Gujar, I. Puspitasari, K.D. Jung and O.S. Joo, *Electrochemically Deposited Nanograin Ruthenium Oxide as a Pseudocapacitive Electrode.* International Journal of Electrochemical Science, 2007. **2**(9): p. 666-673.

41. K.-W. Nam, et al., *Pseudocapacitive properties of electrochemically prepared nickel oxides on 3-dimensional carbon nanotube film substrates.* Journal of Power Sources, 2008. **182**(2): p. 642-652.

42. V. Srinivasan and J.W. Weidner, *An Electrochemical Route for Making Porous Nickel Oxide Electrochemical Capacitors.* Journal of The Electrochemical Society, 1997. **144**(8): p. L210-L213.

43. E.E. Kalu, et al., *Cyclic voltammetric studies of the effects of time and temperature on the capacitance of electrochemically deposited nickel hydroxide.* Journal of Power Sources, 2001. **92**(1–2): p. 163-167.

44. K.-W. Nam and K.-B. Kim, *A Study of the Preparation of NiO_x Electrode via Electrochemical Route for Supercapacitor Applications and Their Charge Storage Mechanism.* Journal of The Electrochemical Society, 2002. **149**(3): p. A346-A354.

45. C.D. Lokhande, D.P. Dubal, and O.-S. Joo, *Metal oxide thin film based supercapacitors.* Current Applied Physics, 2011. **11**(3): p. 255-270.

46. J. Cheng, G.-P. Cao, and Y.-S. Yang, *Characterization of sol–gel-derived NiO_x aerogels as supercapacitors.* Journal of Power Sources, 2006. **159**(1): p. 734-741.

47. U.M. Patil, et al., *Chemically deposited nanocrystalline NiO thin films for supercapacitor application.* Applied Surface Science, 2008. **255**(5, Part 2): p. 2603-2607.

48. H.-K. Kim, et al., *Electrochemical and structural properties of radio frequency sputtered cobalt oxide electrodes for thin-film supercapacitors.* Journal of Power Sources, 2001. **102**(1–2): p. 167-171.

49. C. Lin, J.A. Ritter, and B.N. Popov, *Characterization of Sol-Gel-Derived Cobalt Oxide Xerogels as Electrochemical Capacitors.* Journal of The Electrochemical Society, 1998. **145**(12): p. 4097-4103.

50. S.G. Kandalkar, J.L. Gunjakar, and C.D. Lokhande, *Preparation of cobalt oxide thin films and its use in supercapacitor application.* Applied Surface Science, 2008. **254**(17): p. 5540-5544.

51. H. Zhu, D. Yang, and L. Zhu, *Hydrothermal growth and characterization of magnetite (Fe_3O_4) thin films.* Surface and Coatings Technology, 2007. **201**(12): p. 5870-5874.

52. H.Y. Lee and J.B. Goodenough, *Ideal Supercapacitor Behavior of Amorphous $V_2O_5{\cdot}nH_2O$ in Potassium Chloride (KCl) Aqueous Solution.* Journal of Solid State Chemistry, 1999. **148**(1): p. 81-84.

53. Y. Sato, et al., *Charge-Discharge Characteristics of Electrolytically Prepared V_2O_5 as a Cathode Active Material of Lithium Secondary Battery.* Journal of The Electrochemical Society, 1991. **138**(9): p. L37-L39.

54. T. Cottineau, et al., *Nanostructured transition metal oxides for aqueous hybrid electrochemical supercapacitors.* Applied Physics A: Materials Science & Processing, 2006. **82**(4): p. 599-606.

55. S. Devaraj and N. Munichandraiah, *High Capacitance of Electrodeposited MnO_2 by the Effect of a Surface-Active Agent.* Electrochemical and Solid-State Letters, 2005. **8**(7): p. A373-A377.

56. L.I. Hill, et al., *One-Step Electrochemical Synthesis of alpha-MnO_2 and alpha [center-dot] gamma-MnO_2 Compounds for Lithium Batteries.* Electrochemical and Solid-State Letters, 2001. **4**(11): p. A180-A183.

57. X.-L. Luo, et al., *Ascorbic acid sensor based on ion-sensitive field-effect transistor modified with MnO2 nanoparticles.* Analytica Chimica Acta, 2004. **512**(1): p. 57-61.

58. V. Volotovsky and N. Kim, *Ascorbic acid determination with an ion-sensitive field effect transistor-based peroxidase biosensor.* Analytica Chimica Acta, 1998. **359**(1–2): p. 143-148.

59. L. Bai, et al., *Rechargeability of a Chemically Modified MnO_2/Zn Battery System at Practically Favorable Power Levels.* Journal of The Electrochemical Society, 1993. **140**(4): p. 884-889.

60. H.Y. Lee and J.B. Goodenough, *Supercapacitor Behavior with KCl Electrolyte.* Journal of Solid State Chemistry, 1999. **144**(1): p. 220-223.

61. M.-S. Wu and P.-C.J. Chiang, *Electrochemically deposited nanowires of manganese oxide as an anode material for lithium-ion batteries.* Electrochemistry Communications, 2006. **8**(3): p. 383-388.

62. N. Nagarajan, H. Humadi, and I. Zhitomirsky, *Cathodic electrodeposition of MnOx films for electrochemical supercapacitors.* Electrochimica Acta, 2006. **51**(15): p. 3039-3045.

63. Q. Fan and M.S. Whittingham, *Electrospun Manganese Oxide Nanofibers as Anodes for Lithium-Ion Batteries.* Electrochemical and Solid-State Letters, 2007. **10**(3): p. A48-A51.

64. L.-C. Zhang, et al., *Shape-Controllable Synthesis and Electrochemical Properties of Nanostructured Manganese Oxides.* The Journal of Physical Chemistry C, 2007. **111**(24): p. 8418-8423.

65. B.B. Lakshmi, C.J. Patrissi, and C.R. Martin, *Sol−Gel Template Synthesis of Semiconductor Oxide Micro- and Nanostructures.* Chemistry of Materials, 1997. **9**(11): p. 2544-2550.

66. Y. Dai, et al., *Manganese oxide film electrodes prepared by electrostatic spray deposition for electrochemical capacitors from the $KMnO_4$ solution.* Journal of Power Sources, 2006. **161**(1): p. 737-742.

67. K.-W. Nam and K.-B. Kim, *Manganese Oxide Film Electrodes Prepared by Electrostatic Spray Deposition for Electrochemical Capacitors.* Journal of The Electrochemical Society, 2006. **153**(1): p. A81-A88.

68. F.M.a.M.K. A. Eftekhari, *Template-free preparation of bunches of aligned manganese oxide nanowires.* J. Phys. D: Appl. Phys., 2005. **38**: p. 628.

69. H. Chen, et al., *Reducing dissolution of MnO_2 nanofibers by doping with ferric ion.* Science and Technology of Advanced Materials, 2007. **8**(1–2): p. 63-66.

70. Y. Zheng, et al., *Multiple branched α-MnO_2 nanofibers: A two-step epitaxial growth.* Journal of Crystal Growth, 2006. **286**(1): p. 156-161.

71. J.N. Broughton and M.J. Brett, *Variations in MnO_2 electrodeposition for electrochemical capacitors.* Electrochimica Acta, 2005. **50**(24): p. 4814-4819.

72. M. Nakayama, et al., *A Novel Electrochemical Method for Preparation of Thin Films of Layered Manganese Oxides.* Chemistry Letters, 2004. **33**(6): p. 670-671.

73. M.-S. Wu, *Electrochemical capacitance from manganese oxide nanowire structure synthesized by cyclic voltammetric electrodeposition.* Applied Physics Letters, 2005. **87**(15): p. 153102-3.

74. S.-C. Pang, M.A. Anderson, and T.W. Chapman, *Novel Electrode Materials for Thin-Film Ultracapacitors: Comparison of Electrochemical Properties of Sol-Gel-Derived and Electrodeposited Manganese Dioxide.* Journal of The Electrochemical Society, 2000. **147**(2): p. 444-450.

75. C.-C. Hu and T.-W. Tsou, *Ideal capacitive behavior of hydrous manganese oxide prepared by anodic deposition.* Electrochemistry Communications, 2002. **4**(2): p. 105-109.

76. H. Kim and B.N. Popov, *Synthesis and Characterization of MnO_2-Based Mixed Oxides as Supercapacitors.* Journal of The Electrochemical Society, 2003. **150**(3): p. D56-D62.

77. J. Wen, X. Ruan, and Z. Zhou, *Preparation and electrochemical performance of novel ruthenium–manganese oxide electrode materials for electrochemical capacitors.* Journal of Physics and Chemistry of Solids, 2009. **70**(5): p. 816-820.

78. Y.-S. Chen and C.-C. Hu, *Capacitive Characteristics of Binary Manganese-Nickel Oxides Prepared by Anodic Deposition.* Electrochemical and Solid-State Letters, 2003. **6**(10): p. A210-A213.

79. M. Nakayama, et al., *Electrodeposition of Manganese and Molybdenum Mixed Oxide Thin Films and Their Charge Storage Properties.* Langmuir, 2005. **21**(13): p. 5907-5913.

80. M. Nakayama, T. Kanaya, and R. Inoue, *Anodic deposition of layered manganese oxide into a colloidal crystal template for electrochemical supercapacitor.* Electrochemistry Communications, 2007. **9**(5): p. 1154-1158.

81. K.R. Prasad, K. Koga, and N. Miura, *Electrochemical Deposition of Nanostructured Indium Oxide: High-Performance Electrode Material for Redox Supercapacitors.* Chemistry of Materials, 2004. **16**(10): p. 1845-1847.

82. M. Kalaji, P.J. Murphy, and G.O. Williams, *The study of conducting polymers for use as redox supercapacitors.* Synthetic Metals, 1999. **102**(1–3): p. 1360-1361.

83. http://www.sigmaaldrich.com/technical-documents/articles/material-matters/ionic-liquids-for.html.

84. K.S. Ryu, et al., *Symmetric redox supercapacitor with conducting polyaniline electrodes.* Journal of Power Sources, 2002. **103**(2): p. 305-309.

85. A. Clemente, et al., *Solid-state, polymer-based, redox capacitors.* Solid State Ionics, 1996. **85**(1–4): p. 273-277.

86. A. Laforgue, et al., *Polythiophene-based supercapacitors.* Journal of Power Sources, 1999. **80**(1–2): p. 142-148.

87. R.K. Sharma, A.C. Rastogi, and S.B. Desu, *Manganese oxide embedded polypyrrole nanocomposites for electrochemical supercapacitor.* Electrochimica Acta, 2008. **53**(26): p. 7690-7695.

88. H. Zhang, et al., *Tube-covering-tube nanostructured polyaniline/carbon nanotube array composite electrode with high capacitance and superior rate performance as well as good cycling stability.* Electrochemistry Communications, 2008. **10**(7): p. 1056-1059.

89. G. Wang, L. Zhang, and J. Zhang, *A review of electrode materials for electrochemical supercapacitors.* Chemical Society Reviews, 2012. **41**(2): p. 797-828.

90. J.W. Long, et al., *Asymmetric electrochemical capacitors—Stretching the limits of aqueous electrolytes.* MRS Bulletin, 2011. **36**(07): p. 513-522.

91. A. Burke, *Ultracapacitors: why, how, and where is the technology.* Journal of Power Sources, 2000. **91**(1): p. 37-50.

92. Y.K.a.S.A.H. G.P. Pandey, *Ionic liquid incorporated polymer electrolytes for supercapacitor application.* Indian Journal of Chemistry, 2010. **49A**: p. 743-751.

93. M. Winter and R.J. Brodd, *What Are Batteries, Fuel Cells, and Supercapacitors?* Chemical Reviews, 2004. **104**(10): p. 4245-4270.

94. B. Djurfors, et al., *Microstructural characterization of porous manganese thin films for electrochemical supercapacitor applications.* Journal of Materials Science, 2003. **38**(24): p. 4817-4830.

95. C.H. Chen, et al., *Electrostatic spray deposition of thin layers of cathode materials for lithium battery.* Solid State Ionics, 1996. **86–88, Part 2**(0): p. 1301-1306.

96. L.T. de Jonge, et al., *A comparative study of two advanced spraying techniques for the deposition of biologically active enzyme coatings onto bone-substituting implants.* Thin Solid Films, 2010. **518**(19): p. 5615-5621.

97. J.A. Switzer, *Electrochemical synthesis of ceramic films and powders.* American Ceramic Society Bulletin, 1987. **66**: p. 1521–1524.

98. I. Zhitomirsky, *Electrodeposition of ceramic materials and composites.* Surface Engineering, 2011. **27**(6): p. 403-406.

99. A. Jaworek and A.T. Sobczyk, *Electrospraying route to nanotechnology: An overview.* Journal of Electrostatics, 2008. **66**(3–4): p. 197-219.

100. I. Zhitomirsky, *Cathodic electrodeposition of ceramic and organoceramic materials. Fundamental aspects.* Advances in Colloid and Interface Science, 2002. **97**(1–3): p. 279-317.

101. I.Z. M. S. Ata, *Electrophoretic nanotechnology of ceramic films.* Advances in Applied Ceramics, 2012.

102. I. Zhitomirsky and A. Petric, *Electrophoretic deposition of electrolyte materials for solid oxide fuel cells.* Journal of Materials Science, 2004. **39**(3): p. 825-831.

103. S. Lebrette, C. Pagnoux, and P. Abélard, *Fabrication of titania dense layers by electrophoretic deposition in aqueous media.* Journal of the European Ceramic Society, 2006. **26**(13): p. 2727-2734.

104. I. Zhitomirsky, *Ceramic Films Using Cathodic Electrodeposition.* JOM-e Journal of the Minerals, Metals and Materials Society, 2000. **52**.

105. R. Damodaran and B.M. Moudgil, *Electrophoretic deposition of calcium phosphates from non-aqueous media.* Colloids and Surfaces A: Physicochemical and Engineering Aspects, 1993. **80**(2–3): p. 191-195.

106. P. Sarkar and P.S. Nicholson, *Electrophoretic Deposition (EPD): Mechanisms, Kinetics, and Application to Ceramics.* Journal of the American Ceramic Society, 1996. **79**(8): p. 1987-2002.

107. J.-K. Chang and W.-T. Tsai, *Material Characterization and Electrochemical Performance of Hydrous Manganese Oxide Electrodes for Use in Electrochemical Pseudocapacitors.* Journal of The Electrochemical Society, 2003. **150**(10): p. A1333-A1338.

108. Y.-S. Chen, C.-C. Hu, and Y.-T. Wu, *Capacitive and textural characteristics of manganese oxide prepared by anodic deposition: effects of manganese precursors*

and oxide thickness. Journal of Solid State Electrochemistry, 2004. **8**(7): p. 467-473.

109. M. Cheong and I. Zhitomirsky, *Electrophoretic deposition of manganese oxide films.* Surface Engineering, 2009. **25**(5): p. 346-352.

110. C.-Y. Chen, et al., *Characterization of spray pyrolyzed manganese oxide powders deposited by electrophoretic deposition technique.* Surface and Coatings Technology, 2007. **202**(4–7): p. 1277-1281.

111. T. Brousse, et al., *Long-term cycling behavior of asymmetric activated carbon/MnO_2 aqueous electrochemical supercapacitor.* Journal of Power Sources, 2007. **173**(1): p. 633-641.

112. Q.M. Yang, et al., *Pasted $Ni(OH)_2$ Electrodes Using Ni Powders for High-Drain-Rate, Ni-Based Batteries.* Journal of The Electrochemical Society, 2003. **150**(4): p. A543-A550.

113. V. Paserin, et al., *CVD Technique for Inco Nickel Foam Production.* Advanced Engineering Materials, 2004. **6**(6): p. 454-459.

114. J. Li and I. Zhitomirsky, *Electrophoretic deposition of manganese dioxide–carbon nanotube composites.* Journal of Materials Processing Technology, 2009. **209**(7): p. 3452-3459.

115. H. Lee, et al., *Mussel-Inspired Surface Chemistry for Multifunctional Coatings.* Science, 2007. **318**(5849): p. 426-430.

116. J.H. Waite, *Surface chemistry: Mussel power.* Nat Mater, 2008. **7**(1): p. 8-9.

117. K. Wu, Y. Wang, and I. Zhitomirsky, *Electrophoretic deposition of TiO_2 and composite TiO_2–MnO_2 films using benzoic acid and phenolic molecules as charging additives.* Journal of Colloid and Interface Science, 2010. **352**(2): p. 371-378.

118. P.M. Biesheuvel and H. Verweij, *Theory of Cast Formation in Electrophoretic Deposition.* Journal of the American Ceramic Society, 1999. **82**(6): p. 1451-1455.

119. I. Zhitomirsky, *Electrophoretic hydroxyapatite coatings and fibers.* Materials Letters, 2000. **42**(4): p. 262-271.

120. M.V. Ananth, S. Pethkar, and K. Dakshinamurthi, *Distortion of MnO_6 octahedra and electrochemical activity of Nstutite-based MnO_2 polymorphs for alkaline electrolytes—an FTIR study.* Journal of Power Sources, 1998. **75**(2): p. 278-282.

121. I.A. Janković, et al., *Surface Modification of Colloidal TiO_2 Nanoparticles with Bidentate Benzene Derivatives.* The Journal of Physical Chemistry C, 2009. **113**(29): p. 12645-12652.

122. K.D. Dobson and A.J. McQuillan, *In situ infrared spectroscopic analysis of the adsorption of aromatic carboxylic acids to TiO_2, ZrO_2, Al_2O_3, and Ta_2O_5 from aqueous solutions.* Spectrochimica Acta Part A: Molecular and Biomolecular Spectroscopy, 2000. **56**(3): p. 557-565.

123. P.A. Connor, K.D. Dobson, and A.J. McQuillan, *New Sol-Gel Attenuated Total Reflection Infrared Spectroscopic Method for Analysis of Adsorption at Metal Oxide Surfaces in Aqueous Solutions. Chelation of TiO_2, ZrO_2, and Al_2O_3 Surfaces by Catechol, 8-Quinolinol, and Acetylacetone.* Langmuir, 1995. **11**(11): p. 4193-4195.

124. I. Zhitomirsky and A. Petric, *Electrophoretic deposition of ceramic materials for fuel cell applications.* Journal of the European Ceramic Society, 2000. **20**(12): p. 2055-2061.

125. Y. Sun, M.S. Ata, and I. Zhitomirsky, *Electrophoretic deposition of TiO_2 nanoparticles using organic dyes.* Journal of Colloid and Interface Science, 2012. **369**(1): p. 395-401.

126. D. Lin and B. Xing, *Adsorption of Phenolic Compounds by Carbon Nanotubes: Role of Aromaticity and Substitution of Hydroxyl Groups.* Environmental Science & Technology, 2008. **42**(19): p. 7254-7259.

127. L.M. Woods, Ş.C. Bădescu, and T.L. Reinecke, *Adsorption of simple benzene derivatives on carbon nanotubes.* Physical Review B, 2007. **75**(15): p. 155415.

128. J. Björk, et al., *Adsorption of Aromatic and Anti-Aromatic Systems on Graphene through π−π Stacking.* The Journal of Physical Chemistry Letters, 2010. **1**(23): p. 3407-3412.

129. S.C. Tjong, G.D. Liang, and S.P. Bao, *Electrical behavior of polypropylene/multiwalled carbon nanotube nanocomposites with low percolation threshold.* Scripta Materialia, 2007. **57**(6): p. 461-464.

130. W. Taucher-Mautner and K. Kordesch, *Studies of pasted nickel electrodes to improve cylindrical nickel–zinc cells.* Journal of Power Sources, 2004. **132**(1–2): p. 275-281.

131. Y. Yu, et al., *Nickel-Foam-Supported Reticular CoO–Li_2O Composite Anode Materials for Lithium Ion Batteries.* Angewandte Chemie International Edition, 2005. **44**(43): p. 7085-7089.

132. A. Yuan and Q. Zhang, *A novel hybrid manganese dioxide/activated carbon supercapacitor using lithium hydroxide electrolyte.* Electrochemistry Communications, 2006. **8**(7): p. 1173-1178.

133. J. Li, Q.M. Yang, and I. Zhitomirsky, *Nickel foam-based manganese dioxide–carbon nanotube composite electrodes for electrochemical supercapacitors.* Journal of Power Sources, 2008. **185**(2): p. 1569-1574.

134. Q.S. Song, et al., *Performance improvement of pasted nickel electrodes with multi-wall carbon nanotubes for rechargeable nickel batteries.* Electrochimica Acta, 2007. **53**(4): p. 1890-1896.

135. V.I. Chani, et al., *Effect of substrate pre-coating on adhesion of sintered nickel plaques for electrode application in rechargeable batteries.* Journal of Power Sources, 2005. **142**(1–2): p. 370-381.

136. E. Cormier, et al., *A new powder morphology for making high-porosity nickel structures.* Journal of Power Sources, 2007. **171**(2): p. 999-1009.

137. Y.-g. Wang, L. Yu, and Y.-y. Xia, *Electrochemical Capacitance Performance of Hybrid Supercapacitors Based on Ni(OH)$_2$/Carbon Nanotube Composites and Activated Carbon.* Journal of The Electrochemical Society, 2006. **153**(4): p. A743-A748.